Three-dimensional numerical modeling of flow dynamics and investigation of temporal scour hole development around paired stream deflectors in a laboratory flume

Tim Haltigin
Department of Geography
McGill University, Montreal
January 2005

A thesis submitted to McGill University in partial fulfillment of the requirements of the degree of Master of Science

Library and
Archives Canada

Published Heritage
Branch

395 Wellington Street
Ottawa ON K1A 0N4
Canada

Bibliothèque et
Archives Canada

Direction du
Patrimoine de l'édition

395, rue Wellington
Ottawa ON K1A 0N4
Canada

Your file Votre référence
ISBN: 0-494-12460-1
Our file Notre référence
ISBN: 0-494-12460-1

NOTICE:
The author has granted a non-exclusive license allowing Library and Archives Canada to reproduce, publish, archive, preserve, conserve, communicate to the public by telecommunication or on the Internet, loan, distribute and sell theses worldwide, for commercial or non-commercial purposes, in microform, paper, electronic and/or any other formats.

The author retains copyright ownership and moral rights in this thesis. Neither the thesis nor substantial extracts from it may be printed or otherwise reproduced without the author's permission.

AVIS:
L'auteur a accordé une licence non exclusive permettant à la Bibliothèque et Archives Canada de reproduire, publier, archiver, sauvegarder, conserver, transmettre au public par télécommunication ou par l'Internet, prêter, distribuer et vendre des thèses partout dans le monde, à des fins commerciales ou autres, sur support microforme, papier, électronique et/ou autres formats.

L'auteur conserve la propriété du droit d'auteur et des droits moraux qui protège cette thèse. Ni la thèse ni des extraits substantiels de celle-ci ne doivent être imprimés ou autrement reproduits sans son autorisation.

In compliance with the Canadian Privacy Act some supporting forms may have been removed from this thesis.

While these forms may be included in the document page count, their removal does not represent any loss of content from the thesis.

Conformément à la loi canadienne sur la protection de la vie privée, quelques formulaires secondaires ont été enlevés de cette thèse.

Bien que ces formulaires aient inclus dans la pagination, il n'y aura aucun contenu manquant.

Canada

ABSTRACT

A three-dimensional numerical model (PHOENICS) was used to investigate the role of stream deflector angle and length on the flow field in a rectangular laboratory flume. Subsequent bed topography surveys were performed to examine the role of obstruction angle on scour hole development over time. The model was capable of predicting laboratory velocity and turbulent kinetic energy measurements, performing better for flow over a flat stable bed than over a deformed sand bed. A new method of incorporating complex bed topography into a structured Cartesian mesh was developed in the process. Flow field properties such as dynamic pressure, velocity amplification, separation zone length and width, and downwelling extent and magnitude were found to be strongly dependent on deflector geometry. Equilibrium scour hole depths and geometry are also angle-dependent. A predictive equation was produced explaining the rate at which scour holes reach equilibrium, and compared well with existing literature. Finally, a method was developed whereby characteristics of the flow field over a flat, stable bed could be used to predict equilibrium scour hole geometry.

RESUME

Un modèle numérique tri-dimensionnel (PHOENICS) a été utilisé afin d'examiner le rôle de l'angle et de la longueur de déflecteurs de courant sur la dynamique de l'écoulement dans un chenal en laboratoire. Des relevés de topographie du lit ont aussi été recueillis pour étudier le rôle de l'angle d'obstruction sur le développement temporel de la zone de surcreusement. Le modèle numérique est parvenu à reproduire adéquatement les mesures de vitesse et d'énergie cinétique turbulente, avec des performances supérieures au-dessus d'un lit fixe et plat qu'au-dessus d'un lit de sable montrant une topographie complexe. Une nouvelle méthode a aussi été développée afin d'incorporer une topographie du lit complexe dans une maille structurée cartésienne. Les propriétés de l'écoulement telles que la pression dynamique, l'amplification de vitesse, la longueur et la largeur de la zone de séparation, ainsi que l'étendue et la magnitude de la zone de vitesse orientée vers le lit, sont toutes fortement dépendantes de la géométrie des déflecteurs. Une équation a été produit afin de prévoir le temps requis pour que la zone de surcreusement atteigne un état d'équilibre. Celle-ci se compare bien à ce qui a été observé dans la littérature. Finalement, les résultats ont permis de développer une méthode utilisant les caractéristiques de l'écoulement au-dessus d'un lit fixe et plat pour prévoir la géométrie de la zone de surcreusement à l'état d'équilibre.

ACKNOWLEDGEMENTS

I owe a debt of gratitude to NSERC and FQNRT, who provided the funding necessary to carry out this work.

Great thanks are due to Pascale Biron, without whose guidance, leadership, vision, and occasional prodding, the thesis could not have been produced. In addition, I would like to thank Michel Lapointe for constantly reminding me that there is a 'real world' with a 'physical basis' out there beyond the realm of numerical models.

To Jamie for throwing his hands at it, to Melanie for making everything better, and to Chad-dd-dd for taking up the battle against the ha-ha's, thank-you. I was privileged to be part of Team Fluvial for the past two years, and you certainly made it a more enjoyable ride.

Melissa, you deserve endless credit and thanks for your patience and support. I know I couldn't have been easy to deal with.... from time to time. Moreover, thanks go to my family, who has continued to provide the support and encouragement needed to "get this thing done already".

Mike Tilston must be thanked on countless fronts. From seemingly endless days of surveying to developing dot-product vector rotations on the back of a napkin, you've been there for all of it.

Further thanks go to Colleen Robson for her data, Stuart Lane for his invaluable input, Hugues Lantuit for being Hugues Lantuit, Sangsoo Han for his assistance, Dr. Susan Gaskin, John Bartzcak and the Civil Engineering Hydraulics Laboratory for the set-up, and Andy Coleborne from AC3D for his utter professionalism.

Finally, it must be remembered that day-to-day life still exists in the world of academia. I would therefore like to thank the Architecture Café for 50¢ coffee, Tim Horton's for moving in across the street, the Café Depot for its patio in the summer, Frito-Lay for coming up with Guacamole Doritos, and Bill Simmons from espn.com for the daily breaks.

TABLE OF CONTENTS

LIST OF FIGURES

LIST OF TABLES

LIST OF SYMBOLS

a – ordinary least squares (OLS) regression slope
a_1, a_2 – constants in Franzetti (1982) scour depth predictive equation
b – ordinary least squares (OLS) regression intercept; obstruction thickness
c_μ – empirical constant from the k-ϵ turbulence model ($c_\mu = 0.09$)
CR – contraction ratio; the lateral proportion of the channel obstructed by the deflectors
d_i – diameter than which i percent of the sediment mixture is smaller than, i.e. 50% of the bed sediment is smaller than d_{50}
d_s – depth of scour
d_{sm} – depth of maximum scour
d_{se} – depth of maximum scour after the bed has reached equilibrium
E – roughness parameter in Log-law wall function
F_d – densimetric Froude number
Fr – flow Froude number
F_s – distance upstream of deflectors where flow separates from the bank
F_w – width of the flow separation zone at the deflector nose
F_{zu}, F_{zd}, F_{zTot} – upstream, downstream, and total extent of downwelling flow distribution
g – acceleration due to gravity
i, j, k – downstream, lateral, and vertical directions, respectively, in boundary-fitted coordinate system
ke – kinetic energy
k_s – sediment equivalent grain size
k_w – turbulent kinetic energy at the boundary of the modeling domain
K_1, K_2 – constants in Ettema (1980) scour depth equation
K_s – 'alignment factor' in Melville (1997) scour depth equation
L – lateral projection distance of deflectors
m, n – constants in an exponential function of the form $y = me^{nx}$
N – shape factor equal to 1.25 for a rectangular abutment
n_x, n_y, n_z – number of modeling mesh cells in the downstream, lateral, and vertical directions, respectively
p – constant in Whitehouse (1997) and Cardoso and Bettess (1999) scour depth predictive equation; pressure term in the Navier-Stokes equations
P – dynamic pressure
P_{loc} – local minimum pressure immediately downstream of deflectors
P_x, P_y, P_{dist} – downstream, lateral, and total distance of local minimum pressure from deflector-bank junction
Q – channel discharge
q_s – sediment transport rate
R – bridge pier radius
Re – flow Reynolds number
$S_{u\text{-}b}$, $S_{d\text{-}b}$, $S_{w\text{-}b}$ – scour hole upstream, downstream, and lateral extent, measured relative to the channel bank

$\boldsymbol{S_{u-n}}$, $\boldsymbol{S_{d-n}}$, $\boldsymbol{S_{w-n}}$ – scour hole upstream, downstream, and lateral extent, measured relative to the deflector nose
$\boldsymbol{t}$ – time
$\boldsymbol{t_e}$ – time at which the bed has reached equilibrium
$\boldsymbol{T}$ – time at which scour hole has reached 0.632 of equilibrium depth
$\boldsymbol{T_1}$ – dimensionless time parameter in Whitehouse (1997) and Cardoso and Bettess (1999) scour depth predictive equation
$\boldsymbol{u, v, w}$ - downstream, lateral, and vertical velocity components, respectively
$\boldsymbol{u', v', w'}$ – root mean square of turbulent fluctuations in downstream, lateral, and vertical velocity components, respectively
$\boldsymbol{u_w}$ – average velocity parallel to the wall in the modeling domain
$\boldsymbol{u_*}$ – shear velocity
$\boldsymbol{U}$ – velocity magnitude
$\boldsymbol{\overline{U}}$ – average velocity for a given vertical flow profile
$\boldsymbol{U_0}$ – average approach velocity
$\boldsymbol{U_c}$ – velocity required to induce sediment movement, i.e. "critical" velocity
$\boldsymbol{W}$ – channel width
$\boldsymbol{x, y, z}$ – downstream, lateral, and vertical directions, respectively, in Cartesian coordinate system
$\boldsymbol{y_w}$ – distance between the boundary and the center of the boundary adjacent cell within the modeling domain
$\boldsymbol{y_w^+}$ – parameter that must be between 30 and 300 in numerical solution
$\boldsymbol{Y}$ – flow depth
$\boldsymbol{Y_0}$ – approach flow depth
$\boldsymbol{z_0}$ – height above bed where $U = 0$

$\boldsymbol{\phi}$ – sediment static angle of repose
$\boldsymbol{\kappa}$ – von Karmann constant ($\kappa = 0.4$)
$\boldsymbol{\rho}$ – fluid mass density
$\boldsymbol{\rho_s}$ – sediment mass density
$\boldsymbol{\sigma_g}$ – geometric standard deviation of bed sediment diameter
$\boldsymbol{\tau_b}$ – numerically simulated boundary shear stress
$\boldsymbol{\tau_c}$ – bed shear
$\boldsymbol{\tau_c}$ – bed shear stress required to induce sediment movement, i.e. 'critical' shear stress
$\boldsymbol{\tau_{ij}}$ – time-averaged Reynolds stress term in downstream and lateral directions
$\boldsymbol{\nu}$ – kinematic viscosity of fluid
$\boldsymbol{\Delta}$ – change between successive time intervals of measurement, i.e. ΔS_{u-n} is the change in upstream scour hole extent relative to the nose between t = 5min and t = 30min
$\boldsymbol{\Lambda_n}$ – velocity amplification at deflector nose
Θ - angle of deflector orientation

1. INTRODUCTION

1.1 GENERAL AIMS AND OBJECTIVES

The disappearance of suitable fish habitats through land-use changes and other factors has been extensively studied and documented (e.g. Anderson, 1998; Parrish *et al.*, 1998; Lammert and Allan, 1999; Hicks and Hall, 2003). The resulting loss of native fish stocks is, thus, of great concern for both ecological and economic reasons (Mercille, 2001). In an effort to counter these declines, various stream rehabilitation projects have been widely implemented (e.g. Hilderbrand *et al.*, 1997; Shields *et al.*, 1998; Muotka *et al.*, 2002).

Stream restoration is by no means a new idea. The first references of intentional anthropogenic modification to natural habitats date back hundreds of years (Thompson and Stull, 2002). However, it was not until the early 20th Century that instream measures became particularly utilized (*ibid*). Unfortunately, the success rates of many of the restoration efforts to follow over the next hundred years have been mixed (Frissel and Nawa, 1992; Kondolf and Micheli, 1995; Scruton, 1996; Van Zyll de Jong *et al.*, 1997).

Unsuccessful projects have resulted primarily due to resources being directed into small-scale, site-specific projects as opposed to developing more global restoration guidelines (Roper *et al.*, 1997). Such a 'trial-and-error' approach has dominated the past century and continues to be widely prevalent today (Brookes and Shields Jr., 1996), resulting in high maintenance costs and/or project failure (Kondolf and Micheli, 1995).

Restoration projects involving the installation of instream structures are particularly inhibited by an incomplete description of flow's response to physical obstructions, and how the bed, in turn, responds to changes in flow (Kondolf, 1998). Specifically, the influence of instream obstructions on flow structure and bed topography needs to be systematically identified and examined. Traditionally, this has been done via *in situ* (e.g. Sukhodolov *et al.*, 2002) or laboratory experiments (e.g. Kuhnle *et al.*, 1999; 2002). However, recent advances in computing power and software development have led to an increased reliance on numerical modeling for such investigations (e.g. Molinas and Hafez, 2000; Chrisohoides *et al.*, 2003).

Three-dimensional (3D) computational fluid dynamics (CFD) software such as PHOENICS has successfully been applied to various aspects of fluvial geomorphology, including flow dynamics at river confluences (Bradbrook *et al.*, 2001) and over complex bed topography (Lane *et al.*, 2002), thereby establishing its ability to cope with complicated flow problems. It is hypothesized, then, that a properly designed 3D model would also be capable of accurately reproducing the flow field around stream deflectors.

It is therefore the objective of this study to use a three-dimensional CFD code to:

1) simulate the flow field around paired deflectors in a laboratory flume and evaluate the model's performance against detailed laboratory measurements

2) examine how the flow field around deflectors is influenced by changes in the structures' size and orientation; and,

3) establish a relationship between simulated flow field properties with known changes in bed topography.

The realization of these objectives will provide great insight into flow field behaviour around stream deflectors, and may serve as a first step to the increased use of numerical models in the design stage of rehabilitation projects.

1.2 THESIS PRESENTATION

The thesis is organized around three sets of experimental results, examining flow dynamics and bed topography near paired stream deflectors. In order to meet the stated objectives, a structured research project was conducted and reported in the following chapters:

Chapter **2** explores the context within which the research falls. Beginning with an outline of fish habitat degradation and various stream rehabilitation methods, this chapter proceeds to describe the more detailed aspects of flow dynamics and bed scour near instream obstructions. The use of numerical models in fluvial investigations is then discussed, leading to a formalized statement of the thesis' objectives.

Chapter **3** describes the experimental and numerical methodologies. A summary of the laboratory procedures is presented, including outlines of the parent study conducted by Robson (2003) and the subsequent flume experiments performed in the spring of 2004. Following a general explanation of the governing mathematical and conceptual principles of the CFD code used in the study – PHOENICS – this chapter details the construction and application of the numerical model, and concludes with a summary of the data analysis undertaken.

Chapter **4** represents the first of the thesis' results sections. After the preliminary modeling mesh sensitivity analyses are presented, the model is applied to the laboratory setting. Simulated flow fields over both stable and deformed beds are then evaluated against laboratory velocity and kinetic energy measurements. A discussion of the model's performance in comparison to other published reports follows.

Chapter **5** reports the findings pertaining to objective (2). Simulations are performed using deflectors of varying angle and size to examine how obstruction geometry affects the three-dimensional flow field. Characteristics of the flow field around deflectors are then compared to flow around other types of obstructions.

Chapter **6** details the temporal evolution of bed scour near paired stream deflectors. The changes in scour depths and scour hole geometry over time are presented and compared against various predictive models. Finally, a relationship between the initial flow field and the equilibrium bed is proposed.

Chapter **7** summarizes the project with respect to the stated objectives by presenting the main findings of the study and proposing a number of recommendations for future work.

2. LITERATURE REVIEW AND STUDY OBJECTIVES

2.0 PREFACE

The degradation of fish habitat quality throughout North America has prompted the undertaking of extensive habitat rehabilitation projects (see White, 1996 for an exhaustive review). While various methods are available, one of the most common involves the installation of physical obstructions to flow (Gore and Hamilton, 1996). These obstructions promote bed scour, leading to the development of stable pool habitats for fish (Hey, 1996). Unfortunately, the success of such projects has been limited, in large part due to the poor understanding of the obstructions' impact on the flow field and ultimately how the channel responds to these changes in flow (Kondolf and Micheli, 1995).

Comparatively little research has targeted the feedback cycle between flow and bed topography around stream deflectors (e.g. Hey, 1996; Kuhnle *et al.*, 1999, 2002; Thompson, 2002; Biron *et al.*, 2004a; in press). Rather, the majority of research on scour is performed in an engineering context, primarily around bridge piers and abutments (e.g. Dey *et al.*, 1995; Melville, 1992, 1995, 1997; Lim, 1997; Martin-Vide *et al.*, 1998). The focus in many of these articles, though, tends to be on understanding the mechanism for *reducing* scour so as to increase structural stability (e.g. Kumar *et al.*, 1999; Melville and Hadfield, 1999), while the aim of habitat restoration is to *promote* scour (Thompson, 2002). Therefore, it has been suggested that geomorphologists need to play a stronger role in the planning and implementation phases of rehabilitation projects (Gilvear, 1999), building upon the foundation provided by engineers and applying it to ecological restoration.

Because of the temporal, logistical, and financial limitations of field studies (e.g. Rahman and Haque, 2004), the bulk of scour investigations have been performed in laboratory settings (e.g. Lim, 1997; Lim and Cheng, 1998; Marelius and Sinha, 1998; Graf and Istiarto, 2002) or numerically simulated (e.g. Dey *et al.*, 1995; Richardson and Panchang, 1998; Yen *et al.*, 2001; Ali and Karim, 2002). Although limited by scaling factors to field conditions (Ettema *et al.*, 1998a) and possible underestimation of turbulence intensity (Melville and Raudkivi, 1996), laboratory studies are invaluable for understanding the physical basis of the relationship between flow dynamics and bed response around instream obstructions.

The following chapter presents the findings of the literature survey and aims to illustrate the following: (1) stream deflectors and other instream structures have been only moderately successful in rehabilitating fish habitats; (2) there is an incomplete understanding of the interaction between flow and bed behaviour around instream structures; (3) traditional methods of measuring and/or predicting shear stress in the regions affected by the structures are problematic, and; (4) numerical modeling may be a useful tool in examining the flow field in more detail than would be possible via classical field or laboratory studies. The chapter then concludes with a presentation of the specific research questions addressed in this study and a refined statement of the thesis' objectives.

2.1 STREAM REHABILITATION

2.1.1 Fish Habitat Degradation

Fish population structure is determined primarily by physical habitat (Kondolf and Micheli, 1995; Shields *et al.*, 1995b; Heggenes, 1996). A 'healthy' river consists of alternating shallow and deep sections known as riffles and pools, respectively, which serve to house the fish at different life stages and times of year (Heggenes, 1996). For example, riffles have been shown to be an important source of dissolved oxygen for fish (Newbury and Gaboury, 1993), and deeper pools have slower moving water that can serve as a resting spot with lower temperatures (Thorne, 1997).

In many regions, though, land-use changes are having a negative impact on habitat quality. For example, increased sedimentation in agricultural areas can lead to the loss of the riffle-pool sequence (Lammert and Allan, 1999); as increased quantities of sediment are injected into the system, the spatial variation in channel depth and velocity can be lost (Trimble and Crosson, 2000). The homogenization of bed topography limits the amount of suitable habitat available for fish, and in the process, reduces overall species diversity (Roper *et al.*, 1997).

The loss of native fish stocks is of great concern for both ecological and economic reasons (Mercille, 2001). For example, habitat losses have been directly tied to declines in ecosystem productivity (Minns, 1997). Consequently, reductions in fish biomass leads to an overall loss in biodiversity (Zalewski and Welcomme, 2002), which in turn can increase the vulnerability of extinction for other species (Angermeier, 1995). Moreover, regional economies can be affected by the reduction or migration of fish populations (Ziegenhorn, 2000). In Canada alone, it is estimated that recreational fishers spent approximately $6.7billion on trip-related expenditures in 2000[1]. Economic impacts can then filter down to the local level. Because fish indirectly generate employment (Holmlund and Hammer, 1999), habitat destruction can potentially result in job losses.

2.1.2 Instream Habitat Modification

Attempts to augment fish populations through anthropogenic modification of habitats date back hundreds of years (Thompson and Stull, *in press*). However, prior to the 1930's this was done almost exclusively by private anglers (White, 1996), with no real ecological agenda. The common notion at the time was that sportsmen wanted to make fishing 'less like golf'; by locally increasing fish stocks, less time would be spent standing around and waiting for something exciting to take place (Thompson and Stull, in press).

Since then, the restoration of fish stocks has become one of the primary tasks of fisheries management (Ebersole *et al.*, 1997). In many cases, this is done by attempting to mitigate the local effects expressed by environmental changes elsewhere (Kondolf, 1998). Operating under the assumption that hydraulics and sediment distribution are key factors governing habitat biodiversity, rehabilitation schemes often include the installation of instream structures that modify local flow and channel characteristics to provide suitable microhabitat conditions for the targeted restoration species (Huusko and Yrjänä, 1998).

---

[1] http://www.pac.dfo-mpo.gc.ca/oceans/Policy/fishfact_e.htm

Various types of structures have been used in restoration projects, the most common being weirs (e.g. Hvidsten and Johnsen, 1992; Shields *et al.*, 1995a), woody debris (e.g. D'Aoust and Millar, 2000; Shields *et al.*, 2003), and stream deflectors (Kuhnle *et al.*, 1999; Thompson, 2002). While each of these structures differ in the cost of installation, aesthetics, and longevity (Wesche, 1985), their primary goal is to locally modify the hydraulics of the channel to promote bed scour for the formation of pool habitats (Hey, 1996). By increasing pool volume, local stocks are augmented primarily by immigration (Gowan and Fausch, 1996), attracted by the artificial pools that theoretically serve the same purpose for fish as would a naturally occurring pool, i.e. deeper water, cooler temperatures, etc. (Brookes and Shields Jr., 1996). A brief description of each structure is provided below.

Weirs – also referred to as check-dams or over-pour structures – are obstructions that span the entire channel width and are submerged at virtually all flow depths (FISRWG, 1998). They can serve many habitat rehabilitation purposes, including the enhancement or creation of pools, oxygenating water, and modifying sediment mobility (Wesche, 1985). Typically, scour pools are formed on the downstream side of the structure due to the increased shear stress resulting from the overtopping flow (Shields *et al.*, 1995a; D'Agostino and Ferro, 2004).

Large woody debris (LWD) refers to accumulations of organic matter that modify channel flow dynamics and morphology, nutrient dynamics, and composition of riparian vegetation (Berg *et al.*, 1998). Specifically, LWD creates zones of flow acceleration and deceleration, thereby accentuating the physical diversity inherently important to healthy fish habitats (Shields *et al.*, 2003). The regions of high and low velocity modify the shear stress induced on the bed, leading to the formation of scour pools and sediment accumulation, respectively (Wallerstein, 2003). Unlike permanent habitat structures, the locations of scour and deposition around LWD can vary, as the pieces are sometimes able to move and adjust to local flow conditions (Hilderbrand *et al.*, 1997).

Stream deflectors – also known as spur dikes or, when fully submerged, vanes or groynes – are vertical walls placed on the bank of the channel to reduce the cross-sectional area through which flow can pass. Deflectors behave like artificial point

Figure 2-1: Flow forcing and sedimentation patterns around deflectors of various planform shape and orientation (from Hey, 1996).

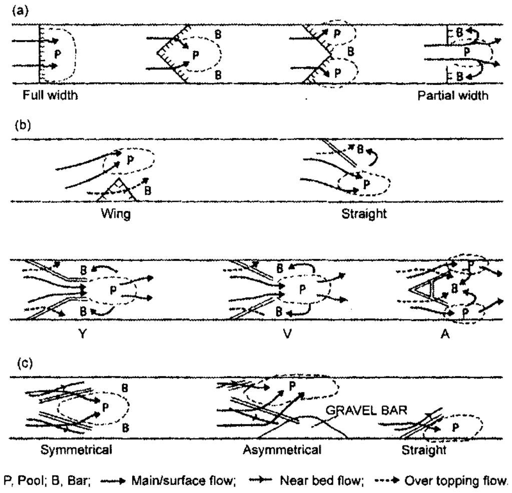

bars, reducing the channel's width-to-depth ratio and guiding the thalweg (FISRWG, 1998). The constriction imposed on the channel by the deflectors leads to a locally-increased water surface slope and accelerated flow, inducing an increase in mean bed shear stress (Thompson, 2002). Depending on the flow stage and the size and orientation of the deflector, flow is forced in different directions and the resulting scour can thus occur at different locations on the bed relative to the structure (Hey, 1996; Figure 2-1).

2.1.3 Rehabilitation Project Failure

Even though vast amounts of money have been directed towards habitat rehabilitation projects, their potential for success is generally unknown (Ebersole *et al.*, 1997). Certainly, several studies indicate that fish biomass can be increased locally because of such projects (e.g. Hunt, 1988; Binns, 1994; Shields *et al.*, 1995b), but many cases have proven ineffective, or even detrimental, to local fish stocks (e.g. Frissell and Nawa, 1992; Kondolf *et al.*, 1996; Pretty *et al.*, 2003).

Although there are problems defining the 'success' of a rehabilitation project from an ecological standpoint (Minns *et al.*, 1996), the *physical* success or failure of individual projects is determined by the interaction between hydraulic processes and structure design (Frissell and Nawa, 1992). Oftentimes, insufficient planning is involved. Minns *et al.* (1996) attribute project failure partially to the politics surrounding funding bodies, who sometimes believe that to be seen taking action may be more important than understanding the impact that a given project will have on an ecosystem. In addition, there has been insufficient effort put into post-project evaluation, in part because it is more difficult to secure funding for the seemingly ethereal concept of evaluation than the immediately tangible structures (Kondolf and Micheli, 1995).

Thus, the lack of success can be partly attributed to the money directed at small-scale, site-specific projects instead of developing more global restoration guidelines (Roper *et al.*, 1997). However, creating strategies that have universal applicability is virtually impossible. Even a detailed classification scheme for rivers and structures would amount to nothing more than a 'cookbook' approach that yields no fundamental information on how the river processes take place (Kondolf, 1998).

While specific restoration objectives need to be more clearly defined at the beginning of a project (Ebersole *et al.*, 1997), it is evident that any scheme involving instream modification must be tailored to local hydraulic and geomorphic conditions (Frissell and Nawa, 1992). However, successfully customizing projects to local conditions has also remained elusive to project designers, as many projects have failed expressly due to an inadequate understanding of the physical principles governing flow and bed response around instream structures (Kondolf, 1998).

Simple changes to structural design will not overcome high damage rates, as project failure stems from changes in channel morphology that had not been anticipated by project designers (Frissell and Nawa, 1992). It has therefore been recommended that fluvial geomorphologists become more involved in the design stages of rehabilitation projects (Kondolf, 1998). Consequently, one of the obstacles that must be overcome involves validating the widespread use of new technologies such as hydraulic numerical models (Gilvear, 1999). If the goal of habitat restoration is truly to "return an ecosystem to a close approximation of its condition prior to disturbance" (Kondolf and Micheli, 1995), it is imperative that the proper choices be made during the design phase. Otherwise, it may be necessary to engineer the habitat more heavily, thereby defeating the original purpose of the project (Hey, 1994).

2.2 FLOW DYNAMICS AND SCOUR NEAR INSTREAM STRUCTURES

2.2.1 Vortex Formation and Vertical Velocity: The Bridge Pier Analogy

Rather than focusing on abutments or spur dikes, research on flow dynamics and bed scour around instream hydraulic structures has been dominated by the study of these phenomena around bridge piers (Kothyari and Ranga Raju, 2001). However, the scouring mechanism around piers is acknowledged as being analogous to that around other instream obstructions (Melville, 1992), and thus serves as a logical departure point for analysis.

When a vertical obstruction is placed in a channel, formerly unidirectional flow becomes highly three-dimensional (Graf and Istiarto, 2002; Chrisohoides *et al.*, 2003). Flow decelerates as it approaches the structure, with the maximum deceleration occurring near the surface (Ahmed and Rajaratnam, 1998). As a result, an adverse pressure gradient is formed along the upstream face of the obstruction that induces a net downward forcing of flow (Ali and Karim, 2002). Although most of the flow is forced towards the bed, the stagnation pressure at the surface also creates a bow wave at the face of the structure (Richardson and Panchang, 1998) (Figure 2-2).

Figure 2-2: Generalized schematic of flow around a bridge pier (from Graf and Istiarto, 2002).

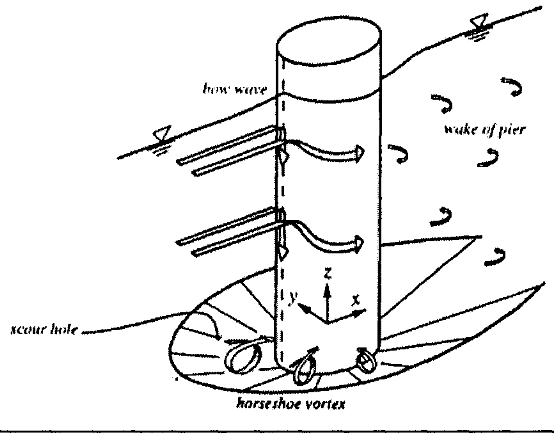

At the base of the pier, a horseshoe vortex system is formed that stretches and weakens in the downstream direction (Graf and Istiarto, 2002). Due to a sudden pressure drop at the nose (Fang *et al.*, 1997), a wake vortex system (vertical axis of rotation) then develops as flow separates around the pier, thus increasing turbulence intensity in this region and promoting augmented levels of bed erosion (Lim, 1997).

The resulting bed scour is related to both the vortex systems and the associated downflow upstream of the obstruction. Lim (1997) purports that scouring is dominated by the combination of the two, while others state that scouring is primarily due to the downflow component (Yen et al., 2001; Ali and Karim, 2002). The latter rests upon the assumption that the vertical flow in this region is the equivalent of a submerged jet (Karim and Ali, 2000).

The submerged jet analogy, however, may be partly erroneous. Ahmed and Rajartatnam (1998) summarize several major differences between a classic submerged jet and the pressure driven downflow next to a pier. First, they note that a jet is typically formed inside a nozzle and diffuses as it moves through ambient fluid, differing from the downflow caused by a pressure gradient because the latter forms and diffuses at the same time. In addition, they report that the approach flow upstream of a bridge pier carries both mass and momentum, whereas the ambient fluid around classical jets is stagnant.

Moreover, the timing of the horseshoe vortices' appearance is also subject to debate. Most studies indicate that the vortex system is one of the main causes of scour (e.g. Lim, 1997; Kothyari and Ranga Raju, 2001; Graf and Istiarto, 2002). However, Raudkivi (1986; cited in Ali and Karim, 2002) claimed that the horseshoe vortex is a consequence of scour, not a cause of it.

Although several similarities can be observed between flow patterns and scour hole geometry around spur dikes or bridge abutments and those found around bridge piers (Figure 2-3), certain differences remain (as described by Kothyari and Ranga Raju, 2001). First, the area over which downflow dominates the flow field is much larger for an abutment than for a pier. Also, the vortex system is allowed to separate around both sides of a pier, while the abutment's attachment to the bank forces separation to occur only on the nose side (projected into main flow). As a result,

Figure 2-3: Differences in flow and scour patterns around piers and abutments (from Kothyari and Ranga Raju, 2001).

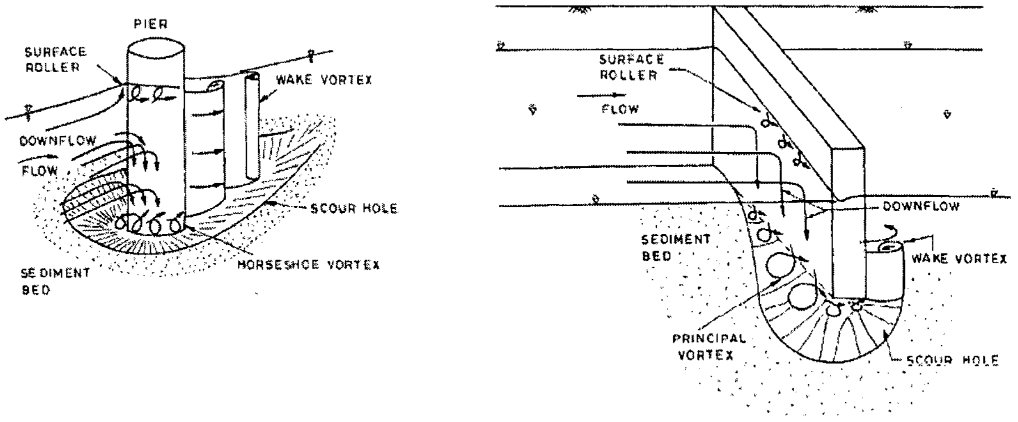

only half of the classic horseshoe is formed. Moreover, the scour hole itself ranges much farther downstream of a pier than an abutment. Finally, because of boundary layer effects produced by the channel wall, the scour hole near an abutment or deflector will be concentrated near the nose of an abutment, while scouring will be greatest near a pier's centerline.

2.2.2 Influence of Structure Design Features on Flow Patterns and Scour

Although the general principles behind scour formation are reasonably well developed, the three-dimensional flow dynamics around hydraulic structures becomes complicated by a number of factors. Depending on the obstruction's shape (Shamloo *et al.*, 2001; Rahman and Haque, 2004), size (Kuhnle *et al.*, 1999; Thompson, 2002), angle of orientation (Ettema *et al.*, 1998; Kuhnle *et al.*, 2002), and grouping (Sukhodolov *et al.*, 2002), the flow field in the immediate vicinity of the structure can be altered in various ways. To fully understand how a given object will alter channel flow and ultimately how the bed will react, each of the structural features must be examined.

a) Shape

The planform shape of an obstruction can significantly affect the surrounding flow field. For example, a poorly streamlined body results in a net thrust acting on the object due to a lower pressure zone in the lee of the obstruction (Shamloo *et al.*, 2001). Not only does the thrust affect the object's drag coefficient, but earlier studies have indicated that the recirculation zone can become enlarged when flow is forced around a quasi-two-dimensional body such as a bridge pier (e.g. Martinuzzi and Topea, 1993).

For example, Shamloo *et al.* (2001) examined flow properties and sedimentation patterns around various simple shapes. They reported that around hemispheres, the two legs of the horseshoe vortex reunite at the back of the body, resulting in the formation of a scour hole. Around a cube, however, the sharp edges of the poorly streamlined body were found to prevent the two legs from reattaching until significantly further downstream, and thus resulted in sediment deposition in the object's lee. When applied to bridge piers, Melville (1997) asserted that, in theory, the greater the streamlining of a pier or abutment, the lesser the equilibrium scour depth.

Moreover, the vertical shape of the obstruction is also important. Rahman and Haque (2004) showed that scour depths are reduced as the side-slope of a "spur-dike-like-structure" (e.g. groynes, abutments, deflectors, etc.) decreases. However, the relationship between obstruction shape and scouring is somewhat unclear. Kuhnle *et al.* (2002) developed an empirical scour-depth equation using spur-dikes with a side-slope of 45°. When Biron *et al.* (2004a) applied the equation to vertically oriented stream deflectors, the equation adequately predicted the observed scour depths, and actually yielded an underprediction in one case.

b) Size

The discrepancy between the Kuhnle *et al.* (2002) predictions and the Biron *et al.* (2004a) measurments may be partly explained by Melville and Raudkivi (1996), who claim that in practice the effect of shape is relatively insignificant as compared to other structural characteristics such as size. Differences in a structure's height and length have both been shown to strongly influence local scour phenomena.

The role of height is not applicable to bridge piers and abutments as they always protrude above the water surface, and thus, for reasonably deep flows, scour depth is virtually independent of water depth (Melville, 1997). However, restoration structures are often designed to be overtopped where winter ice cover is a problem (Dolinsek and Biron, 2001; Biron *et al.*, 2004a), hence its effect should be examined in detail.

Beginning with the analysis of flow over relatively simple objects, Shamloo *et al.* (2001) described the behaviour of a turbulent vortex system that appears when flow overtops the structure; as the height of the object increases, there is more mixing between the turbulent wake and the free surface flow. The amount of mixing increases until the top of the object is above the water surface, at which time the vortex system disappears and a strong reverse flow is present in the lee of the obstruction (Shamloo *et al.*, 2001).

Wu and Rajaratnam (1996) elaborated upon the complexity of overtopping flow, describing four distinct flow regimes depending on the overtopping ratio for submerged weirs (Figure 2-4). In the first regime, flow over the weir dives into the downstream flow as a jet and hits the bed of the downstream channel. Because vertical jets have been associated with changes in bed morphology (Chiew and Lim, 1996; Yen *et* al., 2001), scour would be expected in the region immediately downstream of the obstruction. In the other three regimes – collectively called *surface*

Figure 2-4: Overtopping flow regimes over submerged weirs (from Wu and Rajaratnam, 1996).

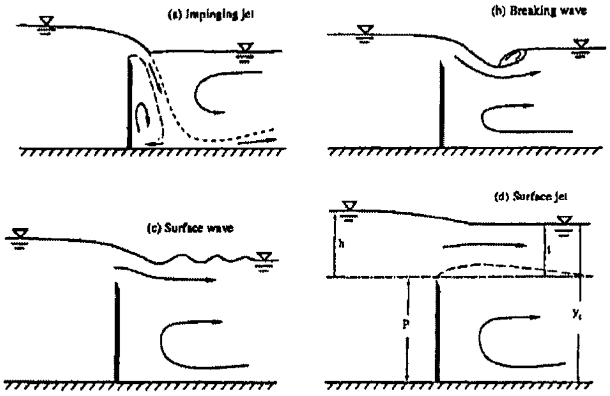

flow – the jet remains at the surface and grows in thickness downstream due to turbulent mixing, with an increasingly strong reverse flow found near the bed (Wu and Rajaratnam, 1996).

Sediment deposition has been associated with large areas of recirculation (Sukhodolov *et* al., 2002) due to the wake in such regions contributing nothing to the downstream transport of fluid (Ahmed and Rajaratnam, 1998). The reduced size of a recirculation zone behind overtopped obstructions may explain why less deposition has been reported in the lee of an overtopped obstruction as relative flow depth increases (Kuhnle *et al.*, 1999; Biron *et* al., 2004a). In addition, greater velocity amplification has been related to increased structure height (Biron *et al.*, in press). As velocity amplification is inherently tied to increases in shear stress, it is unsurprising that scour depths have been shown to be greater as structure height increases (Thompson, 2002; Biron *et al.*, 2004a).

The amount of discharge intercepted by an obstruction is also important (Richardson and Richardson, 1998). In general, it has been reported that scour depths and volumes are proportional to the cross-stream extent of a structure (Kuhnle *et al.*, 1999; 2002; Biron *et al.*, 2004a), mainly because a longer obstruction will impose a greater constriction on the channel, resulting in greater velocity and shear stress amplification (Biron *et al.*, 2004b; in press).

However, the relationship between obstruction length and flow velocity and shear stress only scales to a certain extent (Hoffmans and Pilarczyk, 1996). Melville (1995; 1997) illustrated that for longer abutments – where the length is greater than or equal to flow depth – scour depth is independent of structure length because part of the approach flow moves parallel to the face and therefore does not generate downflow. The notion of reduced scour depths at long obstructions was supported by Ahmed and Rajaratnam (1998), who reasoned that boundary layer effects from the channel wall will begin to dominate at longer abutments, thereby increasing the size of the stagnant flow region on the upstream side of the obstruction and ultimately reducing scour.

c) Angle

The angle of orientation of the obstruction has widely been shown to affect both the flow field and sedimentation patterns around hydraulic obstructions. For example, Biron *et al.* (in press) examined flow patterns around stream defectors oriented at 45°, 90°, and 135°. For both over- and undertopping flow conditions, they reported the greatest velocity amplification, largest recirculation zone area, and highest turbulence intensity for the 90° case.

The three-dimensional structure of the flow field is also dependent on orientation angle. Marelius and Sinha (1998) related the strength of secondary circulation to the angle of orientation of submerged vanes in a laboratory flume. It was found that although the classic horseshoe vortex and two 'suction-side' vortices (downstream-oriented axes of rotation) were present for all angles, the 'optimum' angle of attack to maximize recirculation strength was found to be between 36° and 45°, findings which were subsequently verified through numerical simulation (Sinha and Marelius, 2000).

Obstruction angle has also been tied to changes in bed morphology. Biron *et al.* (2004a) found that, as with maximum velocity and turbulence intensity, scour depths were greater for deflectors oriented perpendicular to flow than for those at 135° and 45°, respectively. For the same orientation angles, Kuhnle *et al.* (2002) examined scour hole volume and geometry around spur dikes. For short dikes, their results were in agreement with Biron *et al.* (2004a). However, for dikes of intermediate length, both depth and volume of scour increased uniformly with angle, maximized at 135°. These findings are more in line with Melville (1992), who also reported a positive relationship between structure angle and scour depth.

d) Grouping

The analysis of flow around a single structure remains relatively simplistic (Marelius and Sinha, 1998), as the flow field becomes increasingly complicated when groups of hydraulic structures are built in close proximity to each other. Sukhodolov *et al.* (2002) performed a comprehensive study on the flow dynamics within a groyne field. Flow around groynes is inherently complicated, with extensive separation zones at the groyne head leading to the formation of a large counter-rotating surface vortex, characterized by slower velocities in the center and increasing velocities progressively outwards (Sukhodolov *et al.*, 2004). It was shown that the number, rotation, and spacing of vortices – as well as the location and area of erosion and sedimentation zone – were all dependent upon the spacing of structures within the groyne field (Sukhodolov *et al.*, 2002).

However, very little work has been performed on flow dynamics and scour around groups of rehabilitation structures. Almost all previous studies on deflectors have focused on a single-wing design (e.g. Kuhnle *et* al., 1999, 2002; Thompson, 2002). To our knowledge, Biron *et al.* (2004a; b; in press) represent the only studies examining these phenomena around *paired* stream deflectors. Therefore, the effect that additional structures will have on flow and scour has yet to be clearly defined.

2.2.3 Temporal Evolution of Scour Holes

Most of the research involving scour focuses primarily on estimating equilibrium scour depths (Kothyari and Ranga Raju, 2001), which, for engineering purposes, remains the most important factor as it is inherently tied to the structural stability of a bridge (Johnson and Simon, 1997). In rivers, scour depths around piers or abutments may not reach maximum values for upwards of 70 years (Johnson and McCuen, 1991), and may, in fact, continue to increase indefinitely (Melville and Chiew, 1999). Therefore, the design life of the bridge is implicitly reliant on protecting against the maximum scour that can possibly occur.

Under field conditions, most floods do not have sufficient duration to generate equilibrium scour depths (Oliveto and Hager, 2002), and thus scour pools can be thought to develop incrementally. Therefore, the design of a restoration structure must consider the *rate* at which the pools develop. Habitat adaptation through time provides dynamic patterns to which species must either adapt or die (Ebersole *et al.*, 1997). Thus, if pools take longer to develop than can be utilized effectively by fish, the restoration project may be rendered futile as the target species would either have emigrated or perished.

Bed scouring is an exceedingly complicated process by which the sediment balance in a given area is in disequilibrium (Kothyari and Ranga Raju, 2001). In most cases, scouring begins at the location of the highest velocity or shear stress amplification, typically near the nose of the abutment or deflector (Ouillon and Dartus, 1997; Molinas *et al.*, 1998; Figure 2-5). Here, velocity amplification can reach up to 175% of approach values depending on the obstruction's projection into the main channel flow (Molinas and Hafez, 2000).

A shallow hole is formed initially, which then extends downstream in the form of a groove (Melville and Raudkivi, 1996) but does not change in width (Lim and Cheng, 1998). During the early stages of scour hole development, the lip of the trench is nearly vertical, such that further excavation undermines the scour hole slope and produces local avalanches (Kothyari and Ranga Raju, 2001), leading to increased depths.

As the scour hole deepens, water mass continuity dictates that flow velocity and shear stress will progressively decrease due to increased flow depth (Umbrell *et al.*, 1998). Eventually, a state of equilibrium is attained whereby the amount of sediment entering the scour hole is equal to the amount leaving it, with the upstream slope of the hole measuring between 28° and 33°, depending on the sediment's angle of repose (Blaisdell, 1996).

The rate at which equilibrium is attained depends upon the intensity of the approach flow (Lim and Cheng, 1998). Under 'clear-water' conditions, approach stress is less than critical, meaning that all sediment motion is due solely to the presence of the structure. In such instances, equilibrium depth (d_{se}) is reached asymptotically (Figure 2-6a). 'Live-bed' scour occurs when the approach flow is

Figure 2-5: Location of scour hole initiation (from Lim and Cheng, 1998)

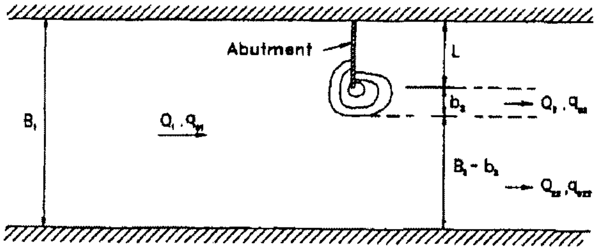

strong enough to initiate sediment transport, meaning that additional sediment will be brought into the regions affected by the obstruction. Under live-bed conditions, scour depths reach an initial peak and then fluctuate around a time-averaged mean, establishing a state of dynamic equilibrium due to the periodic passing of bedforms (Melville, 1997).

The shape of the temporal scour depth curve is also dependent on upstream flow intensity (Figure 2-6b). When clear-water conditions are present, equilibrium depth is approached in a more linear fashion as flow intensity increases, with 50-80% of the maximum depth being reached in the first 10% of the time to equilibrium (Melville and Chiew, 1999). No such curve corresponding to the time-dependence of live-bed scour could be found in the literature.

One must note, though, that there is no clear definition of what constitutes equilibrium. Theoretically, given steady, clear-water conditions, all sediment transport should stop when flow stress is reduced to just-below critical levels. However, sediment is generally excavated from the bottom of the scour hole in the form of bursts (Graf and Istiarto, 2002), and thus even an infrequent turbulent event could be enough to dislodge additional particles from the hole. Therefore, individual laboratory studies have defined their own criteria for bed equilibrium, taking from four hours (Martin-Vide *et al.*, 1998) to approximately ten days (Melville, 1997) of total run time.

Figure 2-6: (a) Temporal development of scour depth for clear-water and live-bed conditions (from Lim and Cheng, 1998); (b) Dependence of clear-water scour evolution on approach flow intensity (from Melville and Chiew, 1999).

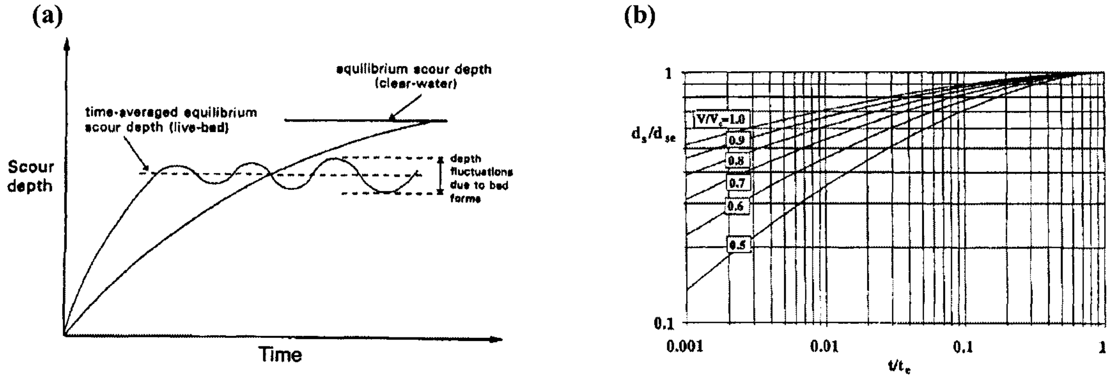

2.2.5 Scour Depth Prediction Models

Due to the complexities of the flow field imposed by instream obstructions, the depth and volume of local scour has proven difficult to estimate accurately (Kuhnle *et al.*, 2002). The underlying principle behind scour is that water mass continuity dictates flow acceleration due to the channel constriction imposed by the structure (Ahmed and Rajaratnam, 1998). A negative feedback cycle ensues whereby acceleration leads to bed scour, which leads to increased flow depth, ultimately reducing flow velocities until equilibrium is attained (Umbrell *et al.*, 1998). Theoretically, then, the volume of sediment eroded should simply be equal to the volume of flow that has been obstructed, so that the equilibrium cross-sectional area of the scoured channel is equal to that of an unobstructed, non-scoured channel. However, both Biron *et al.* (2004a) and Kuhnle *et al.* (2002) showed that different volumes of scouring occurred for identically-sized obstructions angled at 45° and 135° to flow, and thus further attention is warranted.

Throughout the literature, there is general agreement as to what factors play a role in the scouring process. Melville and Chiew (1999) state that scour is a function of various flow, sediment, and structural parameters, summarized as:

$$d_s = f[\mathit{Flood\ flow}\ (\rho, \nu, U_0, Y, g),\ \mathit{Bed\ Sediment}\ (d_{50}, \sigma_g, \rho_s, U_c),\ \mathit{Obstruction\ Geometry}(b, Sh, Al),\ \mathit{Time}(t, t_e)] \qquad \textbf{[2-1]}$$

where ρ is the mass density of water; ν is the kinematic viscosity; U_0 is the approach flow velocity; Y is the approach flow depth; g is acceleration due to gravity; d_{50} is the median sediment diamter; σ_g is the geometric standard deviation of the sediment mixture [$\sigma_g=(d_{84}/d_{16})^{1/2}$]; ρ_s is the sediment mass density; U_c is the velocity required to initiate sediment movement ("critical velocity"); b is the obstruction width, Sh and Al are parameters describing the shape and alignment of the structure; t is time; and, t_e is time-to-equilibrium.

The factors influencing scour can be combined to form a set of non-dimensional parameters, normalizing equilibrium scour depth (d_{se}) by obstruction thickness (b), as:

$$\frac{d_{se}}{b} = f(\alpha, \frac{L}{b}, \frac{U}{\sqrt{gb}}, \frac{Y}{b}, \frac{d_{50}}{b}, \sigma_g, \frac{\rho_s}{\rho}, \phi) \qquad [2\text{-}2]$$

where α is the obstruction orientation relative to approach flow; L is the obstruction length; *shape* refers to the shape of the obstruction; and ϕ is the static angle of repose of the sediment (Ettema *et al.*, 1998b). As ρ and ρ_s are constants, and d_{50} does not play a significant role unless it is relatively coarse (Melville and Chiew, 1999), these variables are generally dropped from consideration.

While the scientific basis for scour-depth predictions is well-developed, a unifying theory for doing so is still "in an embryonic stage, mainly due to the complex nature of the problem" (Ali and Karim, 2002). Most scour depth estimates are empirically-based (e.g. Melville, 1997; Lim and Cheng, 1998; Thompson, 2002), although other forms such as probabilistic equations exist (Johnson and Dock, 1998).

Virtually all of the published equations predict only a *maximum* depth of scour (Kuhnle *et al.*, 1999) and, at that, tend to be overestimates (Johnson, 1995). While overpredicting scour depths is satisfactory, if not preferable, for engineering studies, the applicability of such equations to stream rehabilitation projects may be limited. As outlined in the previous section, considering the rate at which scour pools develop may be important for the success of restoration projects. Six such equations were identified in the literature:

Oliveto and Hager (2002): $d_s = 0.068 N \sigma_g^{-1/2} F_d^{1.5} \log(T_1)$ **[2-3]**

Cardoso and Bettess (1999): $\frac{d_s}{d_{se}} = 1 - \exp\left(-1.025\left(\frac{t}{T}\right)^p\right)$ **[2-4]**

Melville and Chiew (1999): $\frac{d_s}{d_{se}} = \exp\left\{-0.03\left|\frac{U_c}{U_0}\ln\left(\frac{t}{t_e}\right)\right|^{1.6}\right\}$ **[2-5]**

Whitehouse (1997): $\frac{d_s}{d_{se}} = 1 - \exp\left[-\left(\frac{t}{T}\right)^p\right]$ **[2-6]**

Franzetti *et al.* (1982): $$\frac{d_s}{d_{se}} = 1 - \exp\left[a_1\left(\frac{Ut}{L}\right)^{a_2}\right] \qquad [2\text{-}7]$$

Ettema (1980): $$\frac{d_s}{L} = K_1 \log\left(\frac{d_{50}\upsilon t}{L^3}\right) + K_2 \qquad [2\text{-}8]$$

where d_s is depth of scour; N is a shape factor equal to 1.25 for a rectangular abutment; F_d is the densimetric Froude number $\{[F_d=(U/g'd_{50})^{1/2}]$ where $g'=[(\rho_s-\rho)/\rho]g\}$; and T_1 is a dimensionless time parameter $\{T_1=[(g'd_{50})^{1/2}/L_R]$, where $L_R=b^{\alpha}Y^{\beta}$, α is abutment orientation angle to flow, and $\alpha+\beta=1\}$; d_{se} is equilibrium scour depth; t is time; T is the time at which the scour hole has reached 0.632 of equilibrium depth; p is a constant (suggested by the authors that p = 0.350); U_c is the critical velocity required to initiate sediment movement; U_0 is the velocity of the approach flow; a_1 and a_2 are constants equal to -0.028 and 0.333, respectively; L is obstruction length, and; K_1 and K_2 are coefficients.

The Melville and Chiew (1999), Franzetti *et al.* (1982), and Ettema (1980) equations were developed for bridge piers, the Cardoso and Bettess (1999) and Oliveto and Hager (2002) equations were defined for bridge piers and abutments, and the Whitehouse (1997) model was developed for cylindrical obstructions in marine environments. Previous attempts at applying equilibrium scour-depth prediction models to stream deflectors have been only moderately successful. For example, Biron *et al.* (2004a) compared measured scour depths around stream deflectors to the depths predicted by Kuhnle *et al.* (2002) and Thompson (2002), and found only moderate levels of agreement. Therefore, if any or all of the *temporal* equations can be validated for scour around stream deflectors, they could potentially be of great use in the design phase of rehabilitation projects, allowing project managers to estimate bed evolution rates accurately.

2.3 SHEAR STRESS

2.3.1 Shear Stress Amplification and Uncertainty

The presence of an obstruction serves to substantially amplify ambient shear stress, especially for rough beds (Shamloo *et al.*, 2001). Depending on the upstream Froude number, the degree of channel contraction, and obstruction length, it can be augmented by up to 10 times of the approach values near a bridge abutment (Molinas *et al.*, 1998).

Properly accounting for shear stress is of fundamental importance for the analysis of sediment motion. Countless studies have related the strength of flow-induced stresses to the physical response of the bed, in both physical (e.g. Hoey and Ferguson, 1994; Wilcock, 1996; Haschenburger, 1999; Paquier and Kodashenes, 2002) and numerical experiments (e.g. Vigilar and Diplas, 1998; Lim and Cheng, 1998; Yen *et al.*, 2001). Therefore, if the feedback loop between flow patterns and channel morphology is to be understood, a clear picture of shear stress distributions should theoretically be required.

However, there remains uncertainty as to whether the knowledge of shear stress magnitudes is sufficient to predict bed evolution. The characterization of 'critical' shear stress – the strength of the force required to initiate motion for a given-sized particle – is ambiguous at best, having been defined in a variety of ways (e.g. Wilcock, 1996; Haschenburger, 1999). Compounding the issue is that scour may begin at lower levels of stress as compared to a similar channel configuration without an obstruction in it (Hager, 2002). Therefore, the interpretation of any physical or modeled shear stress value may be as difficult as measuring or simulating it in the first place.

2.3.2 Logarithmic Approaches and the Limitations of Field Measurements

Unless a Preston-static tube or shear plate is being used, shear stress values are *estimated* through calculation rather than being directly measured. The standard Law of the Wall ("log-law") (e.g. Wilcock, 1996; Biron *et al.*, 1998; Lawless and Robert, 2001) is one of the most common methods of doing so. However, several limitations exist with the log-law approach. Biron *et al.* (1998) illustrated that the calculated shear stress value may be highly dependent on near-bed velocity data resolution, indicating that predicted stress values will be underestimated if it is not possible to record the velocity measurements in the bottom 20% of flow.

Wilcock (1996) suggested a method to overcome the limitation described by Biron *et al.* (1998) – given knowledge of the channel's roughness properties – by using only a single velocity measurement and assuming a logarithmic velocity profile. However, a substantial problem arises in that the error associated with such an application is nearly threefold that of the standard velocity profile method (Wilcock, 1996).

The fundamental shortcoming of the aforementioned techniques relates to the assumption of a fully-developed logarithmic velocity profile. Although a logarithmic flow profile may exist in obstruction-free channels, flow patterns within a scour hole do not lend themselves to this type of analysis as the logarithmic profile breaks down immediately upstream of and within a scour hole (Graf and Istiarto, 2002). Therefore, other procedures must be used.

2.3.3 Turbulence-Based Estimates and the Limitations of Numerical Models

Several methods of calculating shear stress – such as Reynolds stress (Babaeyan-Koopaei *et al.*, 2002), Turbulent Kinetic Energy ('*TKE*'; McLelland and Nicholas, 2000), and a modified TKE (Kim *et al.*, 2000) – do not rely on assuming the presence of a logarithmic velocity profile. Rather, the alternate techniques calculate shear stress as a function of turbulent fluctuations in the downstream and vertical directions (*Reynolds*), downstream, lateral and vertical directions (*TKE*), or vertical direction only (*Modified TKE*). Such methods are important to understand because estimates based on turbulent characteristics of flow may be more applicable to local scour issues (Graf and Istiarto, 2002).

However, a dilemma arises if shear stress calculated by a turbulence-based method is to be used as validation data for a numerical model: the difficulty of accurately simulating turbulent fluctuations. For instance, not all turbulence closures (*see Section 3.3.2*) in numerical modeling provide the components to compute Reynolds shear stress (Pascale Biron, *personal communication.*). In addition, Nicholas (2001) stated that due to turbulent flow characteristics' strong sensitivity to modeling mesh resolution (see Section 2.4.3), it may be impossible to realistically and consistently reproduce field measurements of kinetic energy. By extension, it is likely that simulations will not be able to simulate shear stresses properly based on turbulent flow properties, especially if steady-state flow is being modeled (Ferguson *et al.*, 2003). Consequently, it may be problematic to compare shear stress estimates based on turbulent fluctuations with predictions from numerical models.

Moreover, choosing the appropriate method for application to the complex flow fields around obstructions is subject to debate. Similar to Molinas *et al.* (1998), Biron *et al.* (2004b) concluded that the TKE approach best explained the scour observed around deflectors in a laboratory flume. However, such a statement operates under the assumption that shear stress would be the greatest in regions where scour was the deepest. This assumption contrasts with Graf and Istiarto (2002), who state that shear stress decreases markedly upon entering a scour hole, reaching a minimum at the bottom.

Clearly, calculating shear stress and relating it to changes in bed morphology has limitations, regardless of what method is used. While it may be feasible for reach-scale studies (e.g. Lapointe *et al.*, 2000), contention will arise when attempting to do so for the local scour around instream obstructions, especially if a numerical model is being used.

2.4 NUMERICAL MODELS

2.4.1 General Use in Fluvial Studies

Whilst field and flume studies remain the conventional techniques to investigate open-channel flows, there is a growing trend towards incorporating numerical simulation. Computational Fluid Dynamics (CFD) has been applied successfully to study the flow fields in both laboratory (e.g. Hodskinson and Ferguson, 1998; Chrisohoides *et al.*, 2003; Lane *et al.*, 2004) and natural channels (e.g. Nicholas, 2001; Ferguson *et al.*, 2003; Biron *et al.*, 2004), examining issues ranging from watershed- and reach-scale processes (e.g. Nicholas and Mitchell, 2003) to small-scale turbulent fluctuations (e.g. Bradbrook *et al.*, 2000b).

Numerical models are an attractive research tool, providing three important advantages over flume and field studies (as summarized by Lane *et al.*, 1999):

1) the spatial density of data yielded by a numerical model is vastly increased over what can reasonably be collected in the field or laboratory;
2) additional explanatory information for understanding the behaviour and controls on various flow structures can be provided;
3) numerous combinations of boundary conditions (e.g. channel geometry, discharge, etc.) can be tested far more efficiently than can be done in the field or laboratory due to greatly reduced requirements of temporal and financial resources.

In addition, field measurements may be difficult to obtain near instream obstructions (Biron et al, 2004b). Therefore, a numerical model may be able to provide information in regions where data could otherwise not be collected.

Before recent advances in computer processing speed, flow simulations were traditionally performed in one (e.g. Garbrecht *et al.*, 1995) or two dimensions (e.g. Molls and Chaudhry, 1995; Nagata *et al.*, 2000; Nicholas, 2001). While one- and two-dimensional models simplify the definition of boundary conditions required to initialize and run a simulation (Lane *et al.*, 1999), they are only applicable to a small variety of flow conditions. The fundamental limitation of two-dimensional models is that they are depth-averaged, and thus provide only an average velocity for any given vertical flow column. For depth-averaging to be valid the underlying assumption is that a fully-developed logarithmic flow profile is present (e.g. Molls and Chaudhry, 1995; Molinas and Hafez, 2000), which may be the case for flow through a relatively uniform channel. However, significant changes in planform or topography can lead to flow separation (Ferguson *et al.*, 2003), and ultimately a departure from logarithmic flow.

As a result, there is a growing trend towards the use of three-dimensional (3D) numerical models (e.g. Meselhe and Sotiropoulos, 2000; Lane *et al.*, 2002; Rameshwaran and Naden, 2003). The primary benefit of 3D simulation is that it provides very detailed information in comparison to the relatively simplistic 1D or 2D options (Cao and Carling, 2002). For example, if flow separation is occurring, a 3D model will offer insight into the complete structure of the flow field rather than relying on planform vectors to represent three-dimensional processes (e.g. Bradbrook *et al.*, 1998). Although three-dimensional models require more detail in the definition of boundary conditions, more complicated modeling meshes, and increased processing time, they have been shown to be more reliable in terms of predictive capability over similar two-dimensional simulations (Lane *et al.*, 1999).

Numerical models are now in more widespread use, but there remains the issue of inadequate model calibration and verification in performance assessement (Cao and Carling, 2002). Open-channel CFD validation schemes have typically consisted of qualitative comparisons of simulated and recorded velocities in the form of predicted vs. measured flow profiles (Ferguson *et al.*, 2003). However, Bates *et al.* (2005) argue that that may be an insufficient test of model performance as the point measurements represent only a small sample of a much more complicated flow field, and thus more detailed statistical analyses should be performed.

2.4.2 Use in Bridge Pier / Abutment Studies

Along with generalized open-channel flow investigations, numerical models have been applied to the flow fields around instream structures such as bridge piers (e.g. Yen *et al.*, 2001; Ali and Karim, 2002), abutments (e.g. Biglari and Sturm, 1998; Molinas and Hafez, 2000), groynes (e.g. Ouillon and Dartus, 1997), and vanes (e.g. Sinha and Marelius, 2000). These models have strengthened and elaborated upon the foundation of knowledge about the flow fields around obstructions. For example, Dey et al. (1995) illustrated that the lip of a scour hole acts as a separation point, leading to the development of roller vortices within the hole (Figure 2-7a). In addition, Chrisohoides et al. (2003) showed that the 'stagnant' flow regions immediately upstream of the obstructions, thought to be reasonably quiescent, are actually far more turbulent and unsteady than previously assumed (Figure 2-7b).

Figure 2-7: (a) Flow separation upon entering a scour hole (from Dey *et al.*, 1995); (b) flow lines immediately upstream of an obstruction (from Chrisohoides *et al.*, 2003).

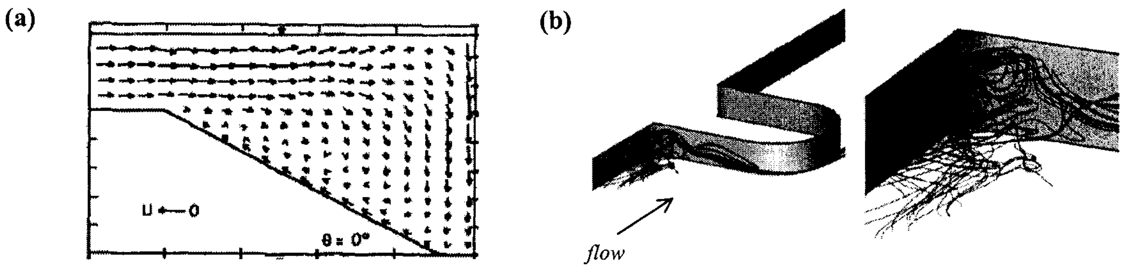

A variety of simulations have related flow structure to changes in bed morphology. In some cases, this has been done qualitatively, simply by showing that predicted regions of augmented shear stress match well with laboratory measurements of bed deformation (e.g. Ouillon and Dartus, 1997). In other cases, sediment transport functions have been coupled with a flow model to produce quantitative estimates of scour hole size and geometry (e.g. Lim and Cheng, 1998; Yen et al., 2001). However, the application of numerical models "for such strongly localized flow-sediment-morphology problems is still in relative infancy", due primarily to the questionable quality of the sediment transport relationships (Cao and Carling, 2002).

Because of the difficulty in properly coupling flow and sediment transport models, the majority of literature involves steady-state flow simulations over bed morphologies in various states of deformation (i.e. flat, stable and rigid; intermediate scour; and equilibrium). However, some of these models remain limited in applicability and validity due to depth-averaging (e.g. Karim and Ali, 2000) – assuming a logarithmic profile where one does not exist – or the incorporation of overly simplistic boundary geometry (e.g. Richardson and Panchang, 1998).

Finally, almost all applications of flow models around obstructions have been applied only to 90° abutments or circular piers due to the difficulty in modeling mesh definition for angled obstructions (see Section 3.2.3). Only one example incorporated various orientation angles for the structure (Sinha and Marelius, 2000). However, no details were provided on how the mesh was constructed beyond stating that it "was allowed to form to the shape of the <obstruction>" (p. 68).

2.4.3 Importance of Grid Definition

Now that the underlying physics of numerical flow models has been reasonably validated, increasing attention in the literature is being placed on the importance of a properly-designed modeling mesh (e.g. Hardy *et al.*, 1999; Lane *et al.*, 2002, 2004). Simulation results can be highly grid-dependent (Nicholas, 2001), meaning that a model's predictions may vary based on how the mesh is built. Thus, whenever a numerical model is being used as part of a research project, a rigorous grid-sensitivity analysis should be performed whereby at least four separate meshes are built and the results are compared to ensure grid independence (Hardy *et al.*, 1999).

When designing the mesh, the choice of spatial resolution – the number and spacing of grid cells within the modeling domain – is entirely arbitrary, though it is commonly assumed that a model's predictive capability increases as grid-cell resolution increases (Hardy *et al.*, 1999). However, with increased resolution comes greater computational expense, and thus a tradeoff must be made between the amount of data the user deems necessary and the amount of time that one is willing to invest in allowing for numerical solution (Richardson and Panchang, 1998).

Even if time-to-solution is not an issue, there are several points that must be considered. First, it is important to ensure that the grid-cell centers – where most models solve the governing flow equations – spatially correspond to field or laboratory measurement locations (Nicholas, 2001). Otherwise, it may be impossible to compare predicted and measured variables properly.

In addition, the size of the grid cells should be similar to the sensing volume of the measuring device (Lane *et al.*, 1999). For example, an electromagnetic current meter averages flow velocity over a larger volume than does an Acoustic Doppler Velocimeter (Lane *et al.*, 1998). If either device is being used for model evaluation but the grid cells have some intermediate volume, the model would therefore be predicting flow variables for a smaller or larger volume than they were measured at, respectively. An Acoustic Doppler Current Profiler (Williams and Simpson, 2004) complicates matters further, as the sensing volume is proportional to the distance away from the device (i.e. it averages velocity over a greater volume nearest the bed, assuming a downward-looking orientation). Therefore, near-bed model verification may be problematic because grid cells should be smallest in the regions closest to the channel boundaries so as to capture rapid variations in flow over a small distance (Molls and Chaudhry, 1995).

Moreover, grid cell resolution may affect the manner in which the model is parameterized. Hardy *et al.* (1999) showed that mesh resolution has a far greater impact on model predictions than does boundary roughness, and thus boundary conditions may have to be altered depending on the mesh used for the simulation. The dependence of boundary conditions on mesh resolution is reiterated by Nicholas (2001), who illustrated that, when using a standard wall function (see Section 3.3.3), increasing the number of cells in a grid effectively roughens the bed and thus any increase in mesh resolution should be accompanied by a reduction in the specified boundary roughness term.

The incorporation of boundary roughness through a generalized wall function may, in itself, be inherently flawed, especially when simulating flows over complex bed topography. In such cases, the mesh has typically been built by form-fitting the modeling domain boundary over topography measurements (e.g. Lane *et al.*, 1999; Bradbrook *et al.*, 2000a) (Figure 2-8a), with bed roughness defined as a 'representative' value of grain size (see Section 3.3.3). However, this is a problem-laden approach, as: 1) there is uncertainty as to what the representative roughness value should be; 2) scale-dependent roughness terms need to be spatially variable; 3) large values of boundary roughness can lead to numerical instability; and, 4) there is no clear definition of what the 'reference height' of the bed – the level from which the height of roughness elements on the bed are measured – should be (Lane *et al.*, 2004). Moreover, it is possible that rapid changes in topography would result in adjacent grid cells having an angle of greater than 20° between them, potentially leading to greater numerical instability (Spalding, 2002).

Lane *et al.* (2002; 2004) have overcome the difficulties of incorporating non-uniform boundary topography by defining bed topography using the notion of *bed porosity* (Figure 2-8b), where cell volumes are blocked out corresponding to elevation values from a Digital Elevation Model (DEM). Fully blocked cells are assigned a

Figure 2-8: Modeling mesh definition over complex topography using: (a) boundary-fitted coordinates and (b) numerical porosity (from Lane *et al.*, 2002)

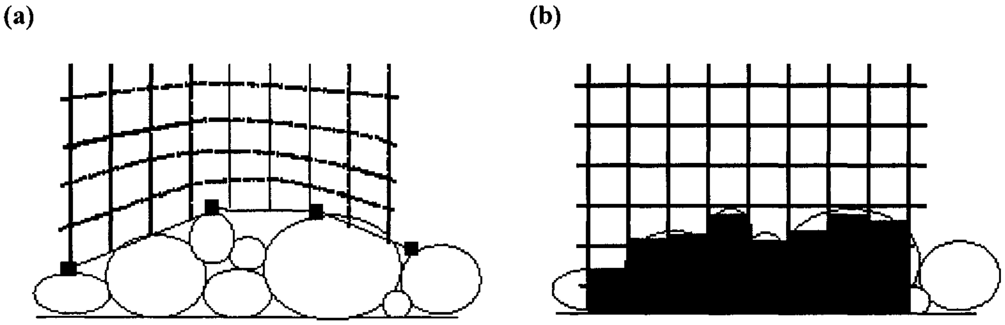

porosity value of zero, meaning that no flow is allowed to pass through it, fully-unblocked cells have a value of 1, and intermediate values are determined accordingly. The model's governing equations are thus modified to reflect that flow can pass through a given cell only partially, depending on its porosity value. Rather than warping the mesh itself, the bottom cells are modified such that they impose a condition within the domain to represent where a solid boundary would otherwise be located.

The bed porosity concept is particularly advantageous, especially for simulating flows within a scour hole. Because bed elevations change rapidly in the vicinity of obstructions such as bridge abutments and deflectors, the common method of building a numerical mesh has been the aforementioned "boundary-wrapping" (e.g. Karim and Ali, 2000; Ali and Karim, 2002) – thus raising the potential of violating the 20° cell skew restriction (Spalding, 2002) – or else relying an overly simplistic representation (e.g. Dey *et al.*, 1995; Richardson and Panchang, 1998). Therefore the porosity technique, or a simple analogue thereof, would allow grid cells to remain perfectly orthogonal while allowing for the incorporation of complex bed topography, thereby reducing the possibility of numerical instability.

2.5 REFINED STATEMENT OF OBJECTIVES

2.5.1 General Research Questions Addressed

While several decision-making criteria are involved in fish habitat restoration schemes (Shields *et al.*, 2003), one of the fundamental aspects remains properly understanding the physical response of the channel to anthropogenic modifications (Kondolf, 1998). As evidenced by the spotty record of habitat rehabilitation success, it is clear that the trial-and-error method in which these projects are often designed and implemented is insufficient (Brookes and Shields, 1996).

The choice to incorporate instream structures in habitat rehabilitation projects is heavily reliant on reasonable estimates of both how much scour will take place and where in the channel it will occur. However, the prediction of scour depth and extent has proven exceptionally difficult, with no real consensus having been reached through a unifying equation (Ali and Karim, 2002). Therefore, it may be necessary to take a different approach, developing a conceptual relationship between flow properties and the resulting bed topography. The overarching question in this thesis, then, asks:

"What is the relationship between the flow field around deflectors and the bed geometry at equilibrium?"

By addressing the properties of the scour hole as a function of the flow field, the nature of the scouring mechanism may be more fully explained. If answered successfully, it is possible that the principles can be combined to set the foundations to develop more detailed models for project designers to establish potential flow and bed responses prior to structure installation. To do so, the primary research question has been broken into three components.

To date, much of the related work on such a question has been limited to physical modeling in a laboratory setting. Of what little research has involved stream deflectors, very few studies have investigated flow and scour around *paired* stream deflectors, and none has yet involved numerical simulation. Therefore, the first research question addressed by the thesis is:

1) "Can a numerical model be used to reproduce the flow field around paired stream deflectors?"

Because numerical models yield orders-of-magnitude increases in the spatial resolution of hydraulic data as compared to field or laboratory studies (Lane *et al.*, 1999), it is probable that properly designed and executed simulations would provide unique insight into the complexity of the three-dimensional flow field around these structures.

Moreover, very little attention has been paid to the impact that various deflector designs will have on flow and scour. Most of the literature is focused on bridge piers and abutments, and thus the majority of knowledge can be applied only to cylindrical obstructions or vertical walls oriented perpendicular to flow.

For the most part, scour depth predictions only include a crude description of the mean flow field such as depth or Froude number, hence their application to complicated flow patterns often leads to questionable results for field tests (Richardson and Panchang, 1998). Rather than focusing on the impact of the structures on the bed directly, it is important to establish the flow's response to structural differences first, as flow is what ultimately causes the bed to scour. Therefore, a second question must be addressed:

2) "How is the flow field affected by changes in size and orientation of the obstructions?"

By acknowledging that bed topography is ultimately a result of modifications to the flow field by the structures, and the fact that scour hole depth and geometry have been shown to be affected by a structure's length and angle, it is likely that a detailed examination of flow around various structures will yield insight into the causes of such differences.

While the analysis associated with Question (2) is valuable for illustrative terms, it does nothing to explain *how* the bed reaches equilibrium. Rather, a process-based approach must be undertaken to examine the evolution of bed topography. Therefore, the final question of the thesis is:

3) "How does the bed change over time?"

This question is of fundamental importance, yet it has received relatively little attention in the literature. Few studies have investigated the temporal dynamics of scour, and at that, have concentrated almost exclusively on establishing a timeline for maximum scour depths. By visualizing how the entire bed changes throughout the scouring process, a more holistic description of the mechanisms by which the channel adjusts itself to artificial obstructions can be established.

2.5.2 Formal Statement of Objectives

Investigating the scouring process around instream obstructions requires a detailed understanding of the surrounding three-dimensional flow field structure. Laboratory settings are often preferable to field studies as they allow for the systematic isolation and control of various flow, channel, and obstruction characteristics. However, even flume studies remain limited by several factors.

For example, the time constraints associated with laboratory measurements can restrict the amount of data collected. As a result, the spatial resolution of the point-source data set may be inadequate to properly identify and interpret large-scale flow features (Ferguson *et al.*, 2003). Moreover, given the nature of the technology used to measure flow properties – as is the case for ADV velocity measurements – it is difficult, if not impossible, to gather information in the regions it may be most necessary to document, such as immediately next to the obstruction or bed (Biron *et al.*, in press). Furthermore, physical studies are often designed to measure a specific variable in a pre-determined location. Consequently, flow field characteristics that the study was not implicitly designed to measure but that still play a role in the scouring process may be neglected unintentionally.

Numerical models can thus provide numerous advantages. The spatial resolution of data yielded through simulation is essentially limited by computer processing speed only. Even a relatively coarse numerical mesh will provide hundreds to thousands of times more individual data points than can be collected in the laboratory within a reasonable time frame. In addition, these data span the entire flow field, including the locations nearest the obstruction and the regions not originally targeted for analysis.

That being said, it is not possible to rely on a numerical model alone. Although flow simulations are becoming increasingly dependable, sediment transport equations are not yet refined enough to produce predictions of bed evolution, especially in complicated flow fields (Cao and Carling, 2002). Moreover, the difficulty of comparing predicted and measured shear stress – ultimately the cause of sediment movement – is limited. Therefore, any study involving scour should contain a laboratory component to provide physical evidence of the channel's response to changing flow conditions. Provided the flow model is designed and constructed successfully, the laboratory and simulated data can then be used in conjunction to develop a relationship between the flow field and the bed topography; the model providing a more detailed illustration of flow than would laboratory measurements, with its output being correlated to physical, 'real-world' changes.

The objectives of this research are thus threefold, using a combination of CFD and laboratory methodologies to:

1) ***simulate the flow field around paired stream deflectors and evaluate its predictive capabilities against detailed laboratory measurements of three-dimensional velocity components and kinetic energy;***
2) ***examine how deflector length and angle of orientation affect the flow field by simulating flows around structures ranging from 30° to 150° and contracting 10% to 35% of the channel's width;***
3) ***illustrate how bed evolves throughout the scouring process and relate the changes in topography to flow field properties prior to deformation.***

Meeting the objectives stated above will provide a significant and unique contribution to the wider body of literature on flow and scour around instream obstructions, and will contribute to a greater understanding of the feedback mechanism between the flow field around deflectors and the resulting channel adjustment.

3. METHODOLOGY

3.0 PREFACE

The research was conducted in two distinct phases, involving laboratory and numerical modeling components, with the former being performed primarily by Robson (2003) and reported in Biron *et al.* (2004a; b; in press). The first phase consisted of collecting data in a laboratory flume, including flow velocity, turbulent kinetic energy, water surface topography, and channel topography.

These data were then used to construct the numerical model and test its predictive capabilities. After the model had been successfully evaluated (Chapter 4), subsequent simulations were performed to examine the nature of flow and bed response around paired stream deflectors (Chapters 5 and 6).

The following chapter provides a summary of both the laboratory methodology used by Robson (2003) (*Objective 1*; 'stable-' and 'mobile-bed' runs) and the subsequent laboratory procedures (*Objective 3*) conducted by the author in the spring of 2004 (henceforth referred to as the 'timeline' runs), details the construction and application of the numerical model (*Objectives 1-3*), and outlines the analysis performed on the laboratory and simulation data.

3.1 EXPERIMENTAL PROCEDURE

3.1.1 Description of Laboratory Flume

All laboratory experiments were conducted in a recirculating (flow only) flume tank in the Civil Engineering Hydraulics Laboratory at McGill University. A schematic of the flume is provided in Figure 3-1, and is described in detail below.

A rectangular plexiglas channel 4m * 0.4m * 0.20m in dimension was placed within a steel recirculating flume measuring 4m * 0.6m * 0.40m with a slope of 0.0005. Flow was driven by a sump pump, with discharge being controlled using a regulating gauge attached to the pump. In all cases, steady flow conditions were maintained. Upstream water depth was regulated with an adjustable weir located in the collection tank near the flume outlet. In addition, baffles were installed near the

Figure 3-1: Laboratory flume schematic (from Biron *et al.*, 2004a).

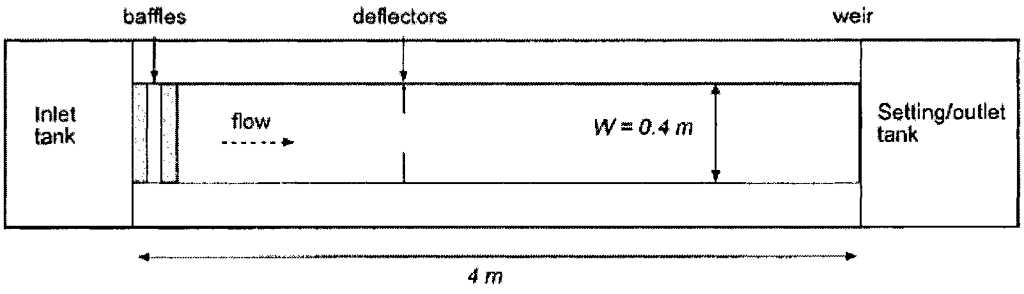

inlet to dissipate large-scale turbulence caused by the incoming flow and to produce inlet flow as close to uniform conditions as possible.

The deflectors were constructed out of plexiglas plates, 1.3cm in thickness, cut so that one of the vertical edges lay flush against the channel sidewalls and that the nose side of the deflector remained squared off. In all cases, the deflectors were attached to the sidewalls and plexiglas bed (stable-bed runs) or channel base (mobile-bed runs) with marine epoxy.

Figure 3-2 illustrates the deflector variables used in combination for the numerous flume experiments. Flow and scour around deflectors angled at 45°, 90°, and 135° – with respect to the downstream channel wall – were examined. In addition, two contraction ratios (*CR*) – the proportion of the channel obstructed by the deflectors – were used: 0.25 and 0.5. However, because of the instabilities in the flow field using *CR* = 0.5, these runs are eliminated from consideration in this study. In all cases, flow depth was less than the height of the deflectors.

Figure 3-2: Definition sketch of deflector orientations and contraction ratios.

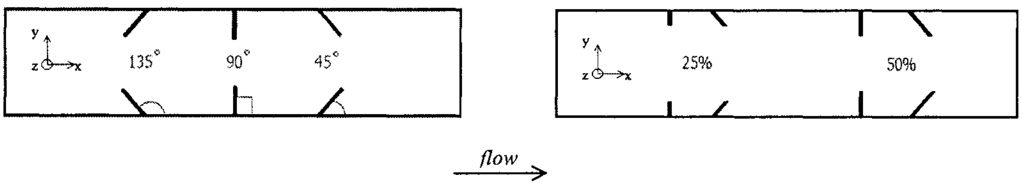

Combinations of the above variables were applied for runs over both stable (plexiglas) and mobile (sand) beds. The base of the plexiglas channel was filled with an 8cm thick layer of uniform silica sand, sieved through a 1.19mm mesh and retained by a 1.0mm mesh. The median diameter (d_{50}) of the sediment mixture is thus 1.10mm. Because the $d_{50} > 0.6$mm, no ripples formed on the bed (Melville and Chiew, 1999). The geometric standard deviation of the sediment mixture ($\sigma_g = [d_{84}/d_{16}]^{1/2}$) was 1.07, ensuring that no armor layer would form within the scour hole; armoring occurs if $\sigma_g > 1.5$ (Froehlich, 1995). The sediment was then levelled using a scraper blade attached to a carriage that slid along side-rails mounted on the edge of the tank.

For the stable bed experiments, a flat plexiglas plate 1.3cm in thickness was inserted atop the layer of sediment and attached to the channel walls using silicon caulking. For the mobile bed experiments, the plexiglas bed was removed and replaced with an additional layer of the sediment mixture described above, 1.3cm in thickness, and subsequently levelled. As a result, no modifications to the weir were required to maintain the same upstream flow depth in both the stable- and mobile-bed cases.

All of the mobile bed runs were performed under 'clear-water' conditions, meaning that the shear stress (τ_0) induced by the approach flow was less than the 'critical' stress (τ_c) required to initiate movement of the sediment. No sediment entered or exited the channel, and thus all changes to bed structure were due only to the presence of the deflectors.

For a more detailed description of the laboratory setup, the reader is referred to Biron *et al.* (2004a).

3.1.2 Flow Field Data

Velocity data were collected using a Sontek^{TM} Acoustic Doppler Velocimeter (ADV). The ADV measures flow velocity in a volume measuring approximately 0.25cm^3, located ~5cm below the sensor head, and breaks it into its three vector components – downstream (*u*), lateral (*v*), and vertical (*w*) – by making use of the Doppler principle. The device was run at each measurement location at a frequency of 25Hz for between

60 and 120 seconds, yielding between 1500 and 3000 consecutive, instantaneous three-dimensional velocity measurements per point. Following the recommendations of Lane *et al.* (1998), instantaneous measurements with signal correlations greater than 70% were retained (~96% of all measurements), and the signal-to-noise ratio for all data was above 15dB. No low-pass filters were applied (Robson, 2003).

The ADV was attached to an adjustable mounting bracket placed atop a carriage that slid along the flume side-rails. Care was taken to ensure that the device was vertically level and that the probes were oriented perfectly downstream. Consequently, no rotations needed to be applied to the raw velocity data (Lane *et al.*, 1998). A more detailed explanation of the ADV hardware, software, and processing can be found in Lane *et al.* (1998).

Detailed velocity profiles were recorded near the channel inlet to establish the average upstream velocity for each flume run. On average, 8-10 individual point measurements were taken at 1-3 verticals along a cross-section located well upstream from the deflectors. In each case, at least five of the point measurements were taken within the bottom 20% of flow depth, thereby reducing the errors associated with subsequent calculations of shear velocity (u_*) and shear stress (τ_0) (Biron *et al.*, 1998).

Velocity profiles were then calculated via the standard Law of the Wall:

$$\frac{U}{u_*} = \frac{1}{\kappa} \ln(\frac{z}{z_0}) \qquad \textbf{[3-1]}$$

where U is the velocity at height z above the bed; u_* is the shear velocity; κ is the Von Karmann constant (κ=0.4); ρ is the fluid density; and z_0 is the height above the bed where $U = 0$.

Average velocity ($\overline{U}$) is determined as:

$$\overline{U} = \frac{u_*}{\kappa} \ln(\frac{z}{ez_0}) \qquad \textbf{[3-2]}$$

where e is the base of natural logarithms ($e = 2.71828$). Discharge (Q) is calculated simply as the product of the channel's cross-sectional area (A) and the average velocity ($Q = \overline{U}A$). Table 3-1 summarizes the average velocity, discharge, shear velocity, Reynolds number, Froude number, and flow depth for both the Robson (2003) and Spring 2004 flume experiments.

For each flume run, Robson (2003) collected velocity measurements at two heights above the bed at an average of 63 verticals throughout the channel. For the stable bed runs, measurements were taken at approximately 0.5 and 2.5 cm above the bed, while data were collected at 0.7 and 2.5cm above the mobile bed. As was the case for the inlet measurements, the ADV was run at 25Hz for 60-120 seconds at all points.

Turbulent kinetic energy (ke) at each measurement point was calculated as:

$$ke=0.5\rho(<u'^2>+<v'^2>+<w'^2>) \qquad \textbf{[3-3]}$$

where u', v', and w' are the root mean square of the turbulent fluctuations in the downstream, lateral, and vertical directions, respectively.

For a more detailed description of these and other hydraulic variables measured and calculated, please refer to Biron *et al.* (2004b).

Table 3-1: Summary of flow flume experiment flow properties.

Source	Q (m^3/s)	U (m/s)	Re	Fr	Y (m)
Biron *et al.* (2004)	9.5×10^{-3}	0.25	23,750	0.26	0.095
Present study	7.9×10^{-3}	0.22	19,800	0.23	0.090

3.1.3 Topography Data

All bed and water surface topography points were collected to a precision of 1mm using a manual height gauge that was placed upon the sliding carriage described in the previous section. This method is considered accurate to +/- 2mm (Robson, 2003).

For the Robson (2003) mobile bed cases, the flume was run for four hours, allowing scour depths to reach approximately 92% of equilibrium levels. The pump was then stopped and the channel was drained slowly enough so as to not promote further bed deformation. At this time, full bed topography surveys were performed, with an average of 300 measurements taken per run ($\sim$214/m^2).

For the timeline runs, maximum scour depths were recorded at five minute intervals for the first 30 minutes, at 15 minute intervals for the next 30 minutes, at 30 minute intervals for the next hour, and then hourly until the scour hole reached equilibrium (defined as <1mm of change over three hours). At each interval, the pump was turned off, channel flow was allowed to stop, and the point of d_{sm} at both deflectors was located and measured. This process was repeated until equilibrium was attained.

A note of consideration must be taken here. It is possible that by stopping flow while sediment was still in transit (i.e. before the scour hole had reached equilibrium), additional particles may have slid into the scour hole under the force of gravity. As a result, the recorded scour depths could potentially be slightly underestimated. However, visual inspection during each stop indicated that if this was the case, the effect was negligible.

In addition to the maximum scour depth measurements, full topography surveys were performed at five minutes, 30 minutes, 120 minutes, and equilibrium for each timeline run, which allowed for the visualization of how the entire bed evolved with time. In all cases, topography measurements were recorded at a resolution of approximately 1-2cm^2 in the vicinity of the scour holes, with point density decreasing with distance from the deflectors. A summary of the number and density of point measurements for the timeline run topography surveys is provided in Table 3-2.

Table 3-2: Number (n) and density of bed topography survey points.

Angle	time (min)	n	density (n/m^2)
45°	5	450	281
	30	628	393
	120	889	556
	1070	1384	669
90°	5	312	195
	30	470	294
	120	534	334
	960	926	579
135°	5	391	244
	30	789	493
	120	933	583
	600	1379	862

The data from all surveys were entered into a Geographic Information System (GIS) – ArcGIS 8.2 – to produce a series of Digital Elevation Models (DEM). This was done using ArcGIS' Spatial Analyst Extension, through Inverse Distance Weighting (IDW; 8 nearest neighbours, power of 2) interpolation methods at a grid cell resolution of 4*4mm (e.g. Figure 3-3). The IDW technique was chosen over spline interpolation because the latter can erroneously under- and over-predict the lowest and highest DEM topography points, respectively, due the manner it which it fits a function to predetermined points. This would yield greater extremes in both scour and deposition topography coordinates, and could potentially lead to inaccuracies during modeling mesh design and construction (see Section 3.2.2). The benefit of IDW in this case is that the maximum and minimum elevations in the DEM are exactly those of the laboratory measurements.

Figure 3-3: Example of topography measurement locations and interpolated Digital Elevation Model.

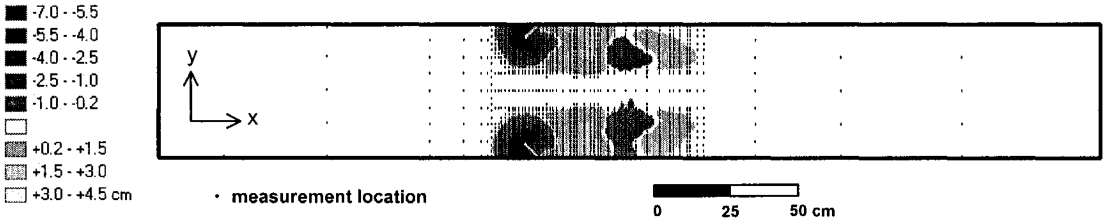

3.2 MODELING MESH DEFINITION

3.2.1 Cartesian vs Boundary Fitted Coordinates (BFC)

The first step in the modeling process involves the creation of a *modeling mesh* or *modeling grid* – a digital representation of the channel in which flow is simulated. The geometry of the inlet, outlet, banks, bed, and water surface are defined, and the interior volume is then discretized into individual contiguous pieces, or *cells*, in which the governing flow equations of the model are solved (see Section 3.3.2). This was done using the finite volume approach, where each cell has six faces and is thus cubic or cuboidal.

Meshes can be built in one of two coordinate systems: *Cartesian* and *Boundary Fitted Coordinates* (BFC). The Cartesian coordinate system is based on three orthogonally-oriented axes, whereas a BFC mesh has a "coordinate surface coincident with each boundary segment, analogous to the way in which lines of constant radial coordinates coincide with circles in the cylindrical coordinate system"[2]. In a BFC system, the traditional x- (streamwise), y- (lateral), and z- (vertical) directions are replaced with i-, j-, and k-directions, respectively, applied locally to each grid cell.

The choice to use either Cartesian or BFC space affects the manner in which various aspects of the mesh are dealt with, including bed topography, water surface representation, and deflector insertion. These topics are summarized in Table 3-3, and described in detail in the following sections.

Table 3-3: Managing various aspects of the modeling mesh based on the choice of coordinate system.

Property	Cartesian	BFC
Bed Topography	"Object Bed"	Surface Wrapping
Water Surface Representation	Rigid Lid	Water Surface Topography
Deflector Insertion	PARSOL	Pixelated

---

[2] http://www.ams.ucsc.edu/~shreyas/btp/node14.html

3.2.2 Incorporation of Bed and Water Surface Topography

Six faces of the simulation volume must be incorporated into the mesh. Because the flume used in the study was rectangular, the inlet, outlet, and banks are simply vertical, rectangular, two-dimensional (2D) plates attached to the bed and water surface at the upstream, downstream, and outer extremities of the channel, respectively. Due to the topographic variation seen in the bed and water surface, though, their construction warrants further description.

Each cell in a Cartesian system is perfectly orthogonal in all three dimensions, meaning that grid lines must be straight along all three axes. Therefore, the problem of cell skew – where the angle between adjacent cells should not exceed 20° (Spalding, 2002) – is eliminated. However, it also removes the possibility of taking any topographic variation into account, as the mesh in Cartesian space must be a perfectly rectangular prism.

The Cartesian restrictions did not pose a problem for bed construction in the stable-bed simulations. Because the plexiglas bed topography varied only +/-2mm, it can reasonably be considered a 2D plane. Therefore, each stable-bed mesh could easily be built in both Cartesian and BFC space. In both cases, the planform dimensions of the bed were specified for a 2D wall. Cell sizes were reduced near the banks and deflectors, with overall grid cell spacing and dimensions for both the Cartesian and BFC meshes created to be as equal as possible. For the stable-bed simulations, a series of grid sensitivity analyses were performed to optimize grid-cell size and spacing (see Section 4.1). A single Cartesian and BFC mesh, respectively, was then used for all deflector angles so as to eliminate the possibility of grid dependent results (Hardy *et al.*, 1999).

Because of the significant topographic variation in the mobile-bed cases, the traditional application of a Cartesian grid could not be used for the mobile-bed simulations. As a result, two separate options were pursued. The first involved a standard BFC representation of the topography, whereby the grid was fitted to the undulating bed coordinates using GeoGrid – a commercially-available mesh-generating software package designed to be compatible with the flow solver PHOENICS. Cross-sectional topography data from the laboratory were input into

GeoGrid and interpolated through an internal spline function to create a continuous bed surface. Care was taken to ensure that the angle between all adjacent cells did not violate the 20° cell-skew constraints.

The second method saw the bed inserted into a Cartesian mesh as an irregularly-shaped obstruction, referred to as an "object bed" (Figure 3-4). Object beds for each mobile-bed simulation were created using AC3D, a Computer Aided Design (CAD) software. DEM topography data points were imported into the software (i) and transformed into a three-dimensional Triangular Irregular Network (TIN) surface, which was subsequently smoothed (ii). A solid, regular, rectangular box was created and fit so that its faces just enclosed the outermost vertices of the TIN (iii). A boolean operation was then performed whereby the TIN was used as a 'cutting surface' to virtually lop off a partial volume of the box, yielding a six-faced object having a flat base and sides and a top representing the bed topography (iv). Because the planform dimensions of the object bed were equal to those of the channel, the object could then be placed directly onto the base of an empty Cartesian grid (v), with the bottom and sides aligned flush with the mesh bed and banks (vi).

The CAD object behaves in a conceptually analogous fashion to the bed porosity technique developed by Lane *et al.* (2002), where portions of cells in a right-angled mesh become blocked rather than form-fitting the grid boundary to highly irregular topography (detailed in Section 2.4.3). As a result, cell-skew issues are entirely avoided because an orthogonal structured grid is being used, hence all cells remain perfectly orthogonal even though complex topography is being incorporated.

As was the case for the stable-bed simulations, an extensive grid sensitivity analysis was performed. However, a single grid could not be used for the various BFC representations, as unique meshes had to be built for each separate run. For all subsequent mobile-bed BFC grids, the number of cells in each direction was held constant with grid cell spacing and size made as uniform as possible.

One of the fundamental limitations of simulating flow in Cartesian space relates to the representation of the water surface. As is the case for bed topography, varying water surface topography cannot be incorporated into the design of a Cartesian grid because each mesh face must be strictly two-dimensional. As a result,

Figure 3-4: Construction of the 'object-bed': (i): DEM points; (ii) creation of TIN surface; (iii) TIN surrounded by solid box; (iv) Boolean function to create six-sided bed; (v) 'empty' modeling mesh; (vi) insertion of bed into mesh. Dotted lines indicate location of inset.

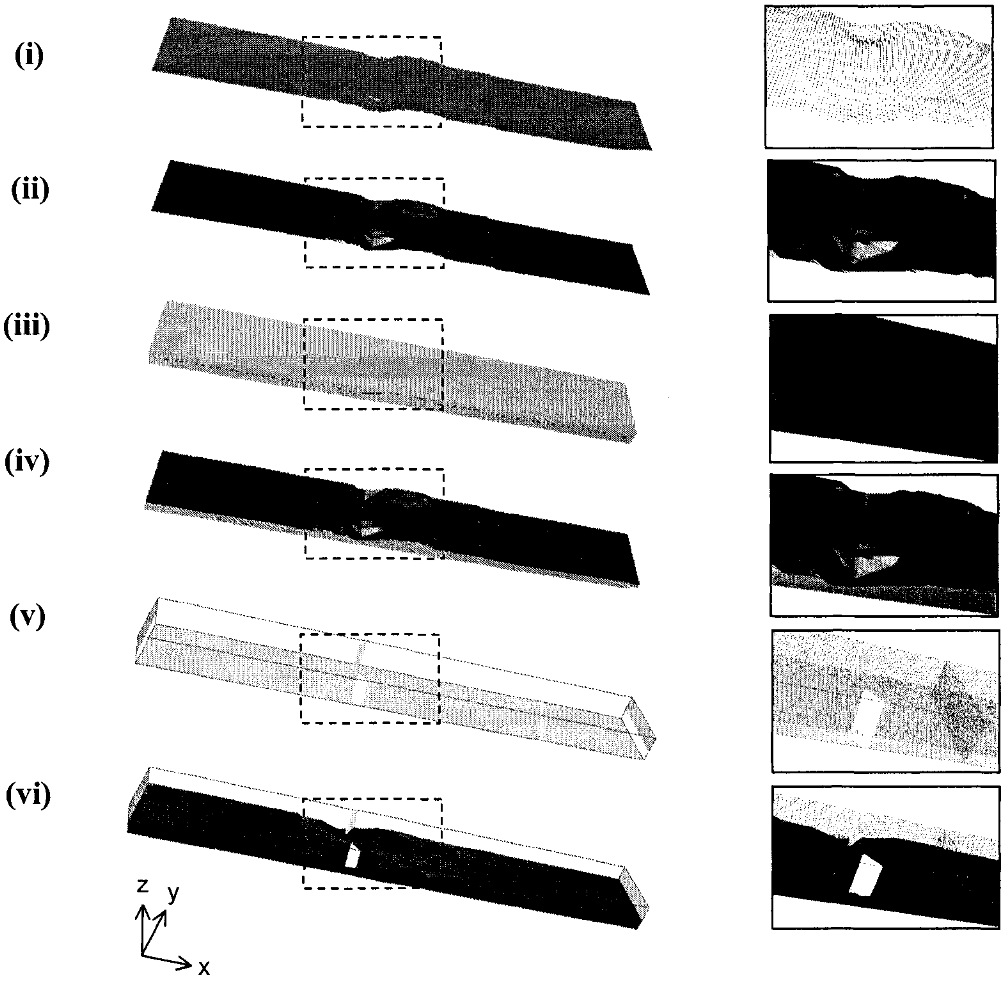

all meshes using Cartesian grids (stable-bed and object-bed simulations) were limited to planar water surface geometry.

The problem of incorporating water surface topography is easily overcome with BFC grids, where the water surface is constructed in a similar fashion as the bed. Laboratory water surface topography data points were entered into GeoGrid as cross-sections, interpolated to form a continuous surface, and attached as the upper-face of the simulation volume. To examine the effect on model results of water surface topography incorporation into mesh design, separate simulations in BFC space were performed with both a planar and a 3D water surface (see Section 4.2).

3.2.3 Deflector Construction

Cartesian and BFC meshes also differ in the manner in which they accept the insertion of solid blockages to flow. Therefore, the deflectors were incorporated into the two mesh types in separate fashions.

Irregularly shaped objects can be placed into a Cartesian mesh even if they do not obstruct a grid cell entirely; the outer boundaries of an obstruction need not perfectly match the grid lines of the modeling mesh. As a result, the real-world dimensions of an obstruction can be used exactly to define and construct a virtual obstruction to flow.

Therefore, deflectors for the stable-bed and object-bed simulations were built as regular rectangular prisms using AC3D. Planform dimensions of the deflectors were entered into the software, creating a four-sided polygon. The base of the deflector was then extruded vertically to create the final 3D object and inserted at the appropriate location in the mesh (flush with the bank, 2.10m from the inlet).

The modeling software can treat these deflectors in one of two fashions. During solution, the governing flow equations (see Section 3.3.2) can be solved for only the volume of the grid cell not obstructed by the deflector when using the 'Partial Solid' (PARSOL) extension. When PARSOL is activated, the mass continuity equations are modified to reflect that flow is passing through only a fraction of the cells obstructed by the deflectors (Figure 3-5a). Therefore, the equations are solved based on a partial cell volume. If this extension is not applied, all cells having more than 50% of their volume obstructed by the deflectors are considered fully-blocked, and no mass continuity modifications are made (Figure 3-5b).

The PARSOL method cannot be applied to the simulations involving BFC meshes, as BFC grids do not support externally-designed object importation. Consequently, two options were available. The first involved attempting to wrap the boundary geometry around the locations where the deflectors would have been placed. However, this resulted in a clear violation of the 20° cell-skew restriction, as angles between adjacent cells approached 45°. Therefore this method was discarded.

The remaining option involved the creation of 'pixelated' deflectors (Figure 3-5c), conceptually similar to the Cartesian cases when PARSOL is not activated. Because entire cells must be obstructed in BFC meshes and adjacent cells are designed to be as orthogonal as possible for ease of numerical solution, deflectors with smooth boundaries could not be created. Rather, vertical stacks of BFC cells – two to three cells in length in the downstream (i) direction, and one cell wide in the lateral (j) direction – were obstructed throughout the volume occupied by the deflectors. Each stack was high enough to fill the entire vertical column where it was located. The BFC deflectors were thus represented as a compilation of these stacks rather than as a single object.

Figure 3-5: Deflectors inserted into Cartesian mesh (a) with PARSOL activated, (b) without PARSOL, and; (c) 'pixelated' BFC deflectors. Grey shading indicates portions of grid cells blocked during numerical solution. Black outlines indicate boundary of object inserted into mesh.

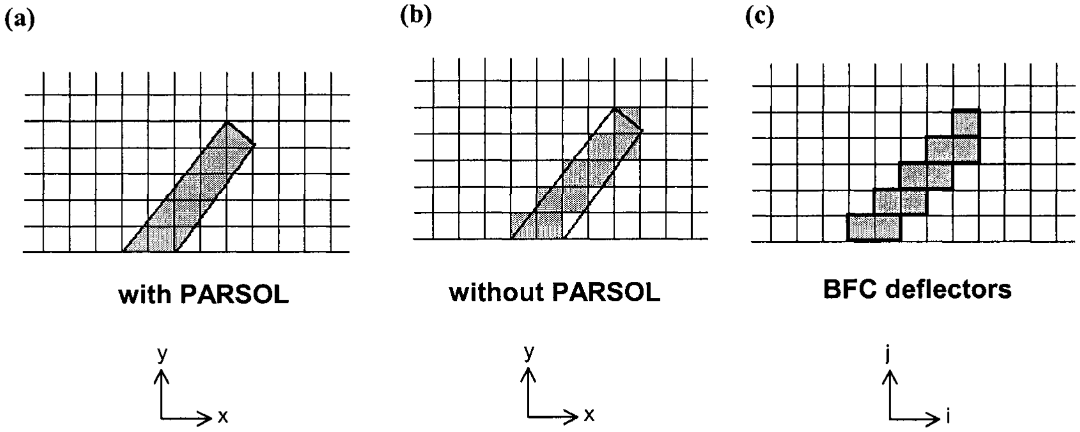

3.3 NUMERICAL MODELING APPROACH

3.3.1 PHOENICS: General Overview

As illustrated in Section 2.4, three-dimensional computational fluid dynamics (CFD) is becoming increasingly relied upon as a research tool to investigate the structure and behaviour of complex open-channel flows. A wide variety of CFD software packages are now commercially available, including that used in this study: PHOENICS.

PHOENICS is a general purpose, open-source Fortran code used to study an assortment of open-channel flow problems. Previous work has included its successful use in the investigation of flow over complex topography (Lane *et al.*, 2002; 2004) flow separation and recirculation at meanders (Bradbrook *et al.*, 2001; Ferguson *et al.*, 2003), and water surface topography and mixing at river confluences (Biron *et al.*, 2004c).

3.3.2 Governing Flow Equations

During solution, the software solves the fully three-dimensional form of the Reynolds Averaged Navier-Stokes (RANS) equations in each cell of the modeling domain:

continuity:

$$\frac{\partial u}{\partial x}+\frac{\partial v}{\partial y}+\frac{\partial w}{\partial z}=0 \qquad \textbf{[3-4a]}$$

momentum :

$$\begin{aligned}
u\frac{\partial u}{\partial x}+v\frac{\partial v}{\partial y}+w\frac{\partial w}{\partial z} &= -\frac{1}{\rho}\frac{\partial p}{\partial x}+\frac{1}{\rho}\left(\frac{\partial \tau_{ii}}{\partial x}+\frac{\partial \tau_{ij}}{\partial y}+\frac{\partial \tau_{ik}}{\partial z}\right)\\
u\frac{\partial u}{\partial x}+v\frac{\partial v}{\partial y}+w\frac{\partial w}{\partial z} &= -\frac{1}{\rho}\frac{\partial p}{\partial x}+\frac{1}{\rho}\left(\frac{\partial \tau_{ij}}{\partial x}+\frac{\partial \tau_{jj}}{\partial y}+\frac{\partial \tau_{jk}}{\partial z}\right)\\
u\frac{\partial u}{\partial x}+v\frac{\partial v}{\partial y}+w\frac{\partial w}{\partial z} &= -\frac{1}{\rho}\frac{\partial p}{\partial x}+\frac{1}{\rho}\left(\frac{\partial \tau_{ik}}{\partial x}+\frac{\partial \tau_{jk}}{\partial y}+\frac{\partial \tau_{kk}}{\partial z}\right)
\end{aligned} \qquad \textbf{[3-4b]}$$

with:

$$\tau_{ij}=\nu\left(\frac{\partial u_j}{\partial x_i}+\frac{\partial u_i}{\partial x_j}\right)-\overline{u'_i u'_j} \qquad \textbf{[3-4c]}$$

where τ_{ij} is the time-averaged Reynolds stress term for two of the three Cartesian directions, u, v, and w are time-averaged Cartesian velocity components in the x- (downstream), y- (lateral), and z- (vertical) directions, ρ is the fluid density, and p is the pressure term.

By definition, the RANS cannot close to completion because the Reynolds stress terms have been inserted into the momentum equations and therefore the system is no longer closed, i.e. there are more variables than equations (Olson and Wright, 1990). Additional equations provided in various turbulence models – of which PHOENICS provides over 20 choices – must be implemented to account for the transfer of momentum by turbulent structures. All simulations performed in this research used the RNG k-ϵ model (Yakhot and Orszag, 1986), previously shown to perform well for simulation of flows in areas affected by high shear (Richardson and Panchang, 1998) such as regions of significant separation and recirculation (Ferguson *et al.*, 2003), as is the case near deflectors.

3.3.3 Boundary Conditions

To initialize the model, turbulence intensity and three-dimensional velocity data – based upon the laboratory measurements – were entered at the inlet of the channel. A uniform average velocity was used at the inlet, as numerous initial simulations found no appreciable difference between using an average velocity and a logarithmic flow profile provided the deflectors were placed far enough away from the inlet to ensure that the flow field was fully developed before it reached the obstructions. Outlet conditions are defined in terms of a hydrostatic pressure distribution. Because hydrodynamic pressures in the model are calculated relative to the outlet conditions, care was taken to ensure that the outlet plane was located far enough away from the deflectors so as not to be affected by the negative dynamic pressures induced by flow recirculation behind the deflectors (Ferguson *et al.*, 2003).

Provided the bed roughness elements are less than half the size of the boundary-adjacent cell (Olsen and Stokseth, 1995), roughness values can be incorporated into the model though the standard Log-Law wall function as:

$$\frac{u_w}{u_*} = \frac{1}{\kappa}\ln(E{y_w}^+) \quad \textbf{[3-5a]}$$

with:

$$ {y_w}^+ = \frac{y_w u_*}{\upsilon};\ E = \frac{30.1\nu}{u_* k_s}\ \text{(for fully turbulent flows)} \quad \textbf{[3-5b]}$$

where y_w is the distance between the boundary and the center of the boundary adjacent cell; u_w and u_* are the average velocity and shear velocity parallel to the wall, respectively; k_s is the sediment equivalent grain size; and E is a roughness parameter (Biglari and Sturm, 1998). The wall function provides near-boundary conditions for flow and turbulence transport and thereby eliminates the need to extend computations right down to the boundary (Spalding, 2002). The wall function also applies to channel side-walls, defined in this research under no-slip conditions. However, choosing between slip and no-slip conditions is relatively insignificant, as it has been shown that model predictions are reasonably insensitive to walls defined under either option (Molls and Chaudhry, 1995).

The determination of k_s is also highly subjective, with values ranging from d_{50} to $3.5d_{84}$ in previous numerical modeling studies (Table 3-4). However, it has been shown that simulation results tend to be insensitive the value of k_s used, regardless of whether a smooth or rough bed is considered (Lane *et al.*, 2002). For the simulations in this study, smooth wall conditions (k_s = 0.000m) were applied to the stable (plexiglas) bed scenarios, while d_{50} (0.0011m) was used for the both the mobile-bed runs and subsequent timeline simulations.

Care must be taken to ensure that $30<{y_w}^+<300$ for the law of the wall to be applied outside the viscous sublayer and within the wall region, referred to as the "y^+ criterion" (Lane *et al.*, 2002). Values of ${y_w}^+$ were examined for each simulation (described in Section 4.2). Within the near-boundary region, the shear in the fluid is considered equivalent to the shear at the wall (Lane *et al.*, 2004), and can thus be used as a proxy for boundary stress.

Table 3-4: Roughness length (k_s) used in previous applications of 3D CFD.

Source	k_s
Booker *et al.* (2001)	$3.5d_{84}$
Nicholas (2001)	d_{50}
Lane *et al.* (1999)	d_{65}
Nicholas and Sambrook-Smith (1999)	d_{50}
Hodskinson and Ferguson (1998)	$3.5d_{84}$
Vigilar and Diplas (1998)	d_{90}

Boundary shear stress (τ_b) is calculated as a function of both the turbulence model and wall function, expressed in terms of kinetic energy at the boundary (k_w) as:

$$\frac{\tau_b}{\rho} = \frac{\kappa u_w c_\mu^{1/4} k_w^{1/2}}{\ln(E y_w^{+})} \qquad \textbf{[3-6a]}$$

with:

$$k_w = \frac{u_*^2}{\sqrt{c_\mu}} \qquad \textbf{[3-6b]}$$

where c_μ an empirical constant from the turbulence model ($c_\mu = 0.09$) (Biglari and Sturm, 1998).

The water surface boundary can be treated in two ways. Under the *rigid lid* assumption, the surface is considered a plane of symmetry, across which all normal resolutes are equal to zero (Lane *et al.*, 2002). In essence, this means that there can be no mass flux across the upper boundary of the mesh, and thus all flow is considered to be contained beneath the defined surface. Instead, a non-zero pressure term – "dynamic pressure" – is applied to the surface to represent water surface superelevation or depression (Ferguson *et al.*, 2003).

In reality, however, the water surface is highly variable and not well-represented by a horizontal plane. As a result, using the rigid lid treatment may lead to velocity overpredictions in regions where water surface superelevation would normally take place and underpredictions in zones of water surface depression (Lane *et al.*, 2004).

To counter the problems incurred by assuming a rigid lid, the mass continuity equation can be modified in the model to reflect the fact that the vertical extent of the flow domain would change with superelevation or depression (Ferguson *et al.*, 2003). This is done by introducing the notion of *porosity* for the mesh cells at the surface (following Bradbrook *et al.*, 1998). The porosity treatment allows the near-surface grid cell to effectively modify its thickness without constructing a new mesh. Variable porosities are attributed to these cells, thereby modifying the mass continuity equations without distorting streamwise velocities (Ferguson *et al.*, 2003).

Unfortunately, our knowledge of the numerical code limits water surface porosity to be applied to BFC cases only. PHOENICS does have the Cartesian equivalent to porosity built into the code in an extension called "Height of Liquid", but attempts to incorporate it in our simulations remained unsuccessful. Separate simulations for each setup were thus run using the rigid-lid treatment for simulations in Cartesian space and both rigid-lid and porosity treatments for the BFC cases.

3.3.4 Numerical Solution

Solution of the equations is achieved through a hybrid-differencing scheme called SIMPLEST, outlined in Bradbrook (2000) and summarized below. An arbitrary pressure field is guessed, and the governing flow equations are solved. The calculated velocities satisfy the momentum equations, but not continuity. Errors between the two are evaluated for each cell in the model based on the difference between inflow and outflow, after which a pressure correction equation is solved. The new pressure and velocity fields then satisfy continuity, but not momentum. A new pressure field is guessed and the process is repeated until the equations come to convergence and the mass and momentum errors are sufficiently small, generally around 0.1% of inlet flux values (Lane *et al.*, 2002). Solution convergence in all simulations was accelerated by the application of a weak linear relaxation to the pressure terms.

For a more detailed explanation of the mathematical and conceptual principles of PHOENICS, please refer to Bradbrook *et al.* (2000), Lane *et al.* (2002, 2004), or Ferguson *et al.* (2003).

3.4 DATA ANALYSIS

3.4.1 Objective 1

The first objective of the present study was to construct and evaluate a numerical model based on the Biron *et al.* (2004a;b; in press) laboratory experiments. To determine a mesh cell resolution that minimized solution time while retaining sufficient predictive performance, a series of mesh sensitivity analyses were performed for the two bed types (stable- and mobile-beds). Preliminary simulations were performed using ten different grids for each bed type. The maximum and minimum predicted values of dynamic pressure, velocity components, and kinetic energy from each simulation were compared to those from the mesh with the finest cell resolution. Following Bradbrook (2000), the optimal mesh was chosen as that which possessed the coarsest resolution (to reduce computing time) and predicted the maximum and minimum flow parameter values to within 10% of the values predicted using the finest mesh. In addition, a reduced major axis (RMA) regression was performed to compare flow predictions from all meshes to those from finest mesh so as to determine which grid had the coarsest resolution but the best correlation to the finest grid (following Hardy *et al.*, 2003) (see Section 4.1).

Once the appropriate mesh resolution was decided upon, the laboratory experiments could be simulated. As described in the previous section, various options are available pertaining to choice of coordinate system, incorporation of bed and water surface topography, deflector construction, and representation of pressure terms at the water surface. Therefore, for each laboratory setup, four and six simulations for stable- and mobile-beds, respectively, were performed (see Section 4.2 and 4.3). In all simulation sets, inlet, outlet, and invariable boundary conditions (i.e. wall function, no-slip conditions, and roughness height) were kept constant.

Following the analysis used in Lane *et al.* (2004) and Ferguson *et al.* (2003), predicted values of u, v, w, and ke from each simulation were compared to the corresponding laboratory measurements through forward (predicted vs. measured) and reverse (measured vs. predicted) ordinary least-squares (OLS) regression to establish the model's predictive capabilities (Ferguson *et al.*, 2003; Lane *et al.*, 2004).

Model performance was then discussed in relation to previous application of 3D-CFD from throughout the literature.

3.4.2 Objective 2

The second objective of the study was to use the numerical model to examine how the flow field around the deflectors is influenced by changes in the structures' size and orientation. To accomplish the objective, simulations were performed with deflector angles ranging from 30° to 150° and contraction ratios ranging from 0.10 to 0.35, again using constant inlet, outlet, and boundary conditions for each run.

Various properties of the flow field – including dynamic pressure maxima minima, and distribution; velocity magnitude amplification and distribution; upstream flow separation distance and separation zone width, and; vertical velocity (downwelling) distribution and magnitudes – were extracted from the simulations and plotted in order to establish trends based on the deflector angle and length. The characteristics of the flow field around deflectors were then compared to similar properties of the flow field around other obstructions (e.g. groynes, weirs, piers, abutments).

3.4.3 Objective 3

The third objective was to provide insight into the temporal dynamics of bed adjustment around deflectors. For the timeline flume runs, scour hole depth and planform dimensions were extracted based on the DEM created from the laboratory measurements at each time interval (5min, 30min, 120min, equilibrium). Additionally, the maximum depths recorded over the course of the run (see Section 3.1.3) were plotted and compared to the various predictive equations (Section 2.2.5) through OLS regression. Additional simulations were run reflecting the flow conditions from the timeline runs, and the properties of the flow field related to Objective 2 were compared against various scour hole dimensions. Ultimately, a method was developed to predict equilibrium scour hole extent based on a geometrical relationship amongst flow variables, culminating in the presentation of a conceptual model of scour hole development over time.

4. MODEL EVALUATION

4.0 PREFACE

With the increase in reliance and utilization of numerical models to examine open-channel flow problems, the focus throughout the recent literature has shifted away from simply establishing the validity of the models' underlying numerical scheme. It is now generally accepted that numerical simulations can be used effectively for a variety of situations, and thus the emphasis is no longer on attempting to have a computer 'successfully' solve a well-established set of equations (Bates *et al.*, 2005). Rather, increased rigor is now being directed towards a more systematic refinement of a model's design and construction rather than blindly accepting a solved set of equations within a discretized space.

As summarized by Hardy *et al.* (2003), an editorial in the American Society of Mechanical Engineers' (ASME) Journal of Fluids Engineering (Vol. 115: p.340) put forth a number of recommendations that must be adhered to in order for a numerical scheme to be deemed credible. The first such recommendation pertains to the necessity of performing and presenting the results of a modeling mesh sensitivity analysis. Such tests should be performed over a wide range of mesh resolutions so as to establish grid-independent or grid-convergent numerical solution (Hardy *et al.*, 2003). In essence, this ensures that any discrepancies between a model's output and the corresponding flow measurements will not be due to the manner in which the mesh has been constructed.

It is also important to note that, when using commercially available CFD software packages, a variety of extensions and simulation options are often available. Not only does the user need worry about mesh resolution, but, indeed, *how* the grid is constructed and the model applied. While the mesh has to be of 'optimum' resolution, the effect of various modeling practices must also be examined with respect to the desired output.

The question of evaluating a model's performance relates specifically to the second of the ASME recommendations, which states that while "comparison with reliable experimental results is appropriate, 'reasonable agreement' with experimental data alone will not be enough to justify a given single-grid calculation" (Hardy *et al.*, 2003, 1540). Such sentiments are echoed by Ferguson *et al.* (2003) and Bates *et al.* (2005), who state that the commonly accepted comparison of measured and predicted flow profiles is insufficient to validate a model's output because the various point measurements may not be fully representative of larger scale flow processes and structures. These authors proceed to call for a more rigorous testing of model data, suggesting that a more formal statistical analysis is required in order to assess a simulation's credibility.

It is therefore the purpose of the following chapter to address the first objective of the thesis – determining if a numerical model is capable of reproducing the three-dimensional flow field around a set of paired deflectors in a laboratory flume – with respect to the aforementioned guidelines. Section 4.1 presents the results of the grid independence tests for both the stable- and mobile-bed simulations, illustrating how changes to mesh cell resolution affect the model's predictions of various flow properties. The results from the sensitivity analysis are then used to determine the mesh dimensions to be used throughout the rest of the thesis by maximizing data resolution and precision (achieved by increasing grid-cell resolution) while minimizing computational time (achieved by decreasing grid-cell resolution).

Section 4.2 proceeds to evaluate the model's performance by comparing simulated flow variable predictions against the laboratory data through statistical analysis. As outlined in Section 3.2, a series of modeling approaches were applied based on the water surface treatment, bed construction, and deflector insertion. Each of these methods was tested independently against the laboratory measurements from Biron *et al.* (in press).

Section 4.3 begins with a general discussion of determining the 'appropriate' methods to evaluate a grid sensitivity analysis. Focus is then shifted to assessing the success of the model, ultimately comparing the results of the present study to other published flow models. Finally, the applicability of the object-bed for simulating flows over complex geometries is compared to the numerical porosity approach of Lane *et al.* (2002, 2004).

4.1 MESH SENSITIVITY ANALYSES

4.1.1 Stable Bed

In total, 10 flow simulations over a stable bed were performed using different mesh resolutions (Table 4-1). Each was performed for deflectors oriented at 135° installed within a Cartesian grid, with the PARSOL extension (see Section 3.2.3) having been activated. Bed roughness, inlet velocity, and inlet turbulence intensity were held constant for each run, and cell sizes were reduced accordingly in the regions where the most rapid change in flow conditions was expected to occur, namely near the bed, banks, and deflectors.

The number of cells in the x- (downstream), y- (lateral), and z- (vertical) directions were varied, as were the combinations thereof. As it is commonly held that an increase in the total number of grid cells results in more 'realistic' results (Hardy *et al.*, 1999), all simulations were compared against that which had the finest mesh: Stable Sensitivity (hereafter referred to as "SS") #10.

Following the method outlined in Bradbrook (2000), Figure 4-1 shows the effect of increasing the total number of grid cells on the maximum values of various flow parameters. The use of maximum values as benchmarks is justified as they indicate the full development of flow features; if a coarser grid is used, the maximum cell values should be reduced due to the averaging of flow variables over a larger spatial domain (Bradbrook, 2000). Thus, any discrepancy of less than 10% between the outputs from a given grid and the finest grid is considered acceptable (*ibid.*).

Table 4-1: Dimensions of modeling meshes used for the stable-bed sensitivity analysis, where *nx*, *ny*, and *nz* are the number of grid cells in the downstream, lateral, and vertical directions, respectively.

Simulation	nx	ny	nz	Total Cells
SS1	85	12	10	10,200
SS2	100	25	10	25,000
SS3	100	25	20	50,000
SS4	165	35	10	57,750
SS5	165	25	15	61,875
SS6	165	40	10	66,000
SS7	165	35	12	69,300
SS8	165	25	20	82,500
SS9	165	50	10	82,500
SS10	250	35	10	87,500

Figure 4-1: Effect of varying stable-bed grid dimensions on maximum and minimum flow variables. (*P* – pressure; *u* – downstream velocity; *v* – lateral velocity; *w* – vertical velocity; *ke* – turbulent kinetic energy). Dotted lines indicate +/- 10% variation from the finest resolution.

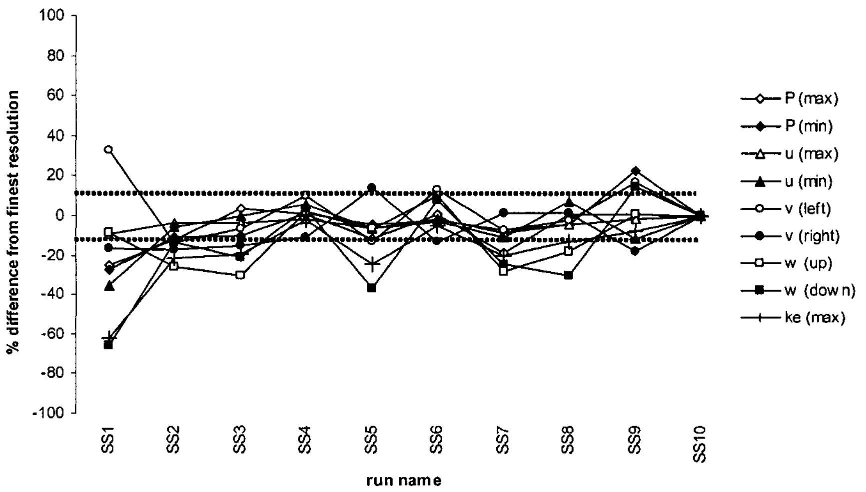

Increasing the total number of cells in the domain has a noticeable effect on all flow variables except for maximum downstream velocity, which varies by less than 10% from the finest resolution in all cases, and minimum downstream velocity, which is outside the boundary for only the coarsest mesh. Except for SS1 (the coarsest mesh), values of maximum and minimum hydrodynamic pressure lie outside the 10% boundaries in only one case each – SS7 (-18.7%) and SS9 (+22.7%), respectively – while lateral velocity components differ for cases SS2 (-13.6% and -17.7% for left and right, respectively) and SS9 (+16.4% and -18.3%, respectively), indicating relative insensitivity of these variables to mesh resolution.

The parameters that appear to be the most sensitive to grid resolution are the vertical velocity components and kinetic energy, as each is underestimated in cases SS2 (-26.1%, -23.5%, and -21.4%, for maximum vertical velocity, minimum vertical velocity, and kinetic energy, respectively), SS3 (-30.4%, -20.7%, and -19.6%, respectively), SS7 (-27.9%, -24.9%, and -20.4%, respectively), and SS8 (-17.8%, -30.1%, and -13.2%, respectively). Additionally, the downward component of vertical velocity is overestimated slightly in case SS9 (+14.7%).

In only two cases, runs SS4 and SS6, do all parameters lie within the +/- 10% threshold. In order to further investigate the level of agreement between these two meshes and the finest mesh, simulation output of flow variables were extracted from the cells corresponding to the locations where measurements were taken in the laboratory. This was done to examine the potential influence of grid definition on the comparison to laboratory data (Section 4.2). Following Hardy *et al.* (2003), a Reduced Major Axis (RMA) regression was performed between the output of SS4 on SS10, SS6 on SS10 (Table 4-2). The RMA was used instead of an ordinary least-squares (OLS) regression as potential error exists in both the dependent and independent variables, whereas a simple least-squares linear regression assumes error in only the dependent variable. Although all simulations converged, the accuracy of the solutions is unknown, and thus the RMA accounts for the potential errors in both variables and provides the regressions slope as the ratio of the standard deviation of the y-variable to the standard deviation of the x-variable (Hardy *et al.*, 2003).

Both SS4 and SS6 yield a strong correlation to SS10 for all flow variables, evidenced by a minimum correlation coefficient (r) of 0.969 (ke – SS4:SS10). Both meshes perform equally well in terms of downstream and lateral velocity, while SS4 performs marginally better in relation to vertical velocity and SS6 has a stronger correlation for turbulent kinetic energy.

Table 4-2: RMA regression prediction of slope (*b*) between variables and the correlation coefficient (*r*) for stable-bed meshes (*u* – downstream velocity, *v* – lateral velocity, *w* – vertical velocity, and *ke* – turbulent kinetic energy)

Variable	SS4 against SS10		SS6 against SS10	
	r	RMA (b)	r	RMA (b)
u	0.987	0.973	0.987	1.028
v	0.991	0.999	0.994	1.034
w	0.979	1.052	0.978	1.016
ke	0.969	0.881	0.973	0.991

Figure 4-2: A comparison of simulation outputs between runs SS6 and SS10 for: (a) downstream velocity component – *u*; (b) lateral velocity component – *v*; (c) vertical velocity component – *w*; and (d) turbulent kinetic energy – *ke*. Diagonal line indicates 1:1 relationship.

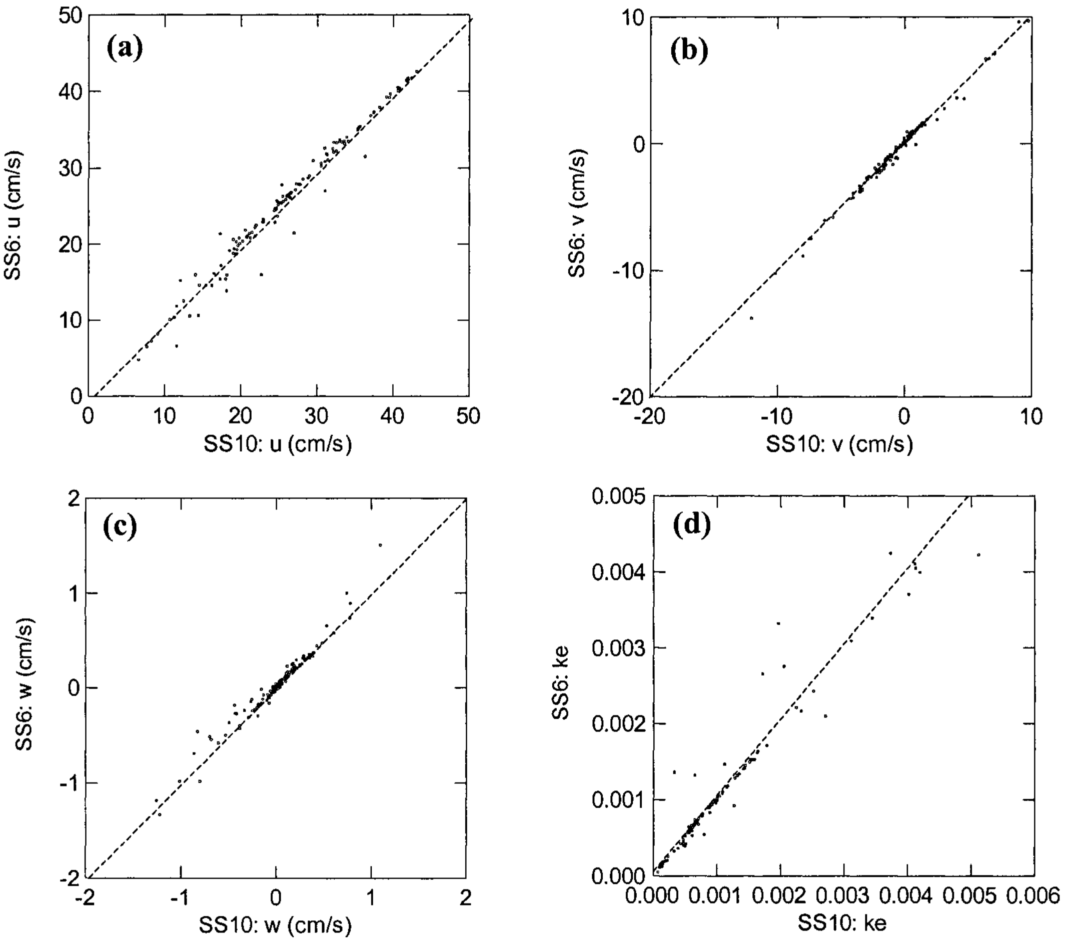

Mesh SS4 produces a regression slope closer to unity for both the downstream and lateral velocities, though only marginally so for the downstream component. Meanwhile, SS6 has slopes much closer to unity for vertical velocity and turbulent kinetic energy. For these variables, the slopes of the SS4 regression lines differ significantly from unity.

Because all maximum flow variables from SS6 differed by less than 10% from the finest mesh, the flow features can be considered fully developed (Bradbrook, 2000). Although this was also the case for SS4, the RMA results indicate a better level of agreement between SS6 and the finest grid (illustrated in

Figure 4-2) than for SS4. Therefore, it was decided that all subsequent simulations over a flat bed would be carried out using grids with the SS6 dimensions of 165*40*10 cells in the x-, y-, and z-directions, respectively.

4.1.2 Mobile Bed

Ten separate simulations were also performed for the mobile-bed sensitivity analysis, with the grid dimensions of each provided in Table 4-3. The simulations were performed for flow around 'pixelated' 90° deflectors in a BFC domain, with the porosity treatment applied to a flat water surface. Hereafter, these runs are referred to as MS1-MS10, or 'Mobile Sensitivity' runs one through ten.

Figure 4-3 illustrates the effect of increasing the total number of cells within the modeling domain on the maximum and minimum values of dynamic pressure, downstream, lateral, and vertical velocity, and kinetic energy. As in the stable-bed cases, the maximum downstream velocity is within the 10% range for all grid resolutions. However, the minimum downstream velocity is greatly underestimated in all cases. In all but one simulation (MS5), maximum hydrodynamic pressure lies within the acceptable boundaries, and at that, just exceeds the limit (+15.7%). Minimum pressures, though, are slightly more sensitive at lower resolutions, only staying within the 10% limits including and beyond the resolution of run MS5. Lateral velocity components are also sensitive at lower resolutions but converge at

Table 4-3: Dimensions of modeling meshes used for the mobile-bed sensitivity analysis, where *nx*, *ny*, and *nz* are the number of grid cells in the downstream, lateral, and vertical directions, respectively.

Simulation	nx	ny	nz	Total Cells
MS1	72	11	5	3960
MS2	81	21	12	20,412
MS3	81	41	12	39,852
MS4	164	21	12	41,328
MS5	164	30	12	59,040
MS6	123	41	12	60,516
MS7	164	40	10	65,600
MS8	164	40	15	98,400
MS9	164	40	20	131,200
MS10	198	55	15	163,350

Figure 4-3: Effect of varying mobile-bed grid dimensions on maximum and minimum flow variables. (*P* – pressure; *u* – downstream velocity; *v* – lateral velocity; *w* – vertical velocity; *ke* – turbulent kinetic energy). Dotted lines indicate +/- 10% variation from the finest resolution

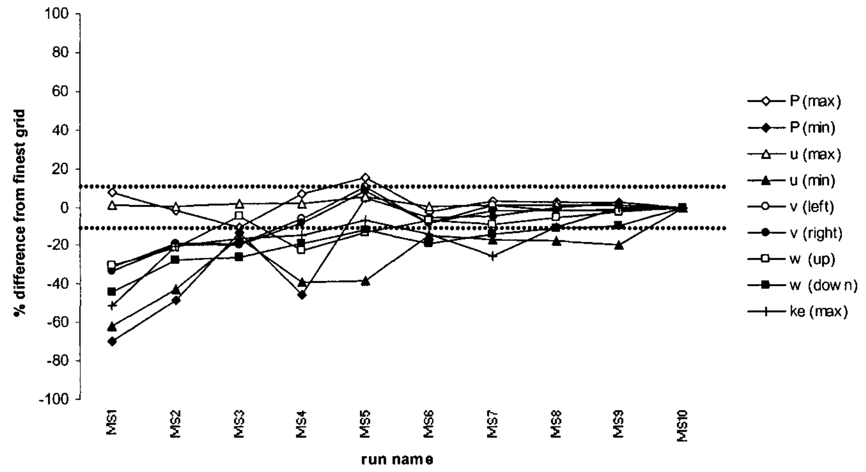

MS4, remaining within +/- 10% for all finer grids and differing by less than 2% from MS7 onwards. Independence is achieved for upwards vertical velocity at MS6 (-6.8%), after which it varies by approximately 4% for the remaining simulations. As was the case with the stable-bed simulations, the most sensitive parameters were downward vertical velocity and turbulent kinetic energy. Both are consistently underestimated for grids of resolution lower than that of MS8, except for kinetic energy in MS4 (-6.6%).

Because no grids were within the +/- 10% range for all flow variables, an RMA regression was conducted on the model outputs from laboratory measurement locations between each mesh and the finest grid (MS10). Consistently, it was found that runs MS8 and MS9 performed most adequately (Table 4-4).

In both cases, the correlation for downstream velocity (*u*) is quite good, with *r* values ranging from 0.957 (MS9) to 0.990 (MS8). The regression slopes, however, indicate that MS9 slightly, but significantly, yields overpredictions. Lateral velocity (*v*) correlation is also good, ranging from 0.978 (MS9) to 0.995 (MS8). For this variable, however, all slopes are significantly greater than unity. Correlation values for vertical velocity are slightly less favorable, with a maximum value of 0.976

Table 4-4: Mobile-bed RMA regression prediction of slope (*b*) between variables and the correlation coefficient (*r*); (*u* – downstream velocity, *v* – lateral velocity, *w* – vertical velocity, and *ke* – turbulent kinetic energy).

Variable	MS8 against MS10		MS9 against MS10	
	r	RMA (b)	*r*	RMA (b)
u	0.990	1.009	0.957	1.096
v	0.995	1.109	0.978	1.302
w	0.976	0.993	0.931	1.156
ke	0.991	0.965	0.904	1.039

(MS8). As was the case for *u*, the slope of the MS9 *w* regression shows a slight but significant overprediction. Both meshes also exhibit good correlation for kinetic energy, with *r* values of 0.991 and 0.904 for MS8 and MS9, respectively, while the slope of the MS8:MS10 regression line being slightly closer to unity.

For all variables, the correlation coefficient was higher and the regression slope closer to unity for mesh MS8 than MS9 (Figure 4-4). It was therefore decided that all subsequent simulations over a mobile bed would be performed with the MS8 dimensions of 164*40*15 cells.

4.2 COMPARISON OF MODEL OUTPUT AGAINST LABORATORY DATA

4.2.1 Stable Bed

As discussed in Section 3.2, there are various methods of incorporating the deflectors, water surface topography, and water surface pressure terms. Therefore, a total of six combinations were available to simulate each stable-bed laboratory run (Table 4-5).

For each simulation, the output of flow variables from the grid cells corresponding to the laboratory measurements locations were extracted and compared against the flume data for the three velocity components and kinetic energy. Although all simulations were performed for steady flow, and thus all flow properties can be considered time-averaged, kinetic energy was included in the analysis because its successful prediction would justify the choice of turbulence model (Ferguson *et al.*, 2003).

Figure 4-4: A comparison of simulation outputs between runs MS8 and MS10 for: (a) downstream velocity component – *u*; (b) lateral velocity component – *y*; (c) vertical velocity component – *w*; and (d) turbulent kinetic energy – *ke*. Diagonal line indicates 1:1 relationship.

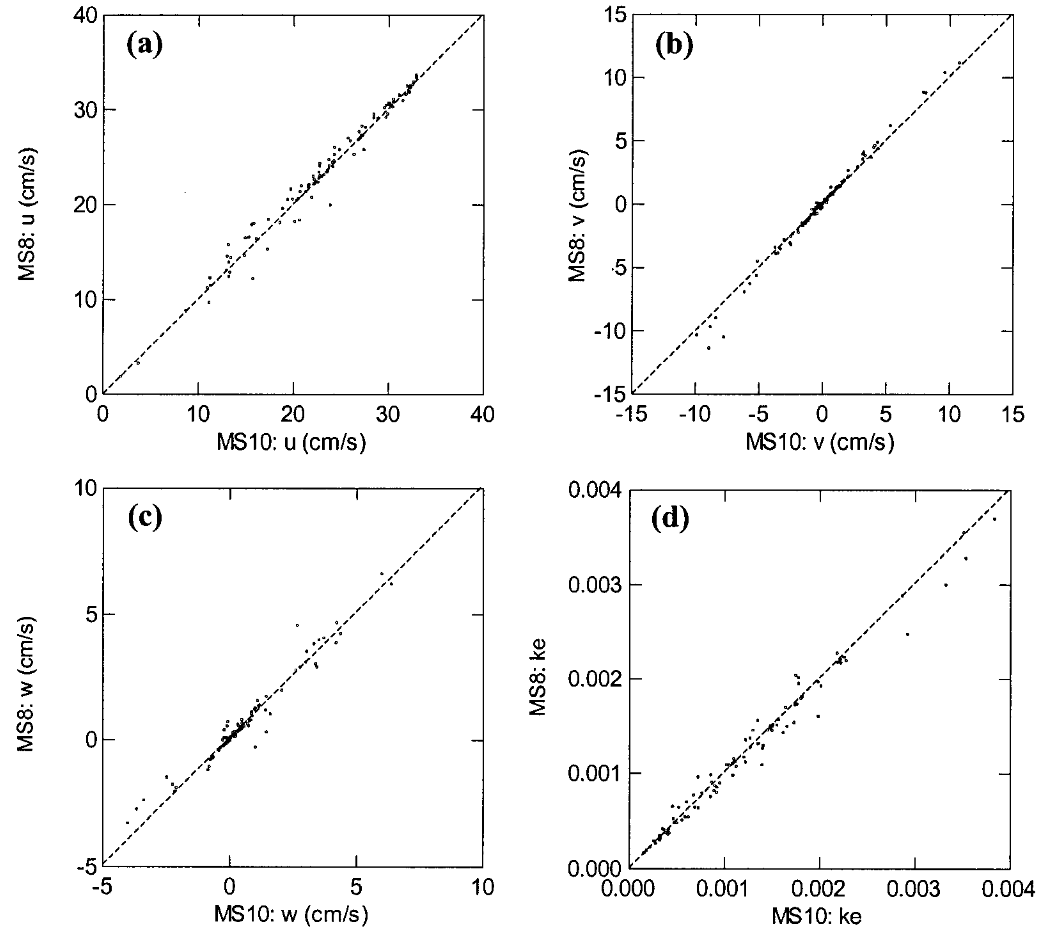

Coefficients of determination (r^2) between predicted and measured flow variables are presented in Table 4-6. Surprisingly, for all three angles, runs S3 and S5 showed no difference from S4 and S6, respectively, indicating that activating the porosity algorithm produced no effect on the model's predictions. This finding was subsequently confirmed by a further review of the regression outputs. As a result, stable-bed runs that incorporated porosity will be eliminated from individual discussion henceforth.

Table 4-5: Stable-bed simulation combinations of coordinate system, water surface topography (WST), deflector insertion method, and water surface pressure treatment. WST indicates whether or not water surface topography was incorporated into the modeling mesh geometry.

Option	Coordinate System	Bed	WST?	Deflectors	Water Surface
S1	Cartesian	plate	No	PARSOL	Rigid Lid
S2	Cartesian	plate	No	Pixelated	Rigid Lid
S3	BFC	surface-wrapped	No	Pixelated	Rigid Lid
S4	BFC	surface-wrapped	No	Pixelated	Porosity
S5	BFC	surface-wrapped	Yes	Pixelated	Rigid Lid
S6	BFC	surface-wrapped	Yes	Pixelated	Porosity

In general, the level of agreement between predicted and measured downstream (u) and lateral (v) velocity is comparable within each simulation option, though pronounced differences can be seen between options. In most cases, slightly higher r^2 values for u were evident, with values ranging from 0.688-0.708 for the 45° runs, 0.803-0.886 for the 90° runs, and 0.764-0.792 for the 135° runs. For v, r^2 values range from 0.611-0.762 for the 45° simulations, 0.822-0.898 for the 90° simulations, and 0.691-0.793 for the 135° simulations.

While simulations performed in BFC space (S3 and S5) tend to show slightly better agreement for u and v than do those performed using a Cartesian mesh (S1 and S2), there is no obvious trend as to whether or not incorporating water surface topography into the mesh's geometry aided the model's ability to predict these components. Specifically, run 45S3 outperformed 45S5 while run 90S5 outperformed 90S3, and no clear difference was exhibited between runs 135S3 and 135S5.

For all angles and simulation options, much lower levels of agreement were found for the vertical velocity component (w) and kinetic energy (ke) than were found for u and v. Values of r^2 for w range from 0.329-0.506 in the 45° simulations, from 0.093-0.321 for 90° simulations, and from 0.115-0.289 for 135° simulations. Kinetic energy also exhibits low r^2 values, ranging from 0.255-0.533 for the 45° runs, 0.129-0.439 for the 90° runs, and 0.358-0.460 for the 135° runs.

Table 4-6: Coefficient of determination (r^2) values between predicted and measured flow variables in the stable-bed simulations. The number preceding the simulation name corresponds to the respective deflector angle, while the following numbers correspond to the simulation option (Table 4-5). Flow variables (*u, v, w, ke*) are as defined in Table 4-4.

Run	variable	r^2	Run	variable	r^2	Run	variable	r^2
	u	0.608		*u*	0.803		*u*	0.764
45S1	*v*	0.611	90S1	*v*	0.823	135S1	*v*	0.691
	w	0.402		*w*	0.321		*w*	0.115
	ke	0.255		*ke*	0.129		*ke*	0.417
	u	0.739		*u*	0.804		*u*	0.794
45S2	*v*	0.697	90S2	*v*	0.822	135S2	*v*	0.731
	w	0.506		*w*	0.314		*w*	0.289
	ke	0.377		*ke*	0.223		*ke*	0.358
	u	0.788		*u*	0.855		*u*	0.792
45S3	*v*	0.762	90S3	*v*	0.898	135S3	*v*	0.753
	w	0.329		*w*	0.164		*w*	0.115
	ke	0.533		*ke*	0.439		*ke*	0.460
	u	0.788		*u*	0.855		*u*	0.792
45S4	*v*	0.762	90S4	*v*	0.898	135S4	*v*	0.753
	w	0.329		*w*	0.164		*w*	0.115
	ke	0.533		*ke*	0.439		*ke*	0.460
	u	0.753		*u*	0.886		*u*	0.792
45S5	*v*	0.750	90S5	*v*	0.866	135S5	*v*	0.740
	w	0.493		*w*	0.093		*w*	0.130
	ke	0.520		*ke*	0.402		*ke*	0.455
	u	0.753		*u*	0.886		*u*	0.792
45S6	*v*	0.750	90S6	*v*	0.866	135S6	*v*	0.740
	w	0.493		*w*	0.093		*w*	0.130
	ke	0.520		*ke*	0.402		*ke*	0.455

As was the case for *u* and *v*, BFC simulations exhibited a slightly better correlation with measured values of *ke* than did Cartesian simulations. For *ke*, however, run S3 outperformed run S5 for all angles. Conversely, vertical velocity tended to be better predicted by Cartesian simulations than by BFC simulations. For all angles, run S2 had a better *w*-correlation than did run S1.

Correlation values between predicted and measured variables represents the amount of scatter in the data, but they do not indicate a lack of bias. Rather, correlation coefficients are used to determine the *precision* of a model only, and hence its *accuracy* must also be evaluated (Bates *et al.*, in press). Therefore, "forward" (predicted vs. measured) and "reverse" (measured vs. predicted) ordinary least squares regressions (OLS) were also performed. As outlined in Ferguson *et al.* (2003), the two regression lines provide limits to the range of best possible fits between the two data sets, and thus simulation bias can be considered acceptable if the line of equality (1:1 fit) lies between the two regression lines.

Forward and reverse OLS regressions were performed instead of RMA regressions as the latter are only appropriate when it can reasonably be assumed that the error in both data sets are the same (Bates *et al.*, in press). Although this was the case for the mesh sensitivity analysis – where both errors were due to modeling issues – the nature of the data now being analyzed indicate that error sources for ADV measurements will differ from those responsible for modeling error.

OLS regression slopes for predicted and measured flow properties are shown in Figure 4-5. In all but a few cases – 45S1, 45S2, and 135S2 – the line of equality is bounded by the forward and reverse regression slopes for the *u*-component. For *v*, slopes were adequately predicted for all of the 90° simulations as well as the S2 runs for 45° and 135°. Slopes for *w* were acceptable in all but a few runs – 90S5, 135S3, and 135S5. Finally, no S1 slopes bounded the line of equality for *ke*, nor did the 45° S2 and S5 simulations.

That most of the forward *u*-regression slopes for the 45° and 90° simulations were significantly less than unity indicates that the model consistently overpredicted measured values that were close to zero. Such a bias is reflected by strongly positive-skewed regression y-intercepts – illustrated in Table 4-7 – where intercept values range from 5.00-9.56 cm/s. Although the intercepts of the other three variables differ significantly from zero in several cases, the magnitudes are always less than 0.75cm/s, 0.63cm/s, and 1.18 kg $m^{-1}s^{-1}$ for *v*, *w*, and *ke*, respectively. While, statistically, it may indicate a slight problem with the model, pragmatically it has little impact. Therefore, the remainder of the discussion will focus on the bias exhibited in the *u*-regressions.

The apparent inability of the model to accurately predict zero-intercepts for *u* may be potentially misleading. Figure 4-6 shows predicted vs. measured downstream velocity for each angle, with the results of all simulation options amalgamated. Values are plotted with a LOWESS smoother of tension 0.500. As can be seen,

Table 4-7: Forward and reverse OLS regression y-intercepts for the stable-bed simulations. Bold values indicate cases where the intercept is not significantly different from zero at the 95% confidence level.

		45°		90°		135°	
	Variable	forward	reverse	forward	reverse	forward	reverse
	u	6.53 ± 1.55	4.20 ± 1.50	6.59 ± 1.36	**-1.26 ± 1.45**	**-1.00 ± 1.41**	6.25 ± 0.94
S1	*v*	0.43 ± 0.17	0.34 ± 0.14	-0.63 ± 0.15	0.74 ± 0.14	**0.24 ± 0.15**	**0.28 ± 0.15**
	w	-0.11 ± 0.02	0.32 ± 0.05	0.15 ± 0.03	-0.62 ± 0.07	**0.04 ± 0.03**	**0.15 ± 0.08**
	ke	0.41 ± 0.12	0.73 ± 0.17	0.66 ± 0.15	1.33 ± 1.33	**0.26 ± 0.15**	0.86 ± 0.17
	u	7.19 ± 1.11	-0.56 ± 1.38	5.48 ± 0.89	**-1.48 ± 1.36**	5.50 ± 1.20	**-0.26 ± 1.46**
S2	*v*	0.30 ± 0.13	0.29 ± 0.12	-0.51 ± 0.12	0.74 ± 0.15	**-0.12 ± 0.13**	**-0.20 ± 0.15**
	w	-0.12 ± 0.02	0.35 ± 0.05	0.12 ± 0.02	-0.63 ± 0.07	**-0.07 ± 0.03**	0.27 ± 0.07
	ke	0.34 ± 0.11	0.58 ± 0.15	0.40 ± 0.11	1.18 ± 0.23	0.30 ± 0.11	0.82 ± 0.17
	u	8.28 ± 0.90	-3.86 ± 1.36	5.00 ± 0.74	-2.13 ± 0.99	**-0.58 ± 1.21**	5.34 ± 0.91
S3	*v*	**0.20 ± 0.11**	**0.21 ± 0.11**	**0.09 ± 0.10**	**-1.02 ± 0.11**	**-0.20 ± 0.13**	**-0.23 ± 0.13**
	w	-0.06 ± 0.02	0.29 ± 0.06	**0.00 ± 0.03**	0.24 ± 0.07	0.09 ± 0.04	**0.13 ± 0.08**
	ke	0.30 ± 0.10	0.357 ± 0.14	0.36 ± 0.10	0.66 ± 0.21	0.33 ± 0.11	0.64 ± 0.17
	u	9.56 ± 0.97	-4.13 ± 1.52	5.99 ± 0.69	-3.71 ± 0.92	**-0.26 ± 1.23**	5.10 ± 0.92
S5	*v*	**0.21 ± 0.11**	**0.22 ± 0.11**	**0.10 ± 0.10**	**0.13 ± 0.12**	**0.19 ± 0.13**	**0.23 ± 0.14**
	w	-0.16 ± 0.02	0.40 ± 0.05	-0.17 ± 0.06	0.33 ± 0.07	0.07 ± 0.03	**0.13 ± 0.08**
	ke	0.24 ± 0.15	0.51 ± 0.13	0.53 ± 0.14	0.73 ± 0.22	0.36 ± 0.12	0.65 ± 0.17

regression slopes are underestimated and intercept values tend to be positively skewed due to a strong overprediction of *u* where measurements were lower than approximately 12cm/s. The smoother line illustrates that the trend for values in this region is virtually horizontal, meaning that there is no significant relationship between predicted and measured values. For the 135° runs, the scatter around the line of equality is more evenly divided between over- and under-predictions. Therefore, the intercept for the 135° *u*-regressions is closer to zero.

Visual inspection revealed that the vast majority of these points were located within the shearing region just downstream of the deflector nose. That the model so greatly overpredicted velocities in this region shows that the width of the recirculation zone is slightly underpredicted. In essence, the model is presuming that these points should be within the acceleration zone closer to the center of the channel – reflected by the high predicted velocity values – whereas the low measured velocities dictate

Figure 4-5: Plot of forward and reverse regression slopes for stable-bed simulations of (a) u; (b) v; (c) w; and (d) ke. Dotted line indicates a slope of unity. Error bars indicate standard error of regression slopes.

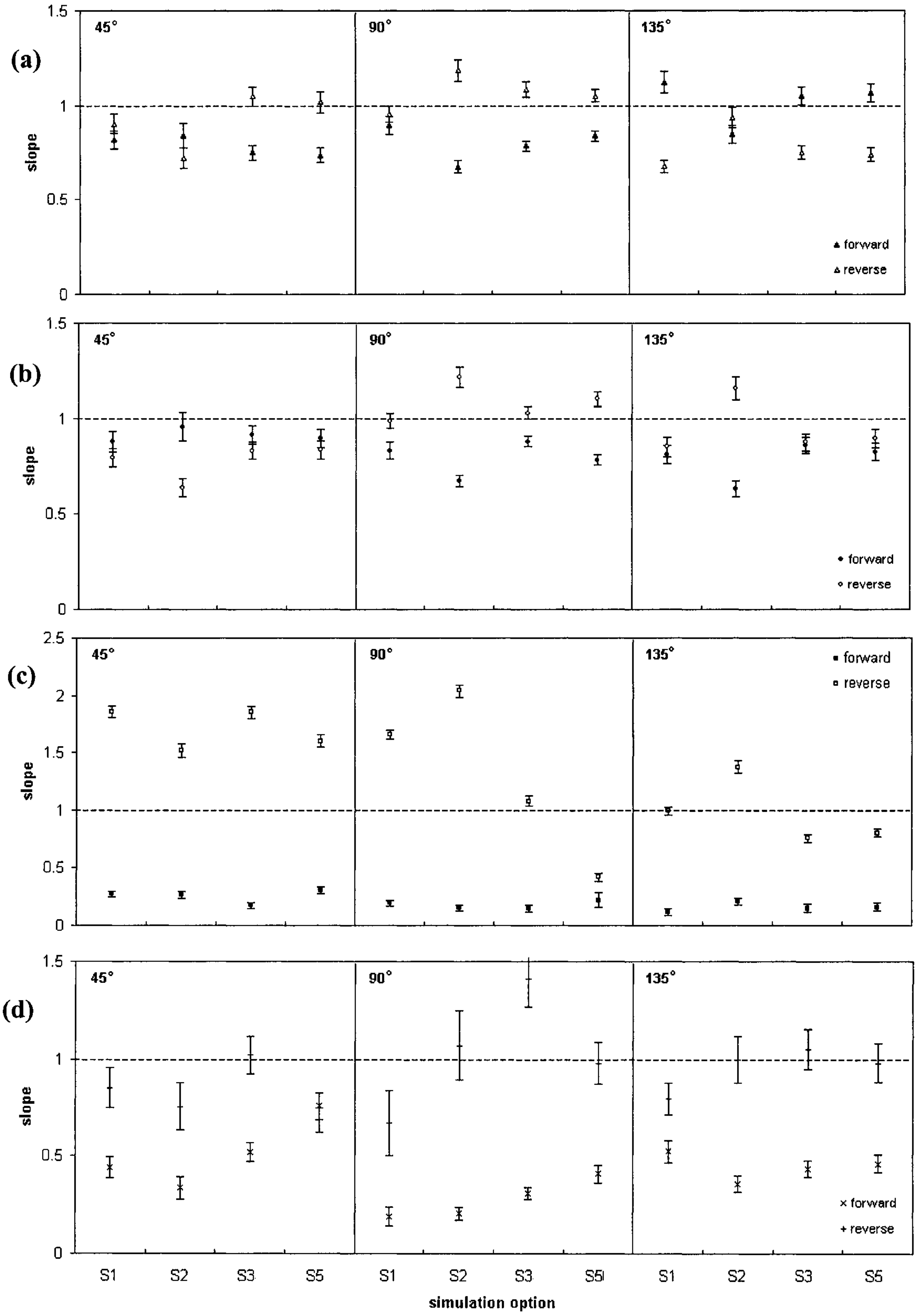

Figure 4-6: Predicted vs. measured downstream velocity component (*u*), including data from all stable-bed options for each angle. Dotted line indicates line of equality. Graphs on right-hand side show only measured values less than 15cm/s. Solid line represents LOWESS smoother.

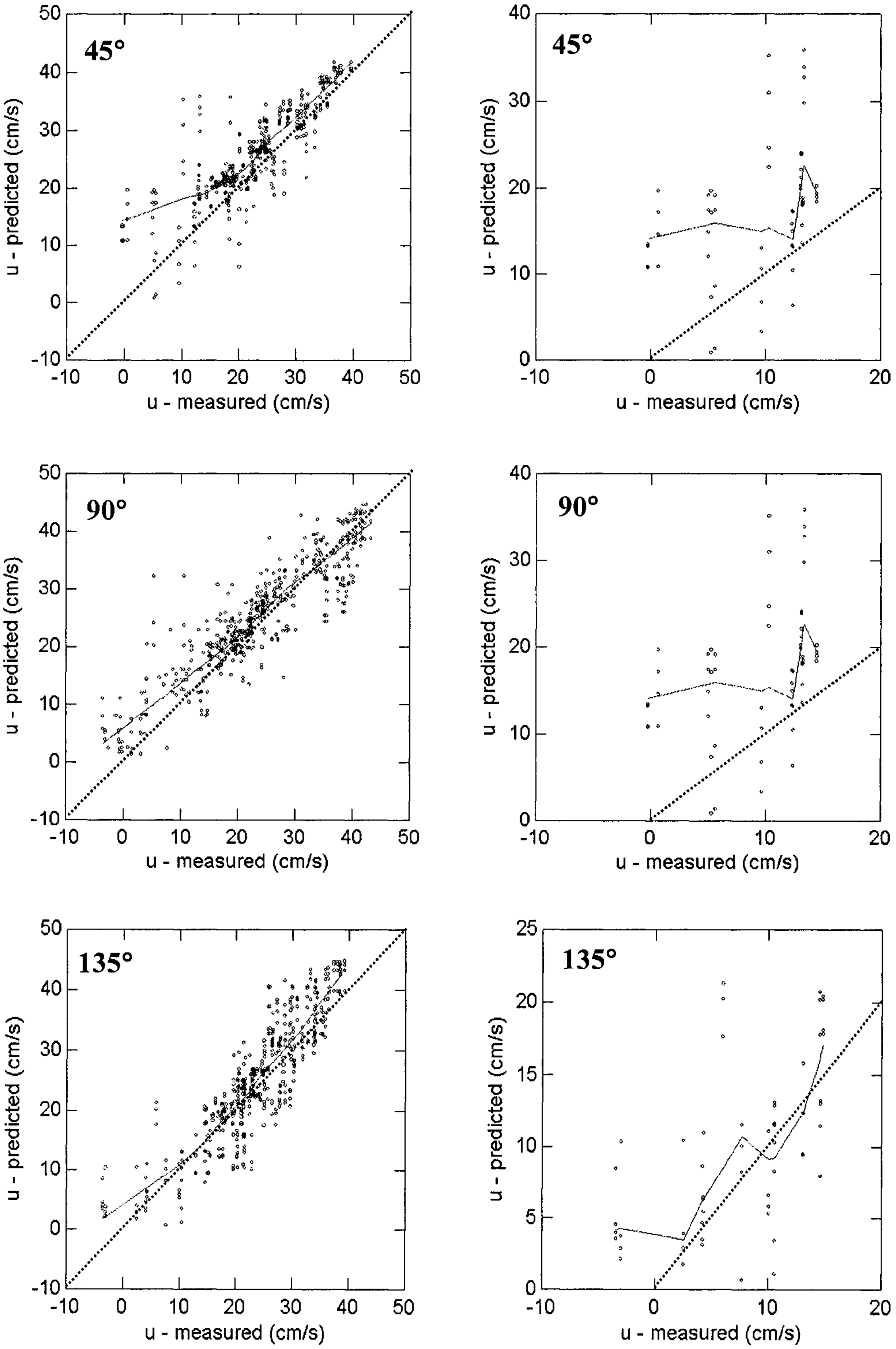

that they are actually within the adjacent low-speed zone. Had the model's recirculation zone been slightly wider, it likely would have encapsulated these points, thereby eliminating the apparent overpredictions.

A number of factors could have contributed to the inability to accurately predict velocity magnitudes near the shearing zone. First, the measurement locations may have been slightly misread on the slide rail gauge in the laboratory, and were possibly closer to the bank than reported. Doing so would erroneously locate these points strictly within the recirculation zone and result in the model's overprediction. In addition, the modeling mesh cell centers – where the flow equations are solved – did not perfectly match the reported measurement locations (±0.3cm). Therefore, the volume of the cell used in the calculations may have been more within the acceleration zone than the recirculation zone, which would result in erroneously high velocity predictions. Finally, because only steady-state simulations were performed, the oscillatory nature of the shearing zone could not be accounted for. Specifically, shearing zones downstream of obstructions have been shown to migrate laterally (Fang *et al.*, 1997), meaning that the width of the adjacent recirculation zone varies with time. Because the model is displaying time-averaged properties only, it is not possible to reproduce the time dependency on the shearing zone location.

Moreover, the y_w^+ criterion was violated just downstream of the deflectors, with values as low as 10 being found As discussed in Section 3.3.3, y_w^+ should be between 30 and 300 (Lane *et al.*, 2002), implying that cell heights in this region should have been increased in order to satisfy $30 < y_w^+ < 300$. However, because it is impossible to alter structured grid cell heights in one region without doing so throughout the domain, attempts to do so resulted in a great loss of information close to the bed throughout the rest of the channel. Because the problem occurred in this region only and attempts to fix it resulted in negative impacts elsewhere, the simulations were deemed acceptable provided that the violation in this region is taken into account for future analyses (Stuart Lane, *personal communication*).

Based on the regression r^2, slope, and intercept values, it is apparent that Options S2 and S3 were best able to predict the flow properties of interest. Options S1 and S5 were least able to satisfy the slope requirements, with five of 15 regression sets plotting beneath the line of equality; Options S2 and S3 were insufficient in only three cases each. Bates *et al.* (2005) state that after model evaluation, the user must decide upon the most practical methods to use the model for future applications. Therefore, although Option S3 may have marginally outperformed S2, the ease of deflector construction, insertion, and modification into Cartesian grids warrants S2 to be deemed more appropriate. Therefore, all subsequent simulations over stable beds were performed using the S2 guidelines.

4.2.2 Mobile Bed

For the mobile bed simulations, a total of four options were available based on the methods used to incorporate bed topography and water surface pressure terms (Table 4-8). Unlike the stable-bed cases, water surface topography data were not available and thus mobile-bed corollaries to runs S5 and S6 could not be created. It should be noted that for the Cartesian case when PARSOL was activated (M1), partial cell volumes are used in calculations both at the bed and around the deflectors based on the percentage of the cell that is physically obstructed (see Section 3.2.3 for more detail).

Coefficients of determination (r^2) for each flow variable and option are shown in Table 4-9. As can be seen, a slightly lower level of agreement for all variables and angles is evident for the mobile bed runs than for the stable-bed cases. The r^2 values of predicted vs. measured u range from 0.527-0.690 for the 45° runs, from 0.515-0.650 for the 90° runs, and from 0.458-0.622 for the 135° runs. No single option performed the best over all of the angles, while Option M1 performed the least adequately in two of three cases.

Table 4-8: Mobile-bed simulation combinations of coordinate system, water surface topography (WST), deflector insertion method, and water surface pressure treatment.

Option	Coordinate System	Bed	WST?	Deflectors	Water Surface
M1	Cartesian	object-bed	No	PARSOL	Rigid Lid
M2	Cartesian	object-bed	No	Pixelated	Rigid Lid
M3	BFC	surface-wrapped	No	Pixelated	Rigid Lid
M4	BFC	surface-wrapped	No	Pixelated	Porosity

Table 4-9: Coefficient of determination (r^2) values for predicted and measured flow variables in mobile-bed simulations. The number preceding the simulation name corresponds to the respective deflector angle, while the following numbers correspond to the simulation option (Table 4-8). Flow variables (*u, v, w, ke*) are as defined in Table 4-4.

Run	variable	r^2	Run	variable	r^2	Run	variable	r^2
45M1	*u*	0.567	90M1	*u*	0.515	135M1	*u*	0.458
	v	0.522		*v*	0.124		*v*	0.495
	w	0.219		*w*	0.223		*w*	0.313
	ke	0.040		*ke*	0.001		*ke*	0.006
45M2	*u*	0.690	90M2	*u*	0.576	135M2	*u*	0.577
	v	0.528		*v*	0.190		*v*	0.263
	w	0.233		*w*	0.331		*w*	0.176
	ke	0.012		*ke*	0.001		*ke*	0.003
45M3	*u*	0.527	90M3	*u*	0.574	135M3	*u*	0.622
	v	0.684		*v*	0.285		*v*	0.523
	w	0.583		*w*	0.244		*w*	0.454
	ke	0.021		*ke*	0.000		*ke*	0.011
45M4	*u*	0.528	90M4	*u*	0.650	135M4	*u*	0.610
	v	0.687		*v*	0.265		*v*	0.526
	w	0.580		*w*	0.252		*w*	0.435
	ke	0.024		*ke*	0.001		*ke*	0.008

A much greater variation can be seen in the model's ability to predict lateral velocities (v), with r^2 values ranging from 0.522-0.687 for the 45° runs, 0.124-0.285 for the 90° runs, and 0.263-0.526 for the 135° runs. For all angles, the BFC options (M3 and M4) more adequately predicted v, though neither did so consistently.

The agreement between predicted and measured w was generally comparable to those found for the stable-bed simulations, though they were slightly lower in some cases. Values of r^2 range from 0.219-0.583 for the 45° runs, 0.223-0.331 for the 90° runs, and 0.176-0.454 for the 135° runs. Again, no single option was best able to predict w, although the BFC runs were better for two of three angles.

The greatest difference in model performance between the stable- and mobile-bed cases is seen for *ke*. Kinetic energy r^2 values were close to zero in all cases, with none of the regressions showing a significant relationship between predicted and measured values. Consequently, *ke* will be eliminated from discussion for the remainder of this section.

Forward and reverse OLS regression slopes are presented in Figure 4-7. For only a handful of variables in certain cases did the slopes bound the line of equality, with the BFC runs (M3 and M4) generally outperforming the object-bed simulations (M1 and M2). For downstream velocity, three simulations satisfied the necessary criterion when including the standard error bar (45M3, 45M4, and 90M4). All options for the 45° runs were sufficient for *v*, as were the M3 and M4 runs for 135°. Finally, M3 and M4 runs were satisfactory for the 45° and 135° predictions of *w*, as was 135M1.

Similar to the stable-bed simulations, the strong underprediction of forward regression slopes for *u* is reflected by strongly positive-skewed regression intercepts (Table 4-10), where values ranged from 4.80-10.19 cm/s. For all simulations, the intercepts for *v* did not differ significantly from zero, while intercepts for *w* did so in only a few cases. However, the intercept magnitudes for the *w*-regressions were less than 0.50 cm/s in all but one case (90M3-reverse), and thus the following discussion will focus on the *u*-regressions.

Table 4-10: Forward and reverse OLS regression y-intercepts (cm/s) for mobile-bed simulations. Bold values indicate cases where the intercept is not significantly different from zero at the 95% confidence level.

		45°		90°		135°	
	Variable	forward	reverse	forward	reverse	forward	reverse
M1	*u*	9.34 ± 1.02	**0.84 ± 1.54**	7.92 ± 1.12	**2.31 ± 1.65**	9.93 ± 1.08	3.45 ± 1.48
	v	**0.22 ± 0.12**	**-0.24 ± 0.17**	**-0.37 ± 0.29**	**0.32 ± 0.25**	**0.21 ± 0.14**	**-0.11 ± 0.16**
	w	**-0.11 ± 0.13**	**0.00 ± 0.083**	**0.24 ± 0.17**	**-0.12 ± 0.11**	**0.11 ± 0.12**	**-0.10 ± 0.06**
M2	*u*	6.84 ± 0.94	**0.41 ± 1.21**	5.76 ± 1.20	3.43 ± 1.40	4.80 ± 1.15	5.20 ± 1.06
	v	**0.04 ± 0.12**	**-0.05± 0.17**	**-0.11 ± 0.28**	**0.20 ± 0.24**	**0.11 ± 0.13**	**0.00 ± 0.51**
	w	-0.23 ± 0.10	**0.06 ± 0.08**	**0.27 ± 0.14**	**-0.12 ± 0.10**	**0.17 ± 0.10**	**-0.13 ± 0.07**
M3	*u*	10.19 ± 1.66	4.42 ± 1.39	3.79 ± 1.19	5.09 ± 1.29	6.41 ± 1.05	2.69 ± 1.14
	v	**0.13 ± 0.14**	**0.22 ± 0.19**	**0.11 ± 0.29**	**-0.03 ± 0.23**	**0.17 ± 0.10**	**0.24 ± 0.151**
	w	**0.04 ± 0.13**	**-0.04 ± 0.06**	-0.35 ± 0.11	0.74 ± 0.13	0.42 ± 0.08	-0.23 ± 0.05
M4	*u*	10.14 ± 1.65	4.43 ± 1.39	7.82 ± 1.02	**-0.65 ± 1.50**	6.57 ± 1.06	2.88 ± 1.15
	v	**0.20 ± 0.19**	**0.12 ± 0.14**	**0.18 ± 0.26**	**0.18 ± 0.23**	**0.15 ± 0.10**	**0.21 ± 0.15**
	w	**0.05 ± 0.13**	**-0.04 ± 0.06**	0.48 ± 0.14	**-0.11 ± 0.09**	0.41 ± 0.08	-0.22 ± 0.05

Figure 4-7: Plot of forward and reverse regression slopes for mobile-bed simulations of (a) u; (b) v; and (c) w. Dotted line indicates a slope of unity. Error bars indicate standard error of regression slopes.

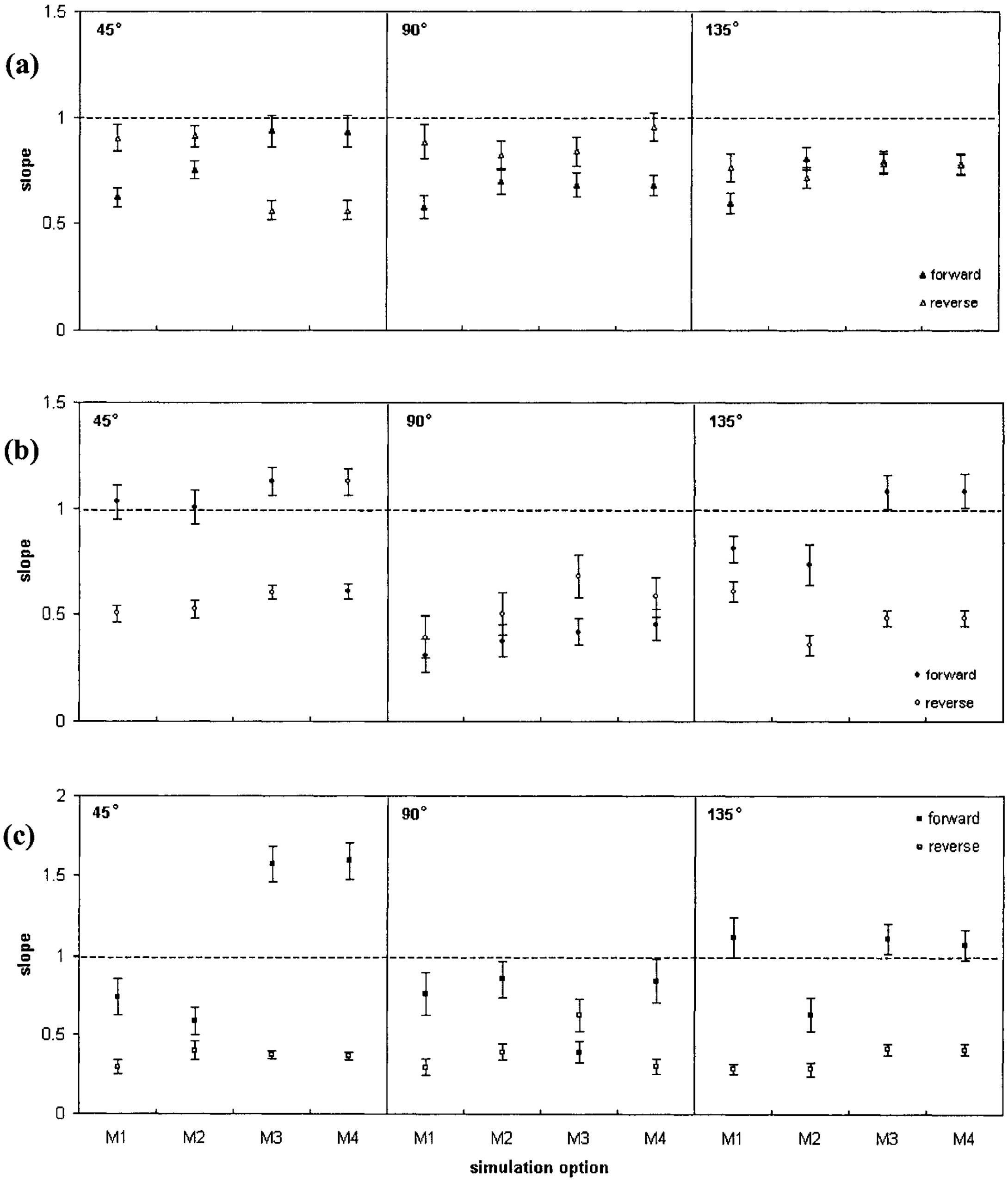

Again, the strong bias appears to be due to the model's tendency to overpredict measured downstream velocities of less than 15 cm/s. As shown in Figure 4-8, this trend is even more pronounced for the mobile-bed simulations than for the stable-bed runs. Like Figure 4.6, the results of all simulation options are plotted together with a LOWESS smoother of tension 0.500.

It is somewhat surprising that, for most variables, the 45° and 135° simulations outperformed the 90° runs. It is possible that the variation in success – given that the only change between runs is the angle of the deflectors – is an artifact of the velocity sampling locations used in the laboratory. For the 90° runs, 18 of 61 velocity measurements near the bed were collected in the scoured zone, compared to 6 out of 70 for the 45° runs and 9 out of 79 for the 135° runs. Because flow patterns within a scour hole are much more complicated than those over non-deformed regions, complicated by separation and vortex production (Dey *et al.*, 1995), it may be possible to conclude that the flow simulations around the 90° deflectors may not have been less 'successful' than the 45° or 135° cases, but rather that the model showed limitations in accurately predicting flow within the scour hole.

4.3 DISCUSSION

4.3.1 Determination of the 'Optimum' Modeling Mesh

The results of the mesh sensitivity analysis (Section 4.1) highlight the necessity to perform such a test, revealing a relatively strong dependence of certain flow variables to grid-cell resolution. While it is entirely possible that different results may have been attained had different modeling treatments been applied to the analysis (i.e. using Option 1 instead of Option 3), the additional time constraints required to so would have been beyond the scope and objectives of this particular research.

In general, dynamic pressure and downstream velocity appear to be the least sensitive components to grid resolutions in both the stable- and mobile-bed cases. The insensitivity of predicted downstream velocity is supported by Nicholas (2001), who states that it may be inappropriate to evaluate the quality of model predictions by downstream velocity alone, assuming, of course, that more flow parameters than simply downstream velocity are of interest to the user (Bates *et al.*, in press).

Figure 4-8: Predicted vs. measured downstream velocity component (*u*), including data from all mobile-bed options for each angle. Dotted line indicates line of equality. Graphs on right-hand side show only measured values less than 15cm/s. Solid line represents LOWESS smoother.

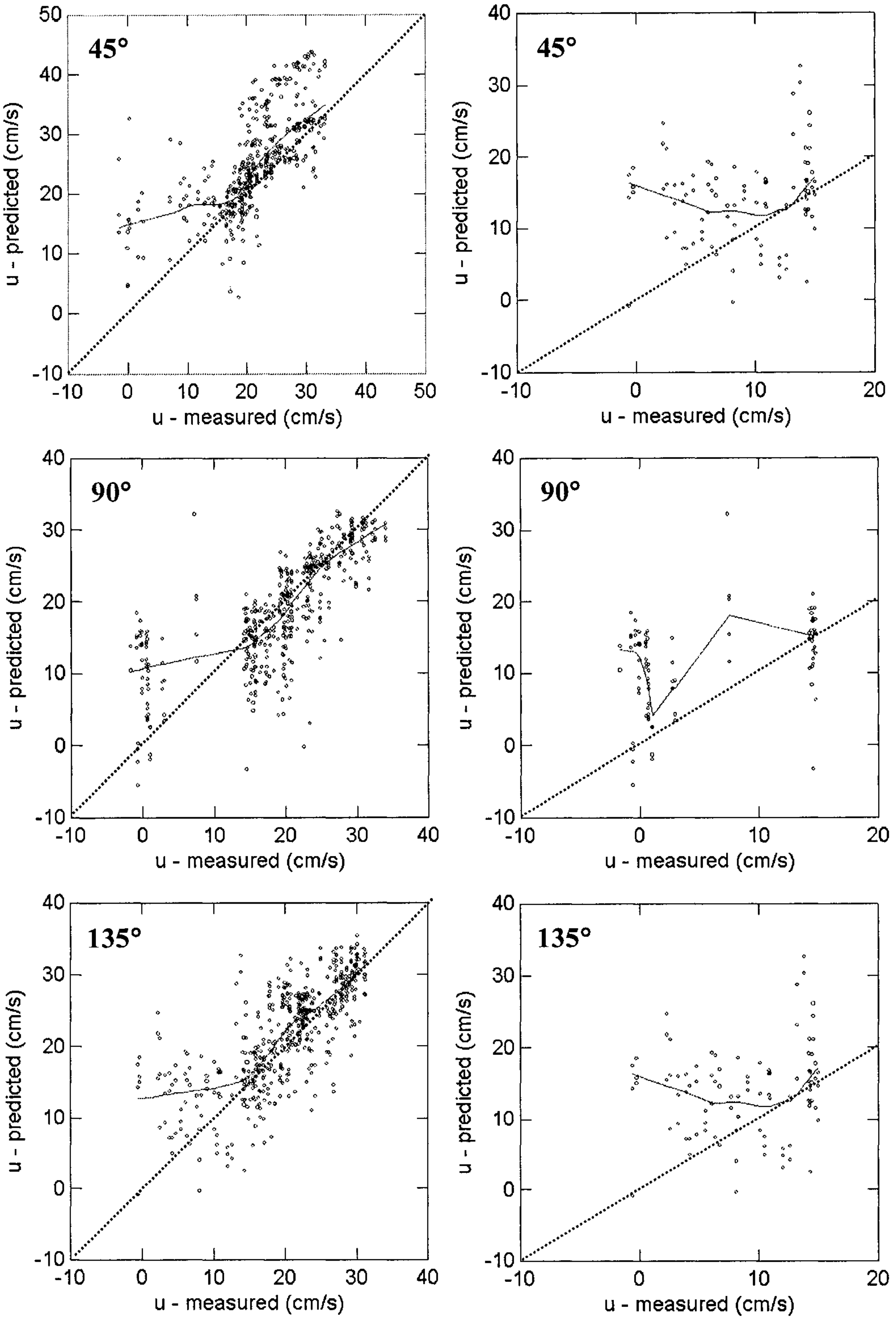

Bradbrook (2000) reported a relatively high sensitivity of vertical velocity, as was evident in Figures 4-1 and 4-3 from the present study. However, the sensitivity of w is somewhat unsurprising, given the relatively low range of predictions that the model is producing. For example, in the present study the maximum vertical velocity magnitude is approximately 10cm/s. Therefore, even a 20% difference in predictions translates into an absolute value of 2cm/s. Given the magnitude of velocity vectors in general, such a change would not greatly impact the general flow field.

The apparent sensitivity of kinetic energy is also common throughout the literature. Other studies (e.g. Bradbrook, 2000; Nicholas, 2001) have reported a strong grid dependence on turbulence parameters, so we may have to accept the notion that a completely grid independent solution for kinetic energy may not be possible (Nicholas, 2001).

Although the ASME recommendations explicitly state the necessity of performing grid sensitivity analyses, the number of meshes that should be tested is still unclear. One suggestion was made by Hardy *et al.* (1999), who recommended that at least four meshes of different resolution should be built. Our results would seem to indicate that had only three to four meshes been tested, it is likely that one of the 'better' meshes would have been excluded, thereby altering the general results of the subsequent simulations. Granted, even having tested ten grids may have excluded a mesh resolution that would have performed even better, but the possibility of having done so is greatly reduced. We therefore recommend that between five and ten grids be used in a sensitivity analysis, a slight increase to the statement of Hardy *et al.* (1999).

In addition, the output of a sensitivity analysis may have to be interpreted in different fashions depending on the individual modeling application. The RMA results indicated that simply using the ±10% thresholds (Bradbrook, 2000) may not have been adequate to determine the optimum grid resolution. For example, Figure 4-1 indicates that there was less difference in the maximum and minimum flow variables between runs SS4 and SS10, but the RMA revealed that, statistically, a higher correlation was found between runs SS6 and SS10 in the zones of interest.

Therefore, for modeling flow around instream obstructions, the analysis of maximum and minimum values may not be sufficient. This is especially true in our case, as the maximum velocity and minimum pressure were often found in the cells that had been partially obstructed by the deflectors. When the grid cell resolution was altered, the proportion of the cell obstruction also changed. Therefore, the maximum values, alone, may not have been fully representative of the overall flow structure. As a result, it may be a useful practice – in the cases where the location of desired output is known *a priori* – to examine the flow variables at measurement locations and compare them to corresponding values from the finest mesh.

4.3.2 Assessing Model Performance

In general, r^2 values between predicted and measured flow properties tended to decrease for u, v, and w, respectively. Such a trend should be unsurprising, as decreasing ranges of target prediction values have been shown to have an impact on correlation values (Sinha and Marelius, 2000). For example, measured u values in our study ranged from approximately -5cm/s to 45cm/s, v ranged from -20cm/s to 20cm/s, and w ranged from –5cm/s to 5cm/s.

The disparity between the stable- and mobile-bed simulations' ability to predict kinetic energy is noteworthy. Because steady-state conditions were imposed on the simulations, the model predictions of kinetic energy do not truly represent velocity fluctuations over time (Lane *et al.*, 2002). Moreover, Robson (2003) showed a marked increase in turbulence production over a sand bed compared to the plexiglas bed, especially in the center of the channel and near the deflectors. Therefore, it is possible that the relatively high r^2 values between predicted and measured kinetic energy over the flat, rigid bed were artificially improved by virtue of the measurement locations, which were for the most part in regions of low *ke*.

Underprediction of recirculation zone width is also a common issue, especially when simulating steady-state flow. Fang *et al.* (1997) showed that in time-dependent flows around obstructions, multiple vortices form, detach, and migrate downstream due to the instability of the shear layer, while steady-state flow produces only one principal vortex bounded by the flow separation line. Recirculation zone underestimation was also reported by Ferguson *et al.* (2003), illustrating the difficulty in accurately simulating time-dependent flow structures within flow fields containing strong reverse flow and lateral shearing.

Although the model's y_w^+ violation in the shearing and recirculation zone may have suggested that the near-bed cell should have increased in height, examining Equation 3-5b reveals that it may instead have been due to abnormally low predicted shear stresses in this area. Because the Log-law wall function calculates shear stress as a function of near-bed velocity magnitude (Equation 3-6a), the low streamwise velocities within the recirculation zone translate into extremely low shear stress predictions. Therefore, it is possible that a different wall function is required to simulate flow fields containing regions of non-logarithmic flow, though any attempt to investigate this is currently beyond the scope of the present study.

Another interesting finding was that the activation of the surface porosity algorithm had no appreciable effect on the stable-bed simulations but did affect the mobile-bed predictions. The effects of porosity – also referred to as the 'free-surface approximation' – on flow predictions has varied throughout the literature. For example, Bradbrook (2000) reported very little difference in predicted vs. measured correlations when porosity was incorporated into a simulation of flow in a parallel confluence. Additionally, Ouillon and Dartus (1997) showed that there was no difference in model predictions near the obstructions between the rigid-lid and free-surface assumptions, though some difference was found near the zone of flow reattachment well downstream.

Certain authors have shown an improvement of model predictions by incorporating a free surface. For example, correlation (*r*) values for Han (2002) improved from 0.68 to 0.83 for the downstream velocity component, and from 0.11 to 0.30 for vertical velocity. In addition, Bradbrook (2000) simulated flows in an angled confluence, and had improvements in downstream and vertical velocity correlation values from 0.66 to 0.88 and 0.07 to 0.10, respectively.

In summary, it is recommended that porosity be activated whenever possible. Because it is impossible to know *a priori* whether or not it will have an appreciable effect – though when it does it has shown to be advantageous, as no examples could be found in the literature stating the contrary – it is unlikely that its incorporation into a modeling scheme will produce adverse results.

4.3.3 Comparison of Results with other Flow Models

In an extensive review and commentary on the ASME recommendations, Bates *et al.* (2005) highlight the necessity of rigorous statistical comparison of predicted and measured flow variables. The authors state that the traditional methods of model evaluation, such as predicted vs. measured flow profiles (e.g. Meselhe and Sotiropolous, 2000; Sinha and Marelius, 2000) or contours (e.g. Ouillon and Dartus, 1997; Richardson and Panchang, 1998), are no longer sufficient. If numerical modeling is ever to be more accepted by the academic community as a legitimate research tool, users need to be more honest and critical of a simulation's performance in an effort to stimulate and promote the advancement of model application.

Qualitative analysis seems to be especially prevalent in published simulations examining flow around instream obstructions, revealed by a brief survey of recent literature on the subject. As illustrated in Table 4-11, the most common techniques used to evaluate a model's performance are visual comparisons of predicted and measured velocity magnitudes, often in the form of plotted vertical profiles or isolines. Because no quantitative analysis was performed in these cases, it is virtually impossible to determine how well the results presented in the current study compare to previously published reports.

As no examples could be found that report a quantitative analysis of simulated flow around obstructions, our model's results must be compared against published studies that performed similar analyses for flow in unobstructed channels (Table 4-12). In terms of accurately predicting velocity components, our results were marginally less successful than Lane *et al.* (2004). However, direct comparison with their study may be partially misleading. Although both experiments were conducted in a laboratory flume, the flow field over a relatively flat, gravelly surface does not exhibit any significant lateral shearing or recirculation zones, and as such all flow is directed downstream. In similar regions in our channel, the model results were far more comparable.

Table 4-11: Previous applications of CFD to flow around instream obstructions in which qualitative comparison of predicted and measured flow properties were used as model evaluation assessment. Unless otherwise indicated, all simulations were performed in three-dimensions.

Source	Study Description	Flow Properties used in Model Evaluation
Ouillon and Dartus (1997)	flow around a groyne	water depth and velocity magnitude isolines
Biglari and Sturm (1998)	two-dimensional flow around bridge abutments in a compound channel	velocity at various points along a single cross-section
Richardson and Panchang (1998)	flow around bridge piers	velocity magnitude isolines
Molinas and Hafez (2000)	two-dimensional flow around bridge abutments	velocity 'turning angle' and nose-velocity amplification
Sinha and Marelius (2000)	flow past submerged vanes	velocity components at various cross-sections and verticals
Yen *et al.* (2001)	flow around bridge piers	velocity magnitude isolines
Ali and Karim (2002)	flow around bridge piers	longitudinal shear stress distribution
Chrisohoides *et al.* (2003)	unsteady flow around bridge abutments	recirculation zone length and visualization of vortices
Salahedin *et al.* (2004)	flow around circular piers	velocity component profiles

Perhaps a more appropriate comparison of our study is with Bradbrook *et al.* (2001a), who simulated flow over a smooth-bed 30° tributary junction with a step, because shearing zones are known to exist at tributary junctions. It can be seen that both our stable- and mobile-bed cases were more successful in predicting downstream velocity and similarly able to predict vertical velocity.

Shearing and recirculation also occur in the flow field near meander bends. Ferguson *et al.*'s (2003) simulations of flow at a meander performed slightly better than ours in terms of downstream and lateral velocity predictions and comparably for vertical velocity and kinetic energy, the latter obviously referring only to our stable-bed simulations.

What is also significant to note is that very few studies have simulated flow over regions of rapidly changing topography, as was found near the deflectors, and thus comparison of our mobile-bed simulations to other published studies is limited.

Table 4-12: Previous studies in which quantitative analysis of flow model predictions was undertaken to compare simulated and measured results. The values shown are predicted vs. measured coefficient of determination (r^2).

Source	Study Description	Downstream Velocity	Vertical Velocity
Bradbrook *et al.* (1998)	tributary junction with parallel tributaries (lab)	0.91	0.51
Lane *et al.* (1999)	flow in a confluence	0.50	0.59
Bradbrook *et al.* (2001)	tributary junction angled at 30° to post-junction channel (lab)	0.53	0.59
Booker *et al.* (2001)	flow in a natural riffle-pool sequence	0.51	-
Ferguson *et al.* (2003)	flow at a meander bend with recirculation at inner bank (field)	0.90	0.44
Lane *et al.* (2004)	experimental study of a channel with a rough bed (lab)	0.91	0.51

For example (Hodskinson and Ferguson, 1998) examined flow in a meander bend but did not collect velocity measurements in the pool, and therefore all model comparisons are made simply with the relatively simple flow conditions over more shallow regions. One study that did report difficulty in predicting flow velocity in regions of rapidly changing topography was Booker *et al.* (2001). Figure 4-9 shows a reproduction of their predicted vs. measured velocity data, illustrating – as we did in Figure 4-8 – a strong overprediction of low flow velocities.

Such comparison serves to highlight that direct comparison of correlation values between any two studies does little more than illustrate the relative successes of individual modeling applications. Because various field and laboratory studies necessarily record measurements at different locations, it is possible that over-sampling in relatively simple flow regions or under-sampling in complex regions could artificially increase predicted vs. measured correlation values. If model predictions from areas without serious complications are being compared to measurements in the same regions, it would be unsurprising that the correlation values would be higher. This was particularly evident for our mobile-bed 90° runs, where over-representation of measurements within the scour hole may have led to reduced correlation values.

Figure 4-9: Scatterplot of model predictions against flow measurements from: (a) Booker *et al.* (2001), and (b) current study (Figure 4-8). Circled points show model overpredictions in regions of rapid topographic change.

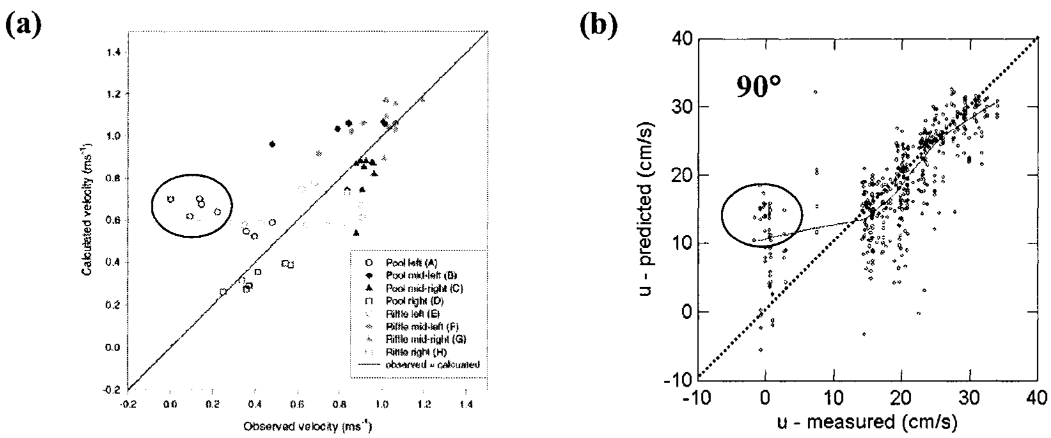

As a result, we recommend an addition to the ASME guidelines reviewed by Bates *et al.* (2005): that researchers should include a figure and short discussion highlighting their measurement locations in addition to the statistical assessment of the model's predictions. It should then be stated explicitly that the reported correlation values reflect the relationship between the model results and the measurements at those given locations only. Although such a statement would not necessarily make any two studies more directly comparable, it would allow the reader or reviewer to more objectively assess the value of the regression results. In a sense, then, a study that has many more measurements within a recirculation zone and a predicted vs. measured r^2 of 0.60 may be deemed "as successful" as another with r^2 values of 0.90 where virtually all of the measurements came from relatively straightforward flow regions.

In addition, it is also recommended that more uniform guidelines be developed to assess the credibility of a given model evaluation. For example, the fundamental scale differences between laboratory and field studies should necessitate the use of different flow measurement devices and techniques. Because a modeling mesh of a natural river reach would have much larger cells than one for a laboratory flume, the sampling volume of an ADV would be much too small to effectively compare to the river model's predictions. It is possible, then, that methods such as Particle Image Velocimetry (PIV) should be further investigated for field applications, as the imaging of large scale processes at a given instant in time may be more applicable for comparison to a numerical model of similar scale than ADV or ADCP recordings.

4.3.4 "Object-Bed" vs. Bed Porosity

Although the simulations using the object-bed (M3 and M4) were seemingly less successful than the bed porosity notion of Lane *et al.* (2002, 2004), they did exhibit potential. Both techniques are conceptually similar, with the object-bed presenting a new option to incorporating complex bed geometry into a numerical model while entirely eliminating potential cell-skew difficulties.

As outlined in the previous section, direct comparison of the relative success rates of the present study and Lane *et al.* (2004) may not be relevant due to the fundamental differences in the complexity of the respective flow fields. Had the object bed been created based on the gravel-surface DEM, it is likely that a much better correlation would have been achieved than was found for the more intricate flow field around the deflectors.

The object-bed, if ever successfully refined, would provide a number of advantages over bed porosity. Firstly, because the software used to create it (AC3D) is extremely user-friendly, no intensive computer programming is required. As a result, the use of numerical models could become more widespread by so-called 'non-experts', thereby addressing the concern of Gilvear (1999), who stated that one of the fundamental challenges of stream restoration design is incorporating the increased use of hydraulic modeling by geomorphologists.

Additionally, the object-bed considers the entire bed to be a single solid object, while bed porosity numerically obstructs portions of individual cells based on predetermined values corresponding to bed elevations at given locations. Therefore, the advantage of using an object bed is that no modifications would need to be made regardless of modeling mesh resolution (Figure 4-10a), whereas the porosity algorithm would need to be altered once the grid structure is changed (Figure 4-10b).

Figure 4-10: Independence of object bed to modeling mesh resolution (modified from Lane *et al.*, 2002).

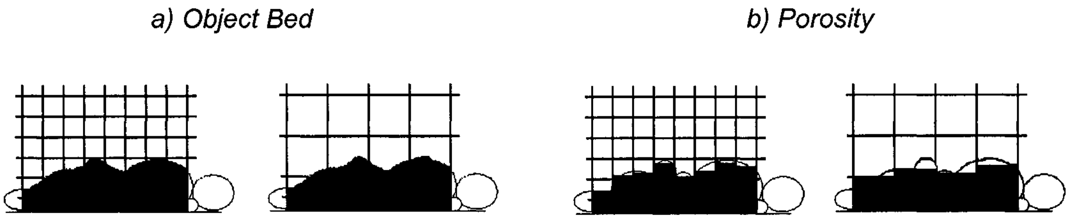

The grid independence of the object bed eases the transferability of a given object-bed between grids, and would especially make any mesh sensitivity analysis more straightforward as a single bed could be used in all grids in the analysis.

However, bed porosity would seem to be applicable to a wider variety of channels. Because it can be developed within a BFC coordinate system, the planform geometry of a curved channel could be defined with the appropriate bed elevations subsequently being accounted for by porosity. As the object-bed was designed specifically with straight channels in mind, at present complex planform geometry cannot be incorporated. Although, theoretically, it could be accomplished by extending the size of the 'object' to include the banks and floodplain as obstructions, it would undoubtedly necessitate a dramatic increase in the total number of grid cells within the modeling domain. As a result, the time-to-solution would be greatly increased (Hardy *et al.*, 1999), potentially to the point of unfeasibility.

Moreover, porosity could be treated as a dynamic simulation variable if sediment transport functions were to be coupled with the flow model (Lane *et al.*, 2002). Because porosity is a numerical property of the mesh, time-dependent models that predict scour and/or deposition could automatically update the porosity value at a given location to accordingly decrease or increase the virtual bed elevation. As object beds are created externally and then imported into an 'empty' mesh, instant updates are impossible and thus individual beds would need to be constructed at each stage of topographic change.

For future applications, it is recommended that a higher-resolution DEM is used to create the object-bed. Because our study was restricted to using topography measurements at a resolution of approximately one per $3cm^2$, the object still retained visual characteristics of the TIN process used to create it. Theoretically, an increased number of nodes would make the bed surface smoother, which in turn would likely translate into improved model performance. Even if the high-resolution photogrammetrical methods (e.g. Lane *et al.*, 2002, 2004) are not available to the user, a minimum resolution of $1point/cm^2$ – easily attainable with a manual point gauge in a laboratory setting – would likely be sufficient.

5. EFFECT OF DEFLECTOR GEOMETRY ON FLOW FIELD

5.0 PREFACE

The evaluation presented in Chapter 4 illustrated that the model is sufficiently capable of reproducing the three-dimensional flow field around deflectors in a laboratory flume, thereby satisfying the first objective of the thesis. As noted by Lane *et al.* (1999), a successfully evaluated model can then be used to test numerous combinations of boundary conditions far more efficiently than can be done in the laboratory. Therefore, numerical simulation will now be used to address the second of the thesis' objectives: to investigate the influence of deflector geometry on the resulting three-dimensional flow field.

To examine the impact of deflector angle on the flow field, simulations were performed using deflectors with a contraction ratio (*CR*) of 0.25 aligned at angles ranging from 30° to 150° at 15° intervals. Additionally, the effect of deflector length on the resulting flow field was examined for angles of 45°, 90°, and 135° by varying the contraction ratio from 0.10 to 0.35 at increments of 0.05. Attempts to use deflectors smaller than 0.02m in length (*CR* = 0.10) were unsuccessful because they were not large enough to effectively block any grid cells in the 45° and 135° cases without PARSOL being activated (see Section 3.2.3). Deflectors larger than 0.07m (*CR* = 0.35) resulted in numerical instability in solution, and thus the simulations did not converge.

Based on the flat-bed mesh sensitivity analysis (Section 4.1), grid dimensions for all runs were set at 165*40*10 in the x-, y-, and z-directions, respectively. Additionally, it was decided that all simulations would be run using the conditions outlined for Option S2 (see Section 4.2.1), as it was shown to successfully match the laboratory measurements. Although Option S3 also performed adequately, the ease of altering minute details of deflector construction using a Cartesian mesh outweighed the minor improvement in performance provided by Option S3. A summary of simulation properties is presented in Table 5-1.

Table 5-1: Simulation variables used to examine the effect of deflector orientation and length on the resulting three-dimensional flow field.

Variable	Description
Coordinate System	Cartesian
Mesh Dimensions	165*40*10
Deflector Insertion	Pixelated
Water Surface Topography?	No
Water Surface	Rigid Lid
Flow Depth	0.095 m
Average Inlet Velocity	0.25 m/s
Inlet Turbulence Intensity	10%
Bed Roughness	$d_{50} = 0.0011$ m
Turbulence Model	RNG-kε
Wall Function	Log-Law

It should be noted that the primary difference between the simulations run for the current set of experiments and those used for the model evaluation is exhibited in the boundary roughness. For the stable-bed runs in Chapter 4, roughness was set to 0.000m as the base of the flume was a smooth Plexiglas bed. Because the simulations in the following chapter are being used to represent the flow field over a sand bed prior to deformation, the boundary roughness was changed to 0.0011m – the median diameter of the bed particles used in the laboratory mobile-bed runs. Lane *et al.* (2002) have illustrated a relative insensitivity of model predictions to minor changes in boundary roughness definition, hence there should be no significant impact on the reliability of the model's output.

The general properties of flow around instream obstructions – especially bridge piers and abutments – has been widely documented (e.g. Lim, 1997; Melville, 1997; Lim and Cheng, 1998; Molinas *et al.*, 1998; Kothyari and Ranga Raju, 2001). As described in Section 2.2.1, flow deceleration causes an adverse pressure gradient to form along the upstream face of the obstruction, thereby directing flow towards the bed. A build-up of pressure upstream of the obstruction forces flow toward the center of the channel, with the maximum velocity amplification being found at the obstruction nose. The sudden pressure drop at the nose forces flow to separate around the barrier, reattaching to the bank well downstream. Meanwhile, flow in the center of the channel is accelerated in order to maintain continuity, as flow in the recirculation zone does not contribute to downstream mass and momentum transfer (Ahmed and Rajaratnam, 1998).

Various authors (e.g. Melville, 1997; Sinha and Marelius, 2000) have shown that flow field properties are dependent on both the length and orientation of the obstructions, while others have shown that equilibrium scour hole depth and geometry also vary based on obstruction geometry (e.g. Ettema *et al.*, 1998; Kuhnle *et al.*, 2002). Because scour is ultimately a function of changes to the flow field imposed by the obstruction, we hypothesize that performing a systematic analysis on the changes to the pre-deformation flow field due to structure geometry will yield insight into why the scour hole is also dependent on structure design. Therefore, it is not the goal of this chapter to perform a sophisticated analysis on the underlying physics dictating the structure of the flow field around deflectors. Rather, we hope to establish trends for various bulk flow field properties based on deflector angle and length that can later be related to equilibrium scour hole geometry (Chapter 6).

The following chapter begins with a general description of flow around instream obstructions, including the distributions of dynamic pressure, velocity magnitudes, and negative vertical velocity (downwelling). This is followed by a presentation of the simulation results using deflectors of varying angle and length. Finally, a comparison of our findings with other published reports is conducted.

5.1 GENERAL DESCRIPTION OF THE FLOW FIELD AROUND DEFLECTORS

For illustrative purposes, examples of the near-bed flow properties used in the subsequent analyses are shown in Figure 5-1, having been taken from the simulations around 90° deflectors of contraction ratio 0.25. The properties described in the following paragraphs are consistent throughout all runs, and thus can be considered representative of the general flow field around deflectors.

The dynamic pressure distribution – defined as the total pressure minus that due to hydrostatic effects (Bradbrook *et al.*, 2000) – is shown in Figure 5-1a. Although the distribution is shown for the bed only, dynamic pressures calculated in numerical simulations with the rigid-lid assumption are virtually uniform at each

Figure 5-1: Definition sketches of (a) simulated dynamic pressure field; (b) simulated velocity field, and; (c) simulated downwelling distribution around deflectors. Examples shown are for 90° deflectors of contraction ratio 0.25. Contour lines for the local suction pressure pocket are at intervals of approximately 0.2Pa.

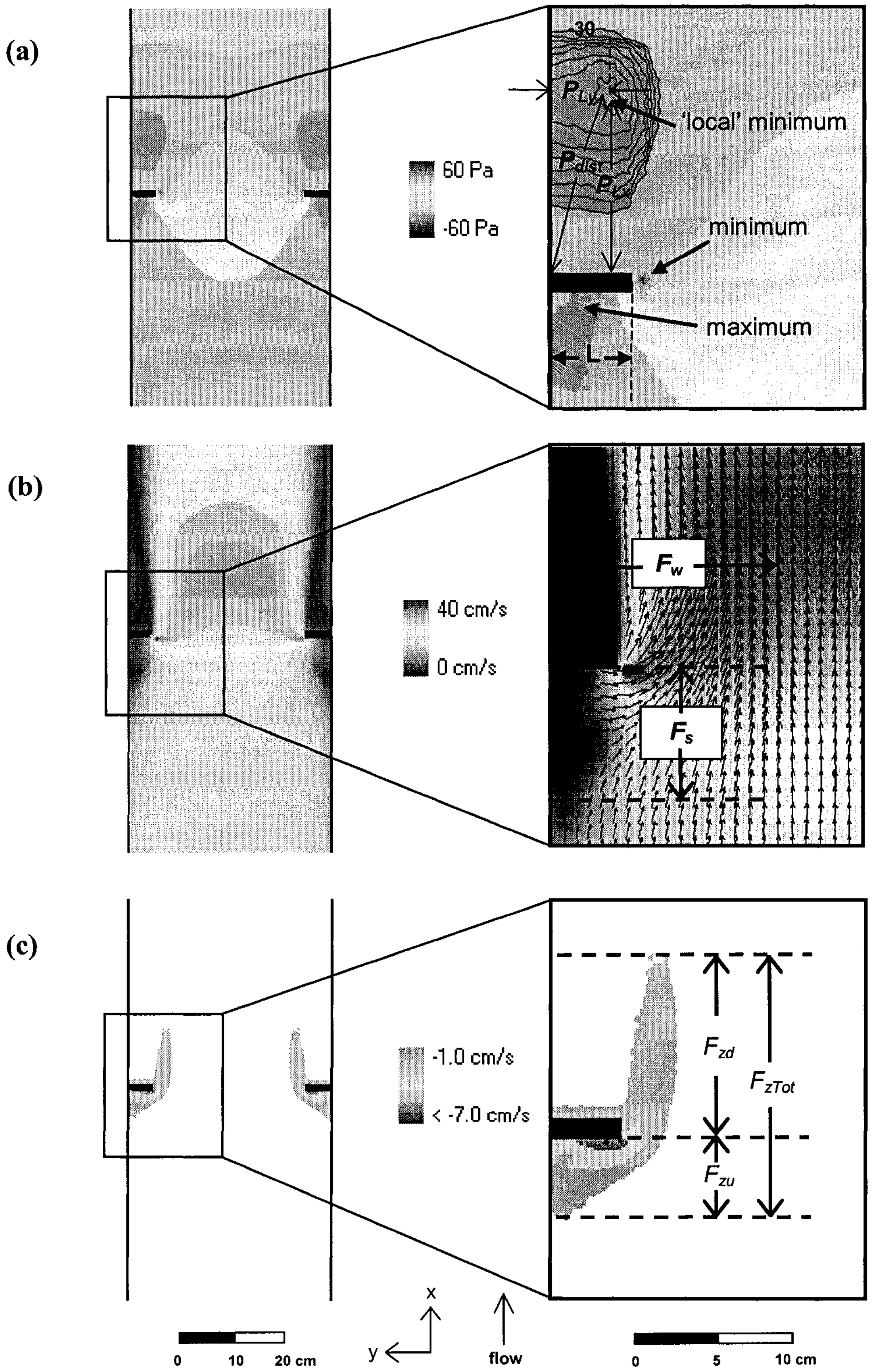

vertical profile (Ouillon and Dartus, 1997), and thus effectively represent the pressure field throughout the flow column.

A pressure increase occurs immediately upstream of the deflectors, with the maximum value found at the deflector face. Beginning at the cross-section between the deflector noses, negative 'suction' pressure takes precedence, with the minimum value located at the nose. Additionally, a pocket of amplified (increasingly negative) suction pressure exists behind the deflectors. Within this pocket, a 'local' minimum is found at a distance P_{Lx} downstream and P_{Ly} laterally from the deflector-bank junction, exhibiting magnitudes slightly less than those found at the nose.

Figure 5-1b shows velocity magnitudes and vectors in the vicinity of the deflectors. As expected, deceleration occurs upstream of the deflectors, and a region of acceleration is found in the center of the channel. The maximum velocity amplification occurs at the leading edge of the deflector nose. Upstream of the obstruction at a distance F_s, flow separates from the bank and is forced strongly towards the center of the channel. Laterally away from the obstruction, the outward flow gradually becomes aligned with the x-axis, eventually becoming parallel to the approach flow at a distance F_w. The region dominated by negative vertical velocity (downflow) is shown in Figure 5-1c. Significant downwelling is found adjacent to the deflector, beginning at a distance F_{zu} upstream of the deflector-bank junction, and extending directly downstream of the deflector nose to a distance F_{zd}, for a total

Figure 5-2: Vertical distribution of flow vectors near the deflectors 1cm from the bank. Blank areas represent modeling mesh cells blocked out by the deflectors.

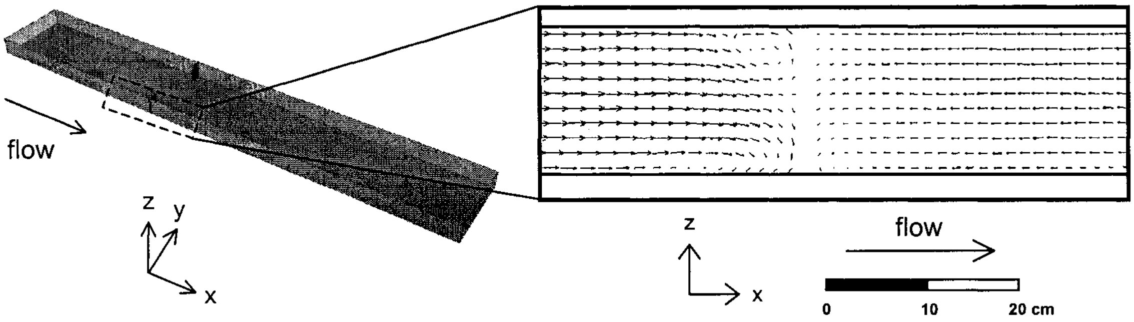

length of F_{zTot}. Figure 5-2 shows the vertical distribution of flow vectors next to the banks. As flow is forced towards the bed, roller vortices with a lateral axis of rotation are found upstream and downstream of the deflectors.

5.2 EFFECT OF DEFLECTOR GEOMETRY ON THREE-DIMENSIONAL FLOW FIELD

5.2.1 Effect of Deflector Angle

Figure 5-3a shows the near-bed dynamic pressure distribution around deflectors of various angles, with the magnitudes of the maximum, minimum (nose), and 'local' minimum (behind the deflectors) presented in Figure 5-4a. The area affected by the upstream pressure buildup grows with increasing deflector angle, while the maximum pressure value increases with angle from 24.8 Pa for the 30° deflectors to 37.2 Pa for the 150° deflectors. Minimum pressures at the nose indicate that, other than for 30°, deflector angle has no significant effect, with values varying by less than 2 Pa in all cases. Local minima, as well, show little variation with deflector angle, with values increasing in magnitude from -27.8 Pa for 30° up to -31.5 Pa for 90°, and subsequently decreasing to -29.3 Pa at 135°. Although the magnitude of the local minima is greatest for the 90° deflectors, their locations consistently migrate closer to the deflector-bank junction (i.e. P_{dist} decreases) with increasing deflector angle (Table 5-2).

Table 5-2: Magnitude and location of local minimum dynamic pressures as a function of deflector angle.

Angle	Local Min (Pa)	P_{Lx} (cm)	P_{Ly} (cm)	*Pdist* (cm)
30°	-27.75	20.8	4.3	21.2
45°	-30.10	16.0	4.1	16.5
60°	-30.19	15.1	4.6	15.8
75°	-30.42	14.7	4.3	15.3
90°	-31.46	13.0	3.9	13.6
105°	-27.49	12.6	3.4	13.1
120°	-30.44	10.3	4.2	11.1
135°	-30.47	8.9	3.1	9.4
150°	-29.27	6.0	2.4	6.5

Figure 5-3: Effect of deflector angle on near bed distributions of: (a) dynamic pressure; (b) velocity magnitude, and; (c) negative vertical velocity.

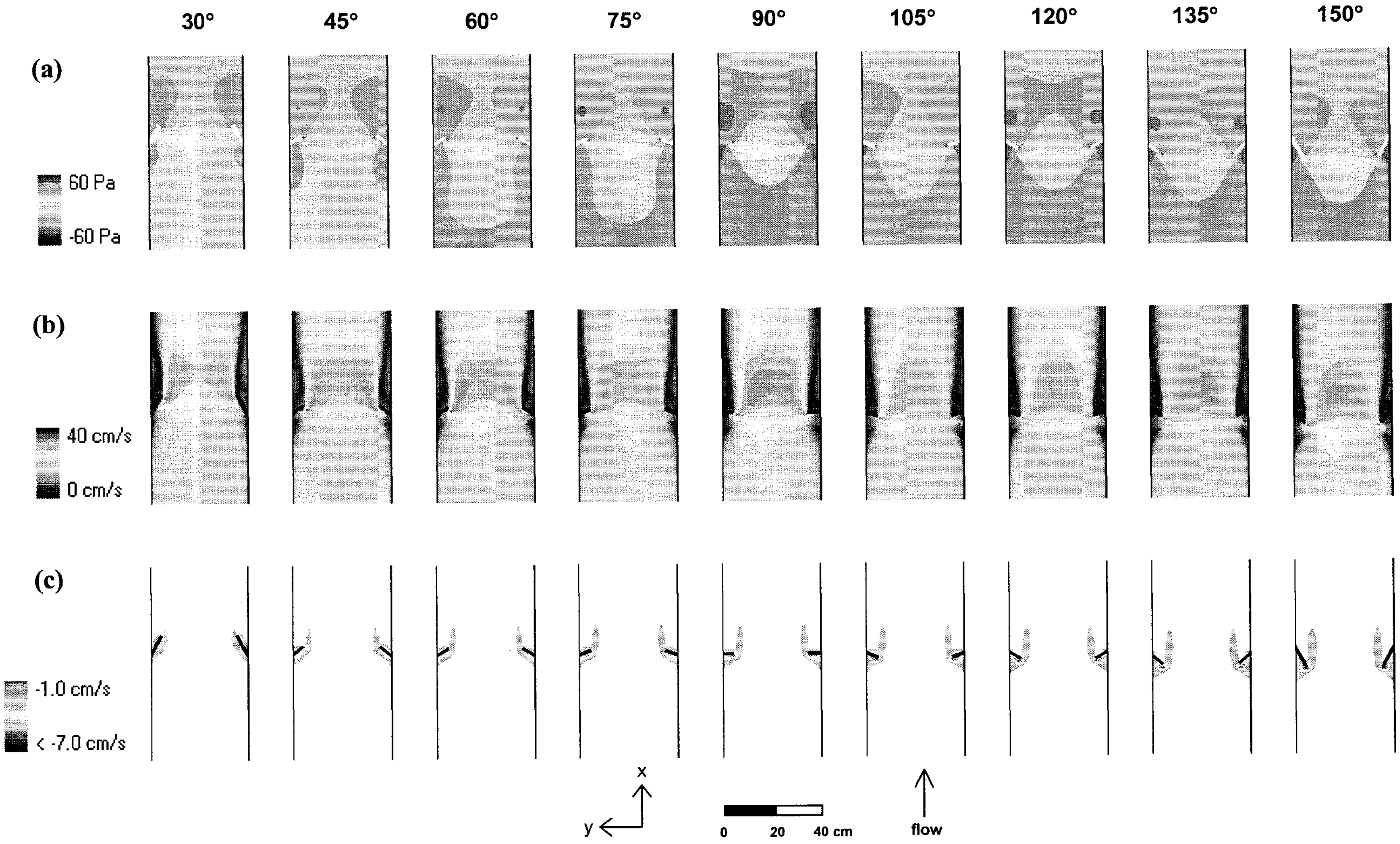

Figure 5-4: Effect of deflector angle on: (a) magnitudes of maximum, minimum, and local minimum dynamic pressure (Pa); (b) nose velocity amplification.

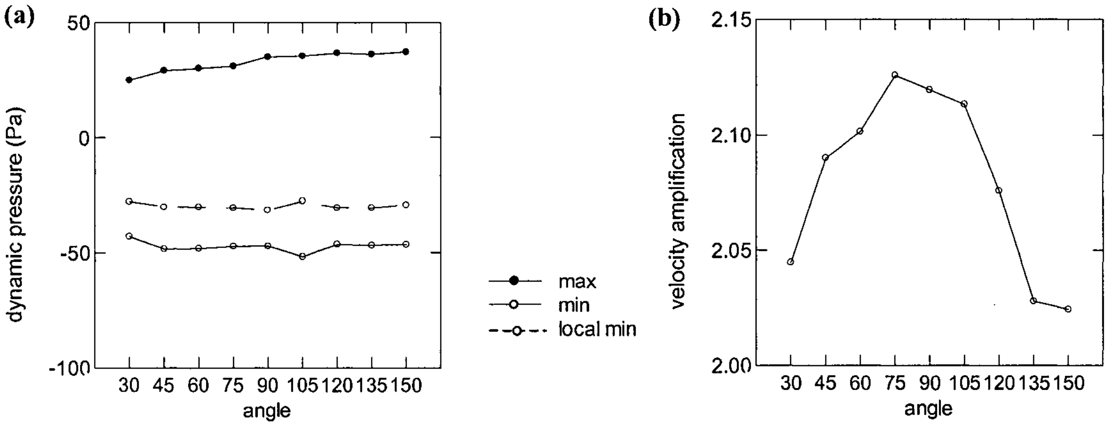

Near-bed velocity magnitudes are shown in Figure 5-3b. For the downstream-facing deflectors, lobes of high-speed fluid extend from the deflector nose downstream towards the center of the channel. At angles greater than 90°, however, these lobes appear to meet in the center of the channel, with the zone of acceleration decreasing in area as deflector angle increases. In all cases, the nose velocity (V_n) is more than double the value of the approach flow (V_a) (Figure 5-4b), increasing from 38.9cm/s for 30° to 40.4cm/s at 75°, then decreasing to 38.5cm/s for 150°, corresponding to a velocity amplification ($\Lambda_n = V_n/V_a$) of 2.04, 2.13, and 2.02, respectively.

The approach flow must overcome the strong pressure gradient set by the obstruction, and thus separates from the bank at a distance F_s upstream of the deflector. Values of F_s vary greatly with deflector angle, as illustrated in Figure 5-5a (shown in dimensionless form normalized by deflector length: F_s/L). Values of F_s range from 2.7cm for 30° to 18.0cm 150° deflectors, corresponding to non-dimensional distances (F_s/L) of 0.54 to 3.60. Figure 5-5a also shows the relationship between flow contraction width (F_w) and deflector angle. Values of F_w increase with angle for downstream-facing deflectors, ranging from 11.5cm for 30° to 14.2cm at 90°, translating into non-dimensional distances (F_w/L) of 2.3 and 2.8. Although a

Figure 5-5: Effect of deflector angle on: (a) upstream flow separation distance (F_s) and width of separation zone (F_w), normalized by deflector length; (b) peak downward vertical velocity magnitude.

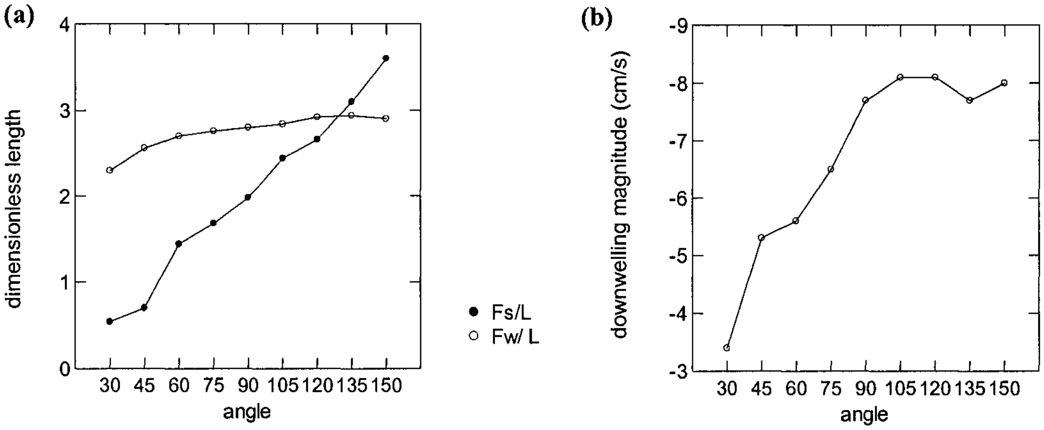

slight increase is shown for deflector angles greater than 90°, the value of F_w for 150° is only 0.5cm greater than that for 90° ($F_w/L = 2.9$).

Vertical velocity distributions near the deflectors are shown in Figure 5-3c. In general, strong downwelling at the bed occurs along the upstream face of the deflectors and extends downstream from the nose. As the deflector angle increases, the flow begins to have a stronger vertical component at distances further upstream (F_{zu}), ranging from 1.7cm for 30° to 12.5cm for 150°, corresponding to dimensionless distances (F_{zu}/L) of 0.34 to 2.50. The maximum downstream extent (F_{zd}) of negative vertical velocities increases with deflector angle from 12.0cm for 30° to 13.3cm for 75°, then decreases to 9.7cm for 150°, or dimensionless distances 2.40, 2.66, and 1.94, respectively. In all cases, the total length of the downwelling zone (F_{zTot}) increases with deflector angle (Table 5-3).

The location where the maximum downwelling occurs is also dependent on deflector angle. As the deflector angle increases, the location of the maximum downflow migrates from the bank along the deflector face, ultimately reaching the nose and remaining there for all upstream-facing deflectors. Furthermore, the magnitude of the maximum increases with angle for the downstream-facing

Table 5-3: Upstream (F_{zu}), downstream (F_{zd}), and total (F_{zTot}) extent of downwelling as a function of deflector angle.

Angle	F_{zu} (cm)	F_{zd} (cm)	F_{zTot} (cm)
30°	1.7	12.0	13.7
45°	2.3	12.9	15.2
60°	3.8	13.0	16.8
75°	4.3	13.3	17.6
90°	4.9	12.2	17.1
105°	7.0	12.1	19.1
120°	8.1	10.4	18.5
135°	10.0	9.0	19.0
150°	12.5	9.7	22.2

deflectors, but becomes nearly constant for deflector angles greater than 105° (Figure 5-5b).

Immediately adjacent to the deflectors, the amount of downwelling that occurs on the lee side decreases as the deflector angle increases. For the 30° runs, downwelling is almost equally distributed on the streamwise and lee sides of the deflectors. However, all downflow occurs on the streamwise side for obstruction angles greater than or equal to 105°. Upon closer examination, this appears to be a function of roller vortex formation near the bed (Figure 5-6). As the flow is forced towards the bed, vortices with a lateral axis of rotation are formed, moving in clockwise and anticlockwise directions for upstream and downstream vortices, respectively. As the deflector angle increases to 90°, the size of the downstream rollers decreases. Vortex formation on the upstream side of the deflectors begins at 75°, where the upstream and downstream vortices are virtually symmetrical. From 90° to 120°, two counterrotating vortices are seen at the bed and the surface upstream of the deflector, with the bed vortex increasing in size with increasing deflector angle. From 135° to 150°, the surface roller disappears entirely and the bed roller increases in size and migrates further upstream, with strong regions of downflow found between it and the deflector.

In summary, many facets of the flow field are affected by the deflector angle of orientation (Table 5-4). In general, a greater perturbation of the flow field is found for higher deflector angles. Specifically, the upstream dynamic pressure maximum,

Figure 5-6: Effect of deflector angle on the vertical distribution of flow vectors near the deflectors 0.5cm from the bank. Blank areas represent modeling mesh cells blocked out by the deflectors.

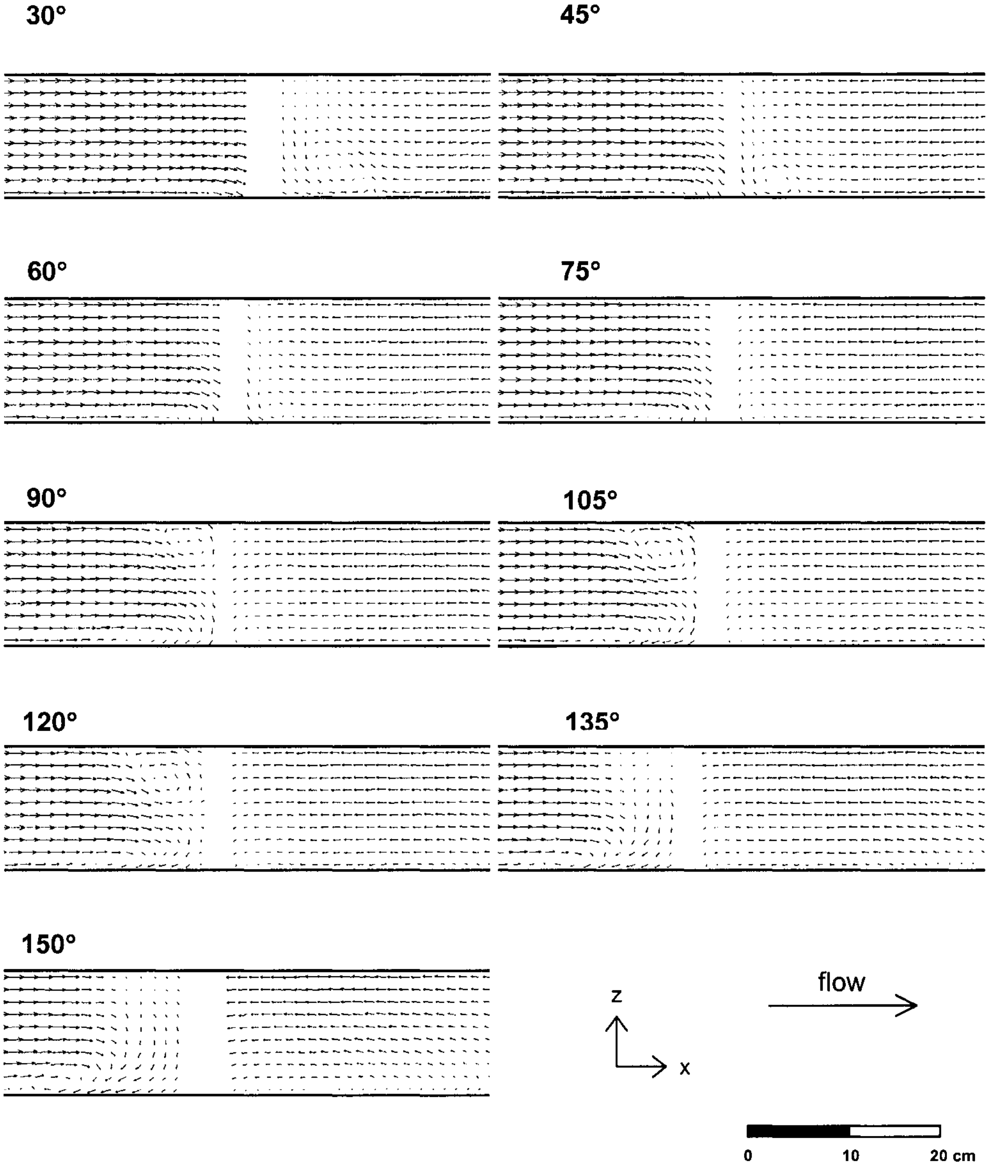

upstream flow separation distance, upstream downwelling extent, and total downwelling distance all increase with greater deflector angles. However, 'local' minimum dynamic pressure, nose velocity amplification, downstream downwelling extent, and flow contraction width are maximized at angles closer to 90°.

Table 5-4: Summary of the effect of deflector angle on various properties of the flow field.

Flow Parameter	Minimum	Maximum	Variation with Angle
upstream dynamic pressure (mag)	30°	150°	increase
downstream dynamic pressure (mag)	30°	45°	no trend
'local' minimum pressure (mag)	30°	90°	increase to 90°, then decrease to 150°
nose velocity amplification (Λ_n)	150°	75°	increase to 75°, then decrease to 150°
upstream flow separation distance (F_s/L)	30°	150°	increase
flow 'contraction width' (F_w/L)	30°	135°	increase to 120°, then plateau at F_w/L=2.9
upstream downwelling distance (F_{zu}/L)	30°	150°	increase
downstream downwelling distance (F_{zd}/L)	135°	75°	increase to 75°, then decrease to 135°
total downwelling distance (F_{ztot}/L)	30°	150°	increase

5.2.2. Effect of Deflector Length

The analysis from the preceding section was repeated for the simulations run with varying deflector lengths. A summary of the findings is presented below with extended detail for interested readers found in Haltigin *et al.* (2004).

In general, increasing the length of the deflectors augments the flow variables described in Section 5.2.1. Specifically, the magnitudes of the maximum, minimum, and local minimum dynamic pressure increase considerably as deflector length is increased. When contraction ratios (*CR*) are less than 0.2, the pressure variables are maximized for the 90° deflectors. However, at $CR > 0.20$ maximum values for both the 90° and 135° deflectors are virtually equal – in all cases being greater than values for the 45° obstructions. For all angles, greater contraction ratios lead to a progressive downstream migration of the local minimum.

Deflector length also impacts the velocity field. Recirculation zones behind the deflectors increase in length and width, which results in a narrower but faster acceleration zone in the center of the channel. Nose velocity amplifications were found to be strongest for the 90° deflectors, with values of Λ_n ranging from 1.6 to 2.7 for contraction ratios of 0.10 and 0.35. For the 45° and 135° deflectors, Λ_n values were virtually equal, ranging from 1.1 to 2.5. Additionally, longer deflectors force the flow to separate from the upstream bank at greater distances (F_S increases). In all cases, F_S is greatest for the 135° deflectors and lowest for the 45° deflectors.

Dimensionless separation distances (F_s/L) become constant beyond CR of 0.20 at values of 0.7, 1.65, and 2.7 for the 45°, 90°, and 135° deflectors (Figure 5-7a).

The width of the separation zone at the nose (F_w) increases rapidly for all angles. Below contraction ratios of 0.20, F_w is greatest for the 90° deflectors while values for 45° and 135° are equal but considerably lower. When normalized by deflector length, F_w/L exhibits an initial rise in magnitude for the 45° and 135° deflectors, while values for the 90° deflectors decrease consistently. Above CR = 0.20, all three angles exhibit a negative linear trend (Figure 5-7b).

The upstream limit of the downwelling distribution (F_{zu}) is almost constant for all contraction ratios for the 45° deflectors, but increases greatly with deflector length for the 90° and 135° deflectors. The downstream extent (F_{zd}) increases in length for all angles. Beyond contraction ratios of 0.25, however, the dimensionless lengths (F_{zd}/L) for the 45°, 90°, and 135° deflectors achieve constant values of approximately 2.55, 2.40, and 2.0, respectively. Similarly, F_{zTot}/L values for the three angles become constant beyond contraction ratios of 0.30, with values of 3.0, 3.2, and 3.7, respectively. In general, maximum downwelling magnitudes increase for longer deflectors, with the greatest values being exhibited for the 135° deflectors.

Figure 5-7: Effect of deflector length on: (a) dimensionless upstream separation distance (F_s/L); (b) dimensionless width of separation zone (F_w/L) for three different deflector angles.

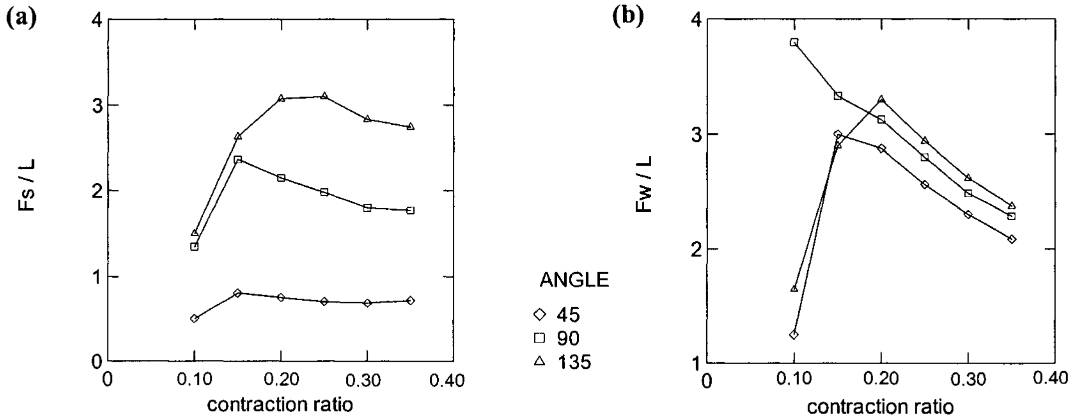

In summary, increasing the length of the obstructions tends to augment the values of several of the flow parameters, including maximum, minimum, and local minimum dynamic pressures, nose velocity amplification, upstream and lateral width of the separation zones, and downwelling extent and magnitude. However, normalizing certain variables by deflector length – namely, upstream flow separation distance, and downstream and total downwelling extent – results in constant values being attained, generally beyond $CR = 0.2$.

5.3 DISCUSSION

5.3.1 Pressure

Although virtually all studies on flow around obstructions mention the importance of pressure gradients on the resulting flow field, very few studies have included discussion of the dynamic pressure field, opting instead to focus on simply velocity and/or shear stress (e.g. Molinas and Hafez, 2000; Salahedin *et al.*, 2004). One of the few examples that examines dynamic pressure at length is Ouillon and Dartus (1997), who simulated flow around a groyne of contraction ratio 0.111.

Figure 5-8a shows these authors' dynamic pressure field at the bed for simulations incorporating a rigid-lid. Similar to our study (Figure 5-3a), a local buildup of pressure occurs in a bubble shape along the upstream face of the obstruction. Moreover, suction pressures extend downstream, with a local minimum occurring on the lee side of the deflectors.

In addition, Figure 5-8a illustrates that Ouillon and Dartus (1997) successfully used the dynamic pressure field as a proxy for water depth, with an increase of slightly less than 10Pa corresponding to water surface superelevation of 1mm. To test this relationship for the present study, water surface topography data taken from Robson (2003) were regressed against the predicted dynamic pressure values at the topography measurement locations taken from the 45°, 90°, and 135° model S2 runs (see Section 4.2.1) (Figure 5-8b). The relationship between the change in water column depth from approach depth ($Y-Y_0$) and dynamic pressure is very good, with

Figure 5-8: Relationship between simulated dynamic pressure and water surface elevation for: (a) Ouillon and Dartus (1997), and; (b) the present study.

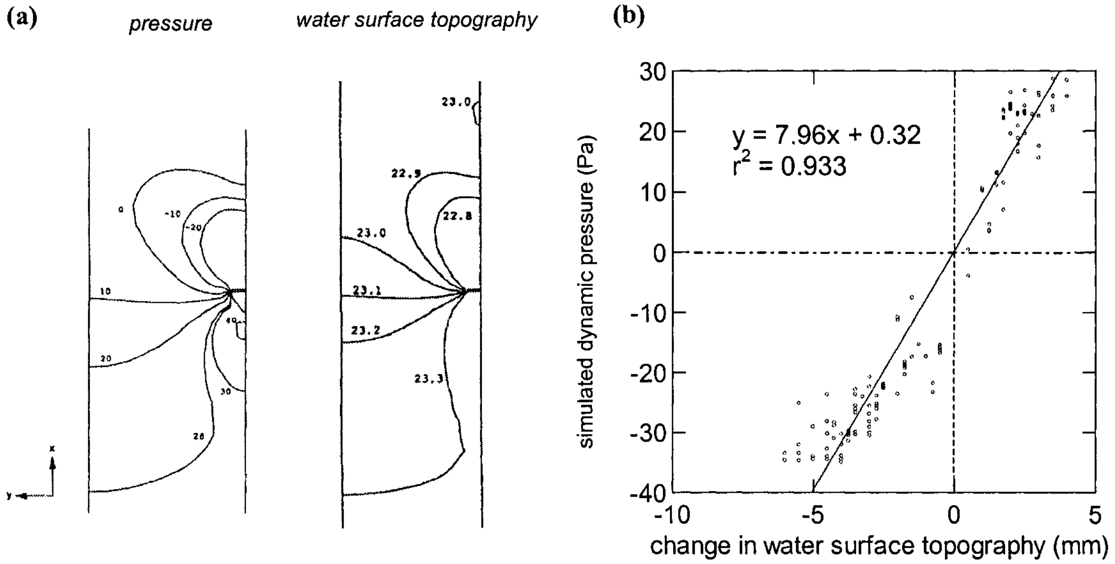

an r^2 of 0.933. The slope of the line of best fit indicates that the water column increases by 1mm for each increase of approximately 8Pa of pressure.

As a result, we can conclude that: (i) the simulations in the present study are qualitatively comparable to Ouillon and Dartus (1997) in terms of reproducing the dynamic pressure field, and; (ii) under rigid-lid assumptions, the dynamic pressure field can be used as a surrogate when water surface topography data are not available. Therefore, based on Figure 5-4a and Haltigin *et al.* (2004), it can be stated that water surface superelevation near deflectors increases with increases in both deflector angle and length. Moreover, the greatest water surface depressions – both at the nose and in the lee of the obstruction – occurs at a deflector angle of 90°, and generally increases in magnitude with increasing deflector length.

5.3.2 Velocity

As with Ouillon and Dartus' (1997) study of flow around groynes, the streamlines upstream of the deflectors indicate a strong curvature of the velocity field. Similar to those authors' description, the flow field near deflectors reveals a three-dimensional recirculation caused by the downflow in front of the obstruction and subsequent ejection at the nose. The flow separation is a result of the stagnation pressure at the front of the obstruction and the corresponding build-up of dynamic pressure at the bed (Graf and Istiarto, 2002), which concentrates upstream flow to form a sideward flow that accelerates and detaches around the obstruction (Salahedin *et al.*, 2004). Because the lateral pressure gradient is ultimately the cause of flowline skew (Ahmed and Rajaratnam, 1998), the distance of upstream separation (F_s) should be related to the upstream extent of the dynamic pressure build-up. Combining Figures 5-4a and 5-5a, both the upstream pressure gradient and the flow separation distance increase with contraction ratio. Theoretically this is sensible, as the approach flow is forced to separate at greater distance upstream to overcome the pressure gradient set by the obstruction (Dey *et al.*, 1995).

When relating flow to scour around abutments, flow patterns near the upstream nose and contracted regions are of primary concern (Molinas and Hafez, 2000). Most literature, however, focuses on the length of the downstream recirculation zone, and thus very little attention has been paid to the size and shape of the upstream separation zone (*ibid.*). As a result, there are few available examples for comparison with our observed F_s and F_w values.

Ahmed and Rajaratnam (1998) examined flow separation around bridge piers, and observed that flow becomes appreciably curved at non-dimensional distances (normalized by pier radius, R) of $F_s/R = 4$, with a maximum turning angle at $F_s/R = 1$. However, flow around piers is allowed to separate around both sides of the obstruction, whereas flow around abutments and deflectors occurs only on the nose side (Kothyari and Ranga Raju, 2001). Therefore, comparison with the values of Ahmed and Rajaratnam (1998) may not be applicable.

As part of a sensitivity analysis of scaling issues concerning flow around weirs in a laboratory flume, Ettema and Muste (2004) examined the effect of obstruction length on upstream separation distances. Using 90° weirs of contraction ratios of 0.11, 0.22, and 0.33, they found that non-dimensional separation distances (F_s/L) initially increase and subsequently decrease with contraction ratio, with a maximum value found at approximately $F_s/L = 2$ for $CR = 0.22$. This compares favourably with our findings of F_s/L variation with contraction ratio for the 90°

deflectors, which increased from 1.35 to 2.15 then decreased to 1.80 for $CR = 0.10$, 0.20, and 0.30, respectively (Figure 5-7a).

Description of separation zone width is also underrepresented in the literature. Kwan (1984, reported in Lim, 1997) stated that the non-dimensional width of flow affected by streamline curvature (F_w/L) around 90° abutments varied from approximately 1.1 to 1.5. While Kwan's (1984) separation width values are comparable to our values for the 45° and 135° deflectors of CR = 0.10 (Figure 5-7b), it is considerably lower than our findings for the 90° deflectors ($F_w/L = 3.8$). However, it is possible that the flow meter used to record velocity was not sensitive enough to identify flow angles of less than 10°, and thus the reported width of the contracted zone could have been underestimated.

Molinas and Hafez (2000) examined flow curvature around abutments of varying contraction ratios, and found that the non-dimensionalized flow contraction width (F_w/L) decreased with increasing contraction ratio. For $CR = 0.10$, 0.20, and 0.30, flow was found to be virtually parallel to the approach flow (angled less than 5°) at F_w/L values of approximately 4, 3, and 2.5, respectively. Our findings of flow contraction zone width for the 90° deflectors (Figure 5-7b) were similar, showing F_w/L values of 3.80, 3.12, and 2.48, respectively.

Whereas the zone of separation around bridge piers is almost circular in shape concentric to the pier (Dey *et al.*, 1995), around abutments it is more kidney-shaped, with a slight elongation on the upstream side. Given the differences in flow separation patterns around piers and abutments (Kothyari and Ranga Raju, 2001), an asymmetrical separation zone shape would be expected near deflectors. As shown in Figure 5-1b, the shape of the upstream separation zone around deflectors is dictated by values of F_s and F_w. Because values of F_s increase proportionally more rapidly than F_w with increasing deflector angle and contraction ratio (Figures 5-5 and 5-7), we can thus conclude that the shape of the separation zone becomes increasingly elongated (less circular) as deflector length and angle increase.

With respect to nose velocity amplification, as discussed by Molinas *et al.* (1998), an increase in contraction ratio resulted in greater values of Λ_n (Haltigin *et al.*, 2004). Molinas and Hafez (2000) reported Λ_n values ranging from 1.1 to 1.6, whereas our Λ_n values ranged from 1.6 to 2.4 for contraction ratios of 0.1 and 0.3, respectively. Although, qualitatively, these trends are similar, a quantitative comparison shows that our values averaged approximately 60% higher. However, it must be noted that Molinas and Hafez (2000) used a depth-averaged model, and thus were comparing average velocity values for the entire flow column whereas we calculated velocity amplification relative to the approach velocity at the bed. Taking average values from our flow columns at the nose normalized by the average approach flow (U_0 = 25cm/s), we exhibit values ranging from 1.05 to 1.82 for CR = 0.10 and 0.30, respectively, which is more in line with their findings.

5.3.3 Downflow

Similar to dynamic pressure, virtually all literature concerning flow and scour near instream obstructions makes passing mention of the importance of downwelling on the scouring process (e.g. Melville, 1997; Lim, 1997; Kothyari and Ranga Raju, 2001). However, few studies incorporate this parameter into discussion.

Certain studies (e.g. Ouillon and Dartus, 1997; Bradbrook *et al.*, 2000) have linked downwelling with negative dynamic pressure. However, the only regions that we found downwelling to coincide with negative pressure were immediately downstream of the deflector noses. We also found downwelling to occur in regions of high dynamic pressure immediately upstream of the deflectors, indicating that the majority of downwelling is a result of vortex formation.

Of the few studies that have incorporated quantitative description of downwelling strength, Ahmed and Rajaratnam (1998) noted that the component of downflow in front of bridge piers in the absence of scour holes will be approximately 35% of the approach flow. As shown in Figure 5-5b, similar values were found for deflectors, though a slight dependence on obstruction orientation is evident. Specifically, for the deflectors of CR = 0.25, maximum downwelling values ranged from 18.3% to 43.5% of approach velocity values, averaging 36.1%. The average value is similar to the 35% prediction made by Ahmed and Rajaratnam (1998).

Ahmed and Rajaratnam (1998) also noted that vertical flow is dependent on the relative flow depth, which is defined as the ratio between flow depth and pier radius. As the relative flow depth decreases, the downwelling component can attain almost 75% of approach values. In essence, this means that the wider the obstruction, the greater the vertical velocity component. As described in Haltigin *et al.* (2004), the same holds true for deflectors of 90° and 135°. As the deflectors increased in length – holding flow depth constant – downwelling-to-approach velocity ratios ranged from 11.7% to 29.4%, 31.1% to 48.9% and 11.1% to 60% for the 45°, 90°, and 135° deflectors, respectively. Again, the general statement of stronger downwelling with deflector length should be modified to reflect a certain dependence on obstruction angle, as the downflow for 45° deflectors was of constant magnitude for contraction ratios greater than 0.15.

Additionally, Ettema *et al.* (1998) have linked decreasing vortex strength with increased vorticity, which in turn is related to the ability of the vortex to evacuate sediment from the scour hole. Figure 5-6 showed that the primary vortices around deflectors angled closer to 90° are smaller than near obstructions of greater or lesser angles. Therefore, it would seem to indicate that vortex formation and strength are dependent on obstruction orientation. Because vortex strength is related to equilibrium scour depths (Mia and Nago, 2003), it is possible that differences in scour depths around angled obstructions (e.g. Kuhnle *et al.*, 2002; Biron *et al.*, 2004a) could be related to the size and strength of the primary vortex.

In conclusion, numerous aspects of the flow field have been shown to be highly dependent on an obstruction's angle of orientation and its length. Dynamic pressures (i.e. water surface variations), velocity magnitudes and angles, and downwelling have all been linked to scour hole formation (Thompson, 2002; Molinas, 1998; Ahmed and Rajaratnam, 1998). Therefore, it was important to systematically examine how the flow properties related to scour varied with obstruction geometry, as it is now possible to examine how deflector design – and the associated changes in flow – relates to scour hole development.

6. FLOW FIELD RELATIONSHIP TO BED TOPOGRAPHY

6.0 PREFACE

Chapter 4 illustrated that a three-dimensional numerical model could be used to successfully simulate the flow field around paired stream deflectors, while Chapter 5 used the model to examine changes in flow patterns resulting from the alteration of deflector length and orientation. Given that various studies have illustrated that obstruction geometry also has an effect on bed scouring (e.g. Melville, 1997; Ettema *et al.*, 1998; Kuhnle *et al.*, 2002), it was necessary to address a third and final objective of the thesis: to relate changes in the flow field resulting from altering the deflector geometry to the scour hole at various times throughout bed evolution.

Scouring results from a complex interaction between the flow field and the bed (Kothyari and Ranga Raju, 2001). Scour pools increase in depth over time in a non-linear fashion, adjusting constantly until a level of equilibrium is attained (Melville and Chiew, 1999). Under 'clear-water' conditions – when the approach flow is incapable of transporting sediment – equilibrium depths are approached asymptotically (Figure 2-6a), ultimately reaching a balance whereby flow within the scour hole is no longer able to evacuate sediment (Lim, 1997).

Because most of the research on scour has been done in an engineering context, primarily around bridge piers and abutments, many existing scour depth equations yield only a maximum depth (e.g. Melville, 1997; Lim and Cheng, 1998), although some authors have also incorporated time into the predictions (e.g. Ettema, 1980; Cardoso and Bettess, 1999; Oliveto and Hager, 2002). However, given that scour around obstructions in natural channels can take place almost indefinitely (Melville and Chiew, 1999), the focus tends to remain on predicting the maximum amount of scour that will occur to ensure structural stability (Johnson, 1995).

In sum, virtually the entire focus of scour research is on *depth* only. While some authors have included area and/or volume of scour in their analysis (e.g. Kuhnle *et al.*, 1999; 2002), to our knowledge none has yet reported on how these variables change with time. When habitat rehabilitation structures are being considered, the area of the scour pool at different stages of development is important to consider. If stream restoration schemes include structures like deflectors or weirs to create ‘artificial’ pools, the goal is generally to maximize the amount of suitable habitat (Thompson, 2002). If, however, the scour hole develops too slowly, the resident fish may be forced to migrate (Ebersole *et al.*, 1997). Given that peak flood flows typically have insufficient time to generate equilibrium (i.e. maximum) depths (Melville and Chiew, 1997), it is therefore important to determine what deflector geometry would result in scour occurring the most rapidly.

The fundamental issue facing rehabilitation project failure is a limited understanding of the interaction between bed topography and the flow field (Kondolf, 1998). As such, relating pool development to the flow field properties found prior to scouring is of the utmost importance in an effort to develop design parameters. We hypothesize, considering that both flow parameters and equilibrium scour dimensions are a function of obstruction geometry, that the differences in the flow fields around structures of varying geometry should be linked to the differences in scour patterns near assorted deflectors. By examining how the bed evolves and relating it to the initial flow conditions, a more complete conceptual model of scour hole development can be provided.

The following chapter begins with a general description of scour pool development for various deflector angles, followed by a more in-depth presentation of the pools’ geometric dimensions. Maximum depths at different times were tested against a number of existing temporal scour equations. Next, the geometric dimensions of the scour holes are related to flow parameters from corresponding simulations over a flat bed, culminating in a conceptual model of scour pool development over time. The chapter concludes with a discussion relating the scour hole development observed in the laboratory to existing literature.

6.1 TEMPORAL DEVELOPMENT OF SCOUR HOLE

6.1.1 Scour hole dimensions and additional simulations

Three flume runs – termed the “timeline runs” – using deflectors at a contraction ratio (*CR*) of 0.25 oriented at 45°, 90°, and 135°, were performed to examine the evolution of bed topography (see full description of laboratory set-up in Table 3-1). The minor reductions in flow depth and average velocity from the Biron *et al.* (2004a,b) runs were necessary because numerous initial tests in the Spring of 2004 resulted in the scour hole reaching the flume base before equilibrium – defined here as less than 1mm of change in scour depth over three consecutive measurements – had been reached.

Full topography surveys for each set of deflectors were performed after the flume had been run for 5, 30, and 120 minutes. Additionally, a final topography survey was carried out after the scour hole adjacent to the deflectors had reached equilibrium, at times of 1070, 960, and 600 minutes, respectively, for the 45°, 90°, and 135° deflectors. Additionally, maximum scour depths were recorded at numerous times throughout pool development (see Section 3.1.3). The dimensions used in the subsequent analyses are defined in Figure 6-1, where $S_{u\text{-}b}$, $S_{d\text{-}b}$, and $S_{w\text{-}b}$ are measured relative to the deflector-bank junction, and $S_{u\text{-}n}$, $S_{d\text{-}n}$, and $S_{w\text{-}n}$ are measured relative to the deflector nose.

It should be noted that some minor asymmetry was found to exist between the pools around the individual deflectors of each pair due to slightly non-uniform flow conditions at the flume inlet. However, scour depths for any given pair never varied by more than 5mm at any measurement interval, and differences in planform

Figure 6-1: Definition sketch of scour hole geometry variables. Scour hole boundary is defined by topography measurements greater or equal than 2mm below original bed level.

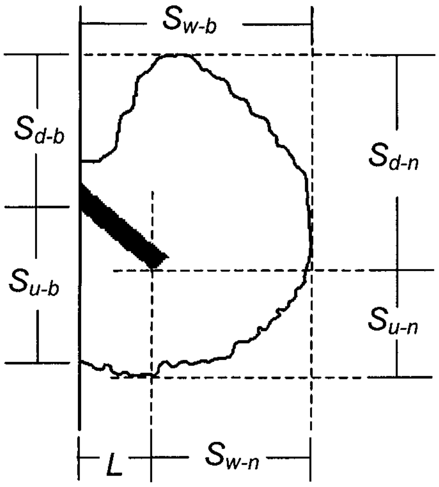

dimensions were typically less than 2cm. Therefore, the values reported throughout this chapter are averaged between the deflector pairs.

In addition, new flow simulations had to be performed to reflect the changes in laboratory conditions between the Biron *et al.* (2004a) runs and the timeline runs. Because all model conditions (Table 5-1) were held constant between the two cases except for average velocity and flow depth – which were reduced by 0.03m/s and 0.005m, respectively, for the timeline runs – it is unlikely that significant errors would have arisen to invalidate the model evaluation (Section 4.1). Subsequent analysis of the timeline simulations revealed that trends for all of the flow parameters discussed in Chapter 5 were maintained (described in Section 6.2.1; see Table 6-5 for details), and are deemed to be reliable.

6.1.2 Scour Hole Planform Geometry

Digital Elevation Models (DEM) of bed topography at different times are shown in Figure 6-2, with the corresponding dimensions presented in Table 6-1. For all angles, scour began at the deflector nose almost immediately upon starting the flume. Although most of the scour after five minutes was still concentrated near the nose for each case, several differences had already availed themselves. For instance, the 45° deflectors only exhibited scour along the upstream face, whereas the holes around the 90° and 135° deflectors extended along both the upstream and downstream faces.

Table 6-1: Scour hole geometry dimensions. Variables are as defined in Figure 6-1. All length values are in units of centimeters.

		from bank			*from nose*		
Angle	Time (min)	$S_{u\text{-}b}$	$S_{d\text{-}b}$	$S_{w\text{-}b}$	$S_{u\text{-}n}$	$S_{d\text{-}n}$	$S_{w\text{-}n}$
45°	5	-	8.8	7.1	2.8	3.8	2.3
	30	-	12.3	8.6	4.0	7.3	4.0
	120	-	13.4	9.4	4.5	8.4	4.4
	equilibrium	1.9	15.0	10.9	6.7	10.0	5.9
90°	5	-	4.8	8.9	4.2	4.8	4.1
	30	4.1	9.5	11.0	5.0	9.5	6.5
	120	5.3	12.3	11.5	6.5	12.3	7.0
	equilibrium	8.2	13.0	13.9	8.5	13.0	9.2
135°	5	-	2.6	7.3	2.1	7.6	3.1
	30	6.5	4.5	9.6	2.7	9.6	5.5
	120	8.5	6.4	11.0	4.1	11.4	6.5
	equilibrium	10.4	6.4	12.2	5.6	11.4	7.8

Figure 6-2: Temporal evolution of bed topography around deflectors. Time at equilibrium is for 45°, 90°, and 135° deflectors is 1070 min, 960 min, and 600 min, respectively.

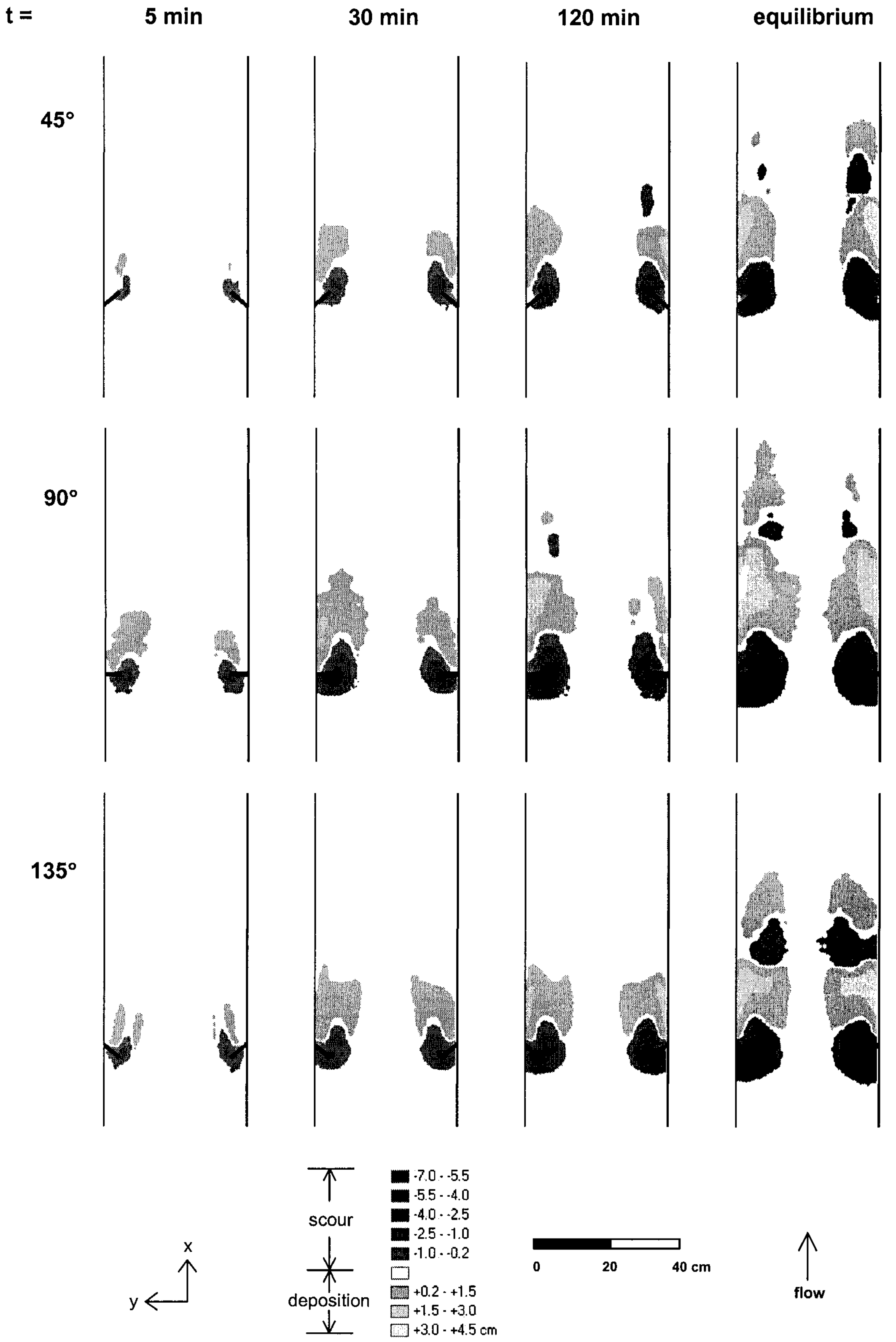

In addition, scouring extended nearly straight downstream for the 45° and 90° cases, while the 135° hole was projected more towards the center of the channel. The lip of the hole had migrated appreciably upstream from the nose for the 90° deflectors ($S_{u\text{-}n}$ = 4.2cm), but did so only marginally for the 45° and 135° runs ($S_{u\text{-}n}$ = 2.8 and 2.1cm, respectively). Furthermore, the total downstream migration from the nose ($S_{d\text{-}n}$) varied by a factor of two, with values ranging from 3.8cm to 7.6cm for the 45° and 135° deflectors, respectively. Moreover, the lateral extent of the scour hole from the nose ($S_{w\text{-}n}$) varied greatly, with values of 2.3, 3.1, and 4.1cm for the 45°, 135°, and 90° deflectors, respectively.

Deposition patterns at the first time interval also differed markedly between the three runs. For the 45° case, sedimentation had only taken place behind the deflector in the recirculation zone. Most of the deposition near the 90° deflectors also occurred in the recirculation zone, although some had taken place downstream of the hole and towards the center of the channel. Finally, the 135° run exhibited deposition in the form of two ridges adjacent to the scour hole.

After 30 minutes, the general planform geometry of the scour holes for all angles had become more similar to each other, having taken on more of a kidney shape. Scour had begun to take place along the downstream face of the 45° deflectors, but did not yet extend to the bank on either side. The 135° hole, meanwhile, had reached the upstream bank ($S_{u\text{-}b}$ = 6.5cm), while the 90° scour hole now extended to the bank on both the upstream and downstream sides of the obstruction. Upstream of the deflector nose, the scour hole had increased the most for the 45° runs, followed by the 90° and 135° holes ($\Delta S_{u\text{-}n}$ = 1.2cm, 0.8cm, and 0.6cm, respectively). The downstream extent of the hole was now nearly double that upstream for the 45° and 90° deflectors ($S_{d\text{-}n}/S_{u\text{-}n}$ = 1.8 and 1.9, respectively), while the 135° hole was now over triple the length downstream ($S_{d\text{-}n}/S_{u\text{-}n}$ = 3.6).

Deposition had reached the downstream bank for all angles, although the 90° deposition zone appeared to have grown the most. The deposition zone was still much narrower than the scour zone for the 45° deflectors, slightly wider for the 90° runs, and greatest for the 135° case.

After the flume had been run for two hours, the 45° scour hole exhibited almost equal streamwise extents relative to the nose in the upstream and downstream directions, but had not reached the bank on either the flow or lee sides. The extent of the scour hole along the bank for the 90° deflectors was now almost as long downstream as upstream. Although scouring was also occurring along both banks for the 135° deflectors, the extent was still much greater in the upstream direction.

Upstream from the deflector nose, the scour hole had grown by only 0.5cm for the 45° deflectors (ΔS_{u-n} = 0.5cm), while the 90° and 135° holes had lengthened by 1.5cm and 2.4cm, respectively. Downstream from the nose, scour extent was the greatest for the 90° deflectors (S_{d-n} = 12.3cm) and decreasingly so for the 135° and 45° deflectors (S_{d-n} = 11.4cm and 8.4cm, respectively). Proportionally, the downstream and upstream extents were now approximately equal for the 45° and 90° holes (S_{d-n}/S_{u-n} = 1.87 and 1.89, respectively), but the 135° scour hole was nearly threefold the upstream length in the downstream direction (S_{d-n}/S_{u-n} = 2.78).

Deposition zone width was still approximately equal to scour hole width for the 45° runs, while the 90° and 135° deposition zones were still slightly wider than the scour hole. Furthermore, residual scour pools had begun to develop downstream of the deposition zones, indicating that scouring near the deflectors had a considerable impact on the downstream flow field.

At equilibrium, the scour hole extended to the upstream and downstream banks for the 45° and 90° runs, but only to the upstream bank for the 135° run. Values of S_{u-b} increased with greater deflector angles, ranging from 1.9cm to 10.4cm for the 45° and 135° deflectors, respectively. In general, the scour hole was widest at the nose.

Upstream from the nose, scour extent was the greatest for the 90° case (S_{u-n} = 8.5cm), followed by the 45° (S_{u-n} = 6.7cm) and 135° (S_{u-n} = 5.6cm) runs. The same trend was evident in the downstream direction, with values of S_{d-n} ranging from 13.0cm to 10.0cm, respectively. Proportionally, though, the downstream extent of scour increased with deflector angle, with S_{d-n}/S_{u-n} values of 1.49, 1.53, and 2.03, respectively. This indicates that downstream scour extents are virtually constant for the downstream facing deflectors, but increase more rapidly with upstream-facing obstructions.

The width of the primary downstream deposition zone followed a similar trend as the scour holes. In the 45° case, the deposition zone was almost perfectly aligned in the streamwise direction as the scour zones. As the deflector angle increased, more deposition was occurring nearer the center of channel. Moreover, residual downstream pools and additional deposition zones were now present for all angles – both having migrated downstream from the previous interval – thereby reflecting the ongoing modification of the downstream flow field. However, it may be misleading that the pool downstream of the 45° deflectors appears to be the largest and deepest of the three. Because equilibrium had been defined by stability of the scour pool adjacent to the deflectors, the flume had run for the longest amount of time for the 45° run (see Section 6.1.2). It is therefore entirely possible, if not likely, that the downstream pools would have continued to develop over time. However, this was not the focus of the present study, and is therefore discounted from further discussion.

To summarize, the equilibrium scour hole extended upstream and downstream along the bank relative to the deflector-bank junction in different proportions for the three deflectors. Values of S_{d-b} were greater, equal, and less than corresponding values of S_{u-b} for the 45°, 90°, and 135° deflectors, respectively, indicating that scour extent near the bank is greatest in the direction of deflector orientation.

Relative to the nose, upstream, downstream, and lateral scour extents were greatest for the 90° deflectors. In the upstream and lateral directions, scouring was greater for the 45° deflectors than for the 135° deflectors, while the downstream scour extent was greater for the 135° deflectors than for the 45° deflectors.

6.1.3 Scour Depth

Maximum scour depths over time for the three scour holes are presented in Figure 6-3a. At all points in time, the maximum depth was located at the deflector nose. In addition – as with the planform dimensions presented in the previous section – all values shown are averages for the deflector pairs.

Initially, scour depths for the three angles are reasonably similar. After only 30 minutes, however, the 90° pool was already deeper than the 135° and 45° pools by over 1cm. The growing disparity continues over time, with the 90° hole eventually reaching the greatest equilibrium depth (d_{se} = 6.0cm), followed by the 135° (d_{se} = 4.9cm) and 45° (d_{se} = 4.5cm) scour pools.

For each deflector, a logarithmic line of best fit explains variations of scour depth with time quite well (Table 6-2). Note that because the equations are logarithmic in form, by definition they are not applicable beyond $t/t_e = 1$ because they do not reach an asymptote at $d_s/d_{se} = 1$ and thus would predict scour depths greater than equilibrium values at $t/t_e > 1$. Trendline slopes average approximately 0.6 and intercepts average approximately 1.3. Variations in the trendline slope show that scour development occurs more rapidly in relation to equilibrium depth as the deflector angle decreases, implying that the hole near the 45° deflectors was approaching equilibrium the fastest.

Figure 6-3: Evolution of: (a) scour depth at the deflector nose (d_s) over time (t), and; (b) dimensionless scour (d_s/d_{se}) and time (t/t_e), as normalized by equilibrium values.

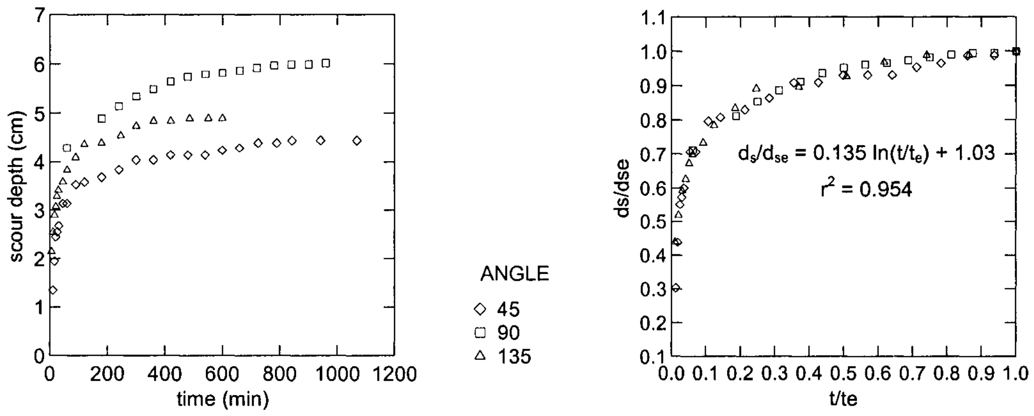

Table 6-2: Lines of best-fit for measured scour depth (d_s) in centimeters over time (t) in minutes.

Angle	Equation	r^2
45°	$d_s = 0.626 \ln(t) + 0.341$	0.943
90°	$d_s = 0.609 \ln(t) + 2.092$	0.973
135°	$d_s = 0.585 \ln(t) + 1.346$	0.985

When scour depth (d_s) and time (t) are normalized by their respective equilibrium values (d_{se} and t_e), the three curves collapse into a single trend (Figure 6-3b), explained by:

$$d_s/d_{se} = 0.135 \ln(t/t_e) + 1.03;\ r^2 = 0.952 \quad [6\text{-}1]$$

As described in Section 2.2.5, a number of other studies have also developed equations to predict scour depth over time, against which the data presented in Figure 6-3 were tested. Ordinary least squares regressions were performed using measured scour data as the independent variable, with regression slopes (a), intercepts (b), and coefficients of determination (r^2) presented in Table 6-3. In cases where an initial value of U was required, upstream velocity measured in the laboratory was used. However, given that predicted velocities near the inlet almost perfectly matched the laboratory measurements, the use of either predicted or measured values would suffice.

Certain modifications to the published equations needed to be made before the analysis could be performed. The Melville and Chiew (1999) equation – hereafter referred to as model *MC* – requires the definition of critical velocity (U_c), or the velocity at which sediment motion is initiated – which was calculated following Umbrell *et al.* (1998):

$$U_c = 1.58[(SG-1)gd_{50}]^{1/2}(Y_0/d_{50})^{0.167} \quad [6\text{-}2]$$

where SG is the specific gravity of sediment ($SG = 2.65$), g is the acceleration due to gravity, d_{50} is the median diameter of the bed sediment mixture ($d_{50} = 0.0011$m), and Y_0 is the approach flow depth ($Y_0 = 0.090$m). Note that the MC model was published

Table 6-3: Ordinary least squares regression slopes (*a*), intercepts (*b*), and coefficients of determination (r^2) between predictive equations of scour hole depth over time and scour data from the present study. Equation variables are as defined in Section 2.2.5. Bold values indicate regression intercepts that were not significantly different from zero at the 95% confidence level.

Source	Equation	*a*	*b*	r^2
present study	$d_s/d_{se} = 0.135 \ln(t/t_e) + 1.03$	0.99	**0.03**	0.954
Oliveto and Hager (2002)	$d_s = 0.068 N\sigma_g^{-1/2} F_d^{1.5} \log(T)$	0.43	0.63	0.754
Cardoso and Bettess (1999)	$d_s/d_{se} = 1\text{-}\exp[-1.025(t/T)^{0.35}]$	0.78	0.17	0.971
Melville and Chiew (1999)	$d_s/d_{se} = \exp\{-0.03[(U/U_c)\ln(t/t_e)]^{1.6}\}$	1.03	**-0.17**	0.976
Whitehouse (1997)	$d_s/d_{se} = 1 - \exp[-(t/T)^p]$	0.85	0.53	0.982
Franzetti *et al.* (1982)	$d_s/d_{se} = 1 - \exp[a_1(Ut/L)^{a2}]$	0.39	-0.43	0.884
Ettema (1980)	$d_s/L = K_1 \log(d_{50}\upsilon t/L^3) + K_2$	0.99	**0.17**	0.950

with an apparent misprint in the U_c/U term, as application of the equation resulted in negative scour depths. Therefore, the term was inverted to U/U_c.

Additionally, the Ettema (1980) model – referred to as model *ET* – required two constants: K_1 and K_2. Although the best fit lines for the 45°, 90° and 135° runs were found to have differing values of these constants, (K_1 = 0.296, 0.303, and 0.280; K_2 = 1.546, 1.844, and 1.663, respectively), average values of K_1 = 0.293 and K_2 = 1.684 were used to amalgamate the three data sets. All other equations were applied as published.

Figure 6-4 shows the relationship between the laboratory scour data and the values predicted by the various equations. Four of the models – *MC*, Cardoso and Bettess (1999; "*CB*"), Whitehouse (1997; "*WH*"), and *ET* – performed quite well, with r^2 values ranging from 0.95 to 0.98 and regression slopes ranging from 0.78 to 1.03. In only one of these cases (*WH*) was there a positive bias. However, the intercept value in this case was approximately 0.5cm, indicating that while it was statistically significant, it was not substantial.

For all four models, depths early in the development of the 45° scour hole were strongly overpredicted, especially by *ET*. However, Equation 6.1 does so as well, possibly reflecting a general limitation of the four equations. While models *CB* and *WH* closely predicted intermediate scour depths for the three deflector angles, it had a slight tendency to underpredict the greater depths exhibited later in development. Conversely, *MC* had slight difficulty predicting the scour depths

Figure 6-4: Comparison of measured scour data with equations from: (a) Oliveto and Hager (2002); (b) Cardoso and Bettess (1999); (c) Melville and Chiew (1999); (d) Whitehouse (1997); (e) Franzetti *et al.* (1982), and; (f) Ettema (1980). Dotted lines indicate 1:1 relationship.

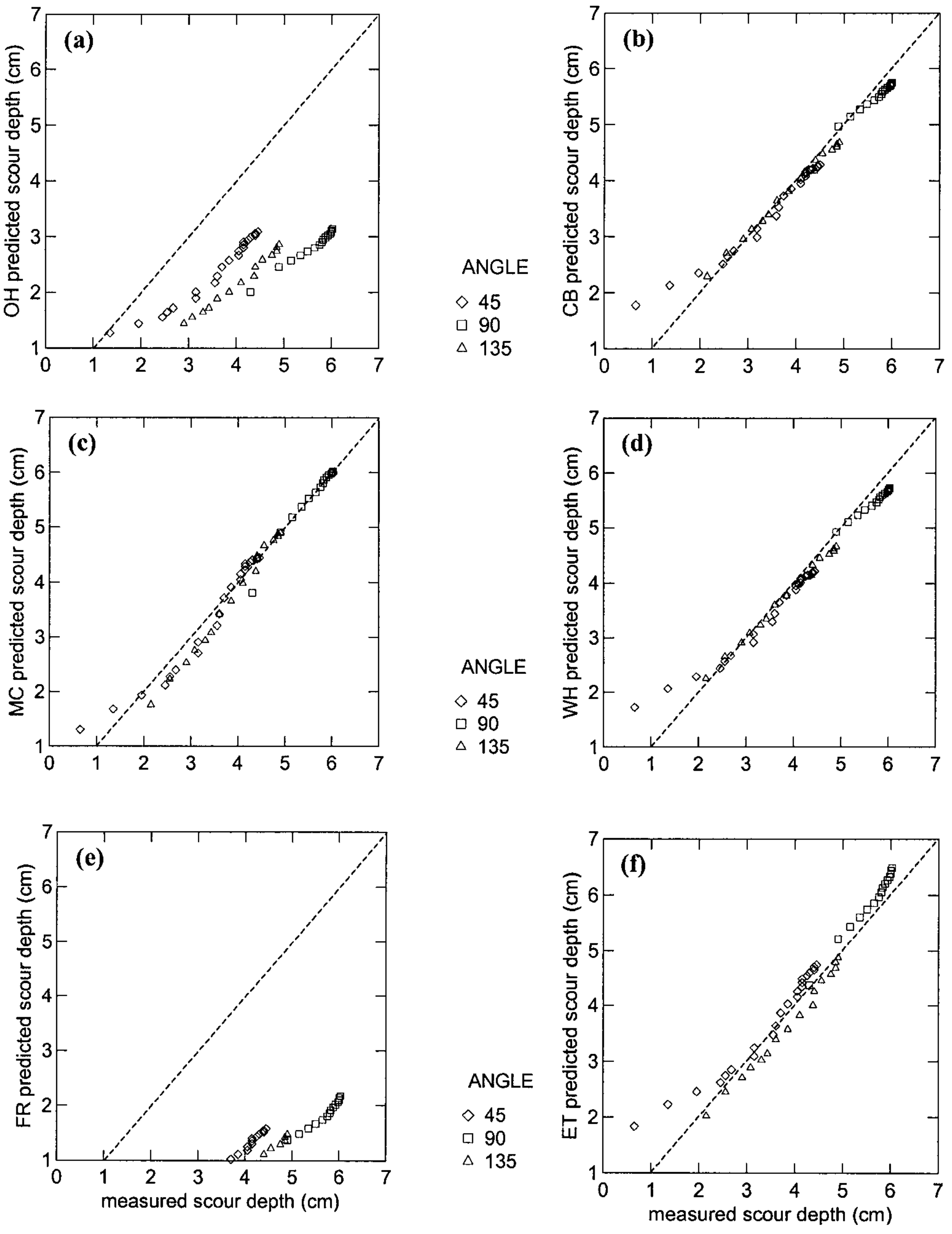

during the intermediate stages of pool development but was more accurate as the holes approached equilibrium. Meanwhile, *ET* worked best for the 135° deflectors, generally overpredicting depths for the 45° run and underpredicting depths for the 90° run. While this is certainly an artefact of using average values of K_1 and K_2, it does indicate a moderate dependence of the equation on deflector angle.

The notion of angle dependence is especially evident for the Oliveto and Hager (2002; "*OH*") and Franzetti (1982; "*FR*") equations. Both models greatly underpredict scour depths at all times, with *FR* performing the least adequately. From model *OH*, individual OLS regressions were performed for the three separate data sets. Slopes for each case were found to be similar, exhibiting values of 0.60, 0.62, and 0.74 for the 45°, 90°, and 135° deflectors, respectively (Table 6-4). The intercepts differed greatly, however, with a maximum of 0.22 for the 45° runs, subsequently decreasing to -0.62 (90°) and -0.79 (135°).

Although model *FR* produced a reasonable r^2 using OLS regression ($r^2 = 0.884$), the predicted and measured scour data were, in fact, better explained with an exponential function in the form of:

$$d_{spFR} = m\, e^{n\, d_{sm}}$$

where d_{spFR} is scour depth as predicted by model *FR*, d_{sm} is measured scour depth, and m and n are constants (Table 6-4). This suggests that future applications of the *FR* equation may require a conversion factor dependent on the deflector angle.

Table 6-4: Relationship between scour depths predicted by Oliveto and Hager (2002) and Franzetti *et al.* (1982) and measured scour data, where *a* and *b* are OLS regression slopes and intercepts, and *m* and *n* are constants in an exponential function.

Angle	Oliveto and Hager (2002)			Franzetti *et al.* (1982)		
	a	*b*	r^2	*m*	*n*	r^2
45°	0.60	0.28	0.943	0.203	0.440	0.952
90°	0.62	-0.62	0.985	0.160	0.428	0.987
135°	0.74	-0.79	0.985	0.125	0.493	0.992
combined	0.425	0.63	0.754	0.215	0.385	0.912

The preceding analysis indicates that Equation 6-1 is comparable with at least four existing temporal scour depth models, and shows less angle dependence than two of them. However, only one discharge and laboratory setup was used in its development, and thus future work will be required to provide additional verification of tis transferability to a wider range of flow conditions.

6.1.4 Rate of Geometrical Change

Although scouring for all three deflectors began at the deflector nose, the pools approached planform equilibrium in different fashions. Figure 6-5a shows the upstream and downstream scour extents from the nose at each measurement interval. There appears to be three distinct phases of development in each case, as indicated by sharp breaks in slope. In the first phase, all scour holes grew more quickly in the downstream direction than in the upstream direction. During this stage, the 45° and 90° scour holes grow upstream slightly faster than they do downstream, while the downstream length of the 135° pool outpaces the upstream growth at a ratio of approximately 4:1. In the intermediate stage, the 45° and 90° pools grow in the downstream direction at a dramatically increased rate relative to upstream growth, while the 135° pool expansion in the downstream direction relative to the upstream

Figure 6-5: Proportional streamwise development of scour hole: (a) upstream and downstream magnitude extent from the nose, (b) normalized by equilibrium values. Dashed line indicates 1:1 relationship.

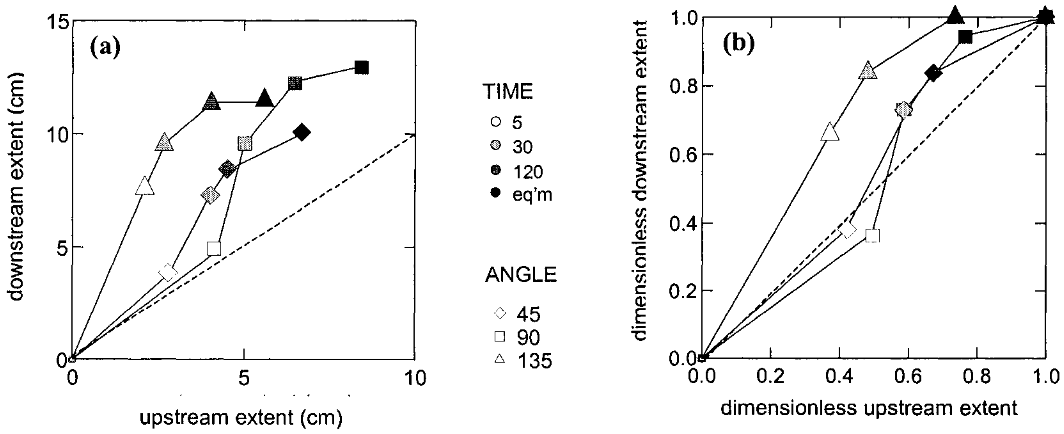

direction is reduced. In the final stage, the 45° and 90° downstream progression slows relative to the upstream progression, reverting back to a rate of nearly 1:1. The 135° pool, however, had already reached its maximum downstream extent after two hours, and thus grows only in the upstream direction until equilibrium depth had been attained.

When upstream and downstream scour extents are plotted normalized by the equilibrium values, some interesting trends are revealed (Figure 6-5b). During the first phase, although the scour holes near the 45° and 90° deflectors were increasing at a greater rate downstream in terms of absolute distances, the non-dimensional rate of increase was less than unity. Therefore, it appears that equilibrium, in fact, is initially approached more rapidly in the upstream direction than in the downstream direction for the 45° and 90° scour holes. The 135° pool, however, approaches equilibrium far more quickly in the downstream direction than in the upstream direction.

During the second phase, the rate of growth in the downstream direction is much greater for the 45° and 90° deflectors relative to growth in the upstream direction. Even though the plots are above the line of equality for the 135° pool, the slope is now less than unity, indicating that the rate of approach to equilibrium is greater in the upstream direction.

In the final stage, the 45° and 90° scour pools again approach equilibrium in the upstream direction more rapidly, indicated by a slope of less than unity. The 135° pool, though, had already reached downstream equilibrium after the second phase, and thus grew only in the upstream direction during the remainder of the time.

Combining the changes in planform geometry with evolution of maximum scour depth, the slope of the scour hole both upstream and laterally from the nose (i.e. location of maximum depth) varied over time (Figure 6-6a; please note that the time values are plotted on logarithmic axes). After the initial increase in slope upon scour initiation during the first five minutes, the upstream scour hole slope evolves very differently for the three deflectors. For the 45° scour hole, the upstream slope exhibits an abrupt increase until t = 30min, and then increases more gradually until equilibrium is reached. The upstream slope of the 90° hole also increases greatly until t = 30min, but then stays constant until t = 120min before increasing again to

Figure 6-6: (a) Upstream and (b) lateral scour hole slopes (expressed as gradients) over time, (c) and (d) normalized by equilibrium values, against non-dimensional time (*t/t$_e$*). Dashed lines indicate equilibrium slopes.

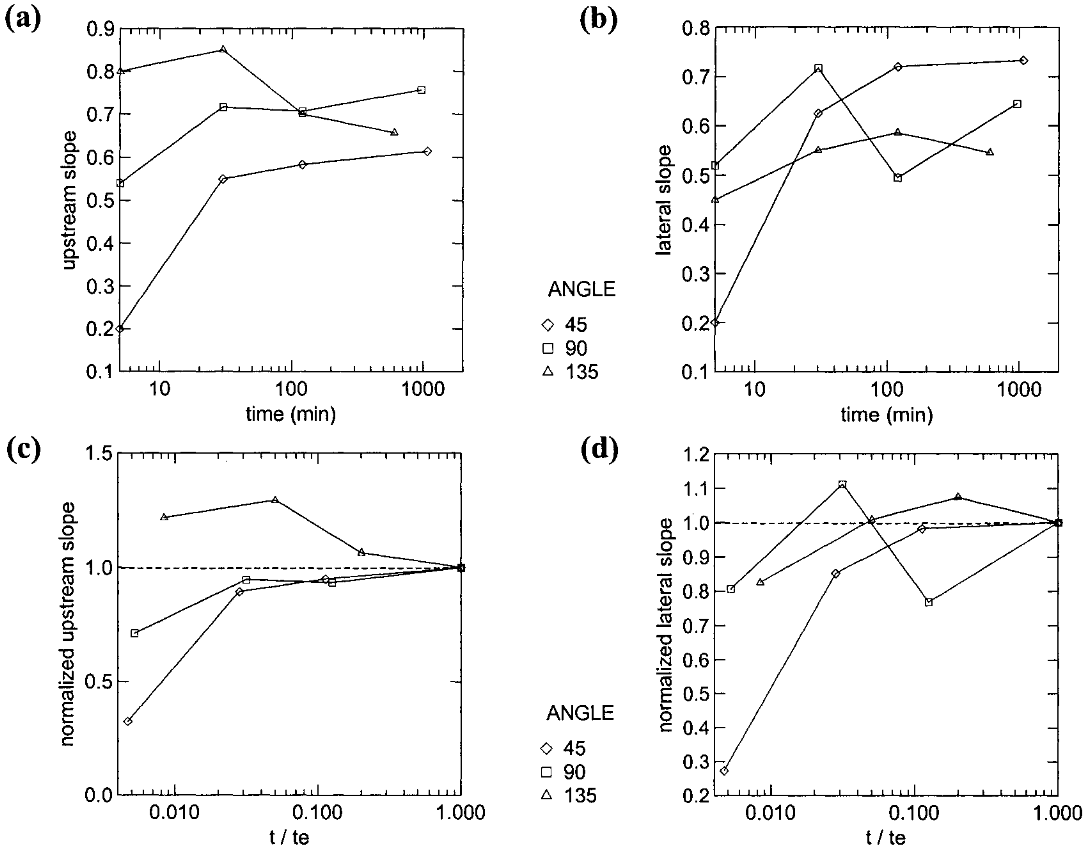

reach equilibrium. After a moderate increase from five to 20 minutes, the slope of the 135° hole decreases sharply, and subsequently increases until equilibrium.

The lateral scour slopes of the three holes also evolve in different fashions (Figure 6-6b). The lateral slope of the 45° hole follows the trend of the upstream slope, with an initial increase followed by an extended period of moderate increase. The 90° hole, meanwhile, exhibits alternating dramatic increases and decreases in lateral slope, while the 135° hole increases moderately in lateral slope until *t* = 120min, and then gradually decreases until equilibrium.

When slope and time values are normalized by equilibrium values (Figures 6-6c and 6-6d), it was found that both the 45° and 90° upstream slopes attain almost 90% of equilibrium values after 120 minutes of run time, and then gradually increase over the duration of the run. The 135° upstream slopes, however, are much greater than the equilibrium values throughout the entire duration of scour hole development, showing almost a continual decrease. The lateral slopes of the 45° hole are virtually equal to those of the upstream slopes, while the 90° hole approaches equilibrium in an iterative fashion. Finally, the lateral slope of the 135° hole begins at less than the equilibrium value, exceeds it at t = 120min, and ultimately decreases until the end of the run.

6.2 RELATIONSHIP BETWEEN INITIAL FLOW FIELD AND BED TOPOGRAPHY

6.2.1 Scour Hole and Flow Property Dimensions

Flow variables from the timeline simulations and those performed in Section 5.2 at a contraction ratio (*CR*) of 0.25 are shown in Table 6-5. Although the discharge had been decreased slightly for the timeline runs – and thus the absolute values of each variable were not equal – the general trends shown at deflector angles for each flow variable were very similar. For instance, the distance along the bank of upstream separation (F_s) increases with deflector angle, while the widths of the separation zone at the nose (F_w) are much larger for the 90° and 135° runs than the 45° tests. Additionally, the upstream and downstream extents of downwelling increase and decrease, respectively, with increasing deflector angle. Finally, the downstream location of the maximum water surface depression (P_x) decreases with increasing deflector angle in both sets of simulations.

Similarly, the scour hole geometry between the timeline and Biron *et al.* (2004a) runs also exhibit comparable trends. The upstream extent of the scour hole

Table 6-5: Simulated flow variables and selected scour hole dimensions. Flow variables are as defined in Figure 5-1, and scour variables are as defined in Figure 6.1. All distances reported are in centimeters.

Source	CR	Angle	*flow*				*equilibrium scour*				
			F_s	F_w	F_{zd}	P_x	d_{se}	$S_{u\text{-}b}$	$S_{w\text{-}b}$	$S_{u\text{-}n}$	$S_{d\text{-}b}$
Timeline	0.25	45°	2.5	12.3	5.4	16.9	4.5	1.8	10.9	6.7	15.0
		90°	9.0	14.7	10.3	12.9	6.3	8.2	13.9	8.5	13.0
		135°	12.8	15.4	4.1	10.0	4.9	11.6	13.9	6.7	7.5
Biron *et al.* (2004a)	0.25	45°	3.5	12.8	7.1	16.0	5.0	3.9	12.0	7.1	13.8
		90°	9.9	14.0	11.8	13.0	6.8	9.7	12.8	9.4	11.9
		135°	15.5	14.7	9.2	8.9	6.5	15.1	15.2	9.1	10.7

(S_{u-b}) increases uniformly with increasing deflector angle, as does the width of the scour hole. Moreover, the pool's maximum upstream extent from the nose (S_{u-n}) is greatest at 90°, followed by the 135° and 45° deflectors, respectively. Lastly, total downstream extent of the scour hole relative to the deflector-bank junction (S_{d-b}) decreases consistently with larger obstruction angles.

When the flow variables from simulations over a flat bed are compared to equilibrium scour hole geometry, some noteworthy patterns emerge. Firstly, F_s values are virtually identical to S_{u-b} in all cases, differing by an average of 0.58cm (7.1%). Next, F_w compares closely to S_{w-b} for the three angles, differing by an average of 0.85cm (7.0%). Values of S_{d-n} exceeded F_{zd} for all runs by an average of approximately 4.0cm. Finally, values of P_x are slightly greater than the corresponding S_{d-b} values, except for the Biron *et al.* (2004a) 135° run.

6.2.2 Visualization of Initial Flow Field Properties with Bed Topography

Figure 6-7 shows simulated flat-bed flow vectors, the location of the 'local' minimum pressure in the lee of the deflectors (P_{loc}), and the downwelling distribution superimposed upon changing bed elevations over time. It is evident that scouring starts at the nose of the deflectors, where the maximum velocity amplification was found. At the five-minute interval, the scour hole is roughly symmetrical about the downwelling distribution. Over the following time interval, scouring around all deflectors continues to extend downstream along the region of maximum downwelling while growing both laterally and in the upstream direction. After 120 minutes, the scour hole has now extended beyond the limit of the original downwelling distribution, and has continued to grow upstream and laterally. At equilibrium, the holes have reached their limit in each direction. Of particular note is that: (a) the upstream extent along the bank is located at the location of flow separation (F_s); (b) the lateral extent at the nose is aligned with the outward limit of the separation zone (F_w); (c) no scouring occurs beyond P_{loc}; (d) the maximum downstream extent is now approximately aligned with the deflector nose, and; (e) scour depths are roughly symmetrical around the downwelling distribution, although the downstream extent is slightly closer to the bank.

Figure 6-7: Simulated velocity vectors, P_{loc} position, and downwelling distribution with temporal evolution of bed topography.

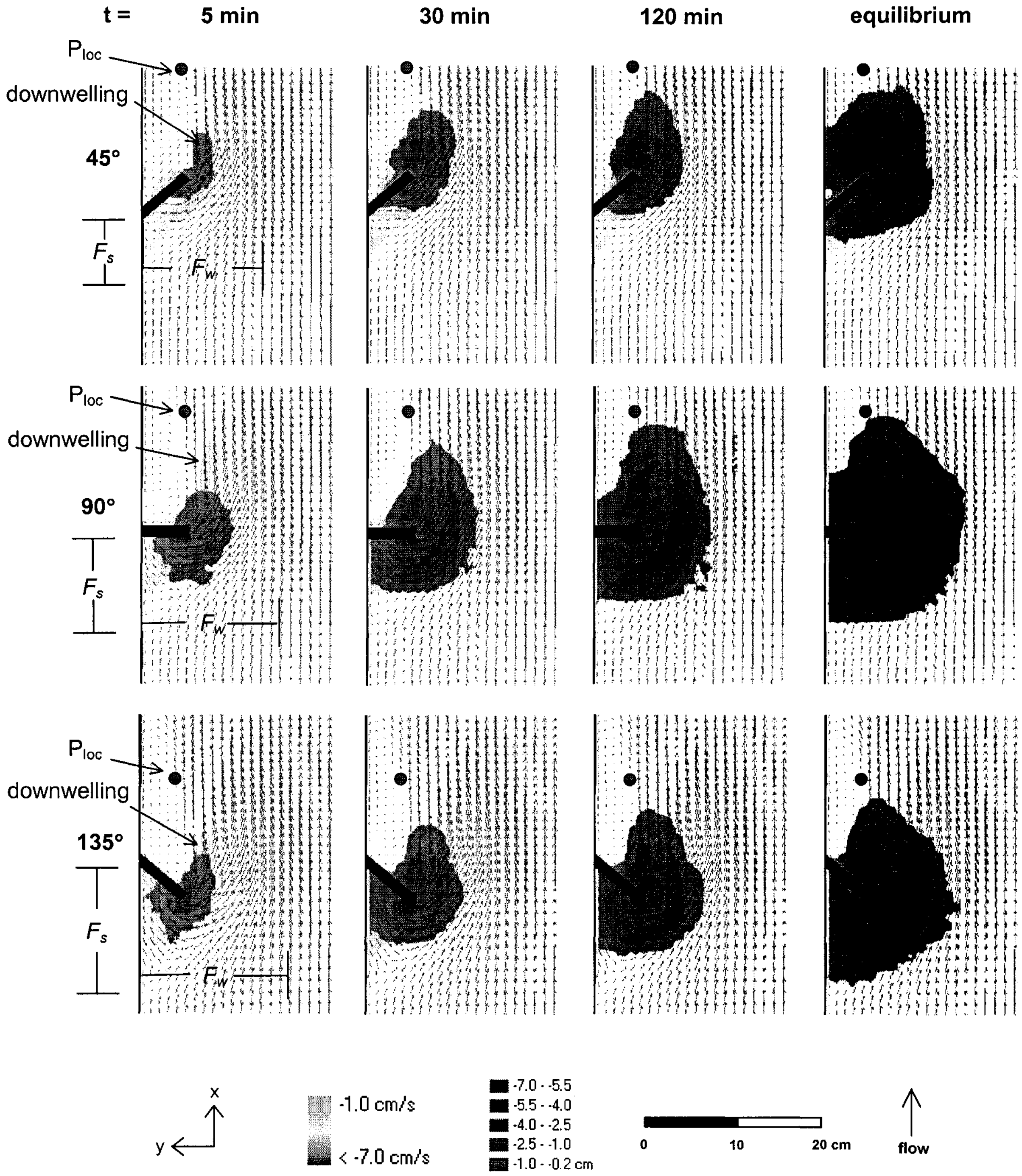

Combining the above statements reveals that some of the flow parameters can be used as points of inflection to trace out the planform geometry of the equilibrium scour hole (Figure 6-8). The steps to outline the equilibrium planform geometry based on the initial flow field and deflector position are detailed in the table below of the figure, and described as follows. First, point P1 is placed at the location of P_{loc}. Line L1 is drawn perpendicular to the bank at an upstream distance from the deflector F_s, and L2 extends laterally across the channel from the nose. Line L3 is then drawn in the streamwise direction at the deflector nose. Point P2 is inserted at the upstream flow separation point F_s, and P3 is placed along L2 at a distance F_w from the bank, corresponding to the simulated width of the upstream separation zone. Line L4 is then drawn to join P2 and the deflector nose, L5 joins the downstream deflector-bank junction with P1, and L6 joins P1 and P3. Point P5 is placed at the intersection of Lines L3 and L6. Line L7 is drawn perpendicular to the bank, extending through the intersection of L4 and L6. Point P6 is then inserted at the intersection of L6 and the bank. Finally, L8 connects P5 and P6, while L9 represents a circle incorporating P3, P4, and P5.

To trace out the final geometry, a straight line connects P2 and P4. A semi-circular arc beginning at P4 travels along L9, passes through P3, and extends to P5. From P5, the path follows L8 until its intersection with L5, along which it travels until the intersection with L7. At this point, the path follows along L7 until the intersection with the bank. Lastly, a line is drawn through the downwelling distribution, about which scour depths are virtually symmetrical.

Figure 6-9 shows the method applied to the three timeline runs (T45, T90, and T135, for the 45°, 90°, and 135° deflectors, respectively), and Figure 6-10 applies it to the Biron *et al.* (2004a) runs (B45, B90, and B135, respectively). In all cases, the upstream extent of the scour hole is clearly determined by F_s (P2). Because the upstream extent of scour from the nose (S_{u-n}) was virtually equal to $F_s + L\tan(90-\Theta)$ in all cases – where L is the lateral projection of the deflector, and Θ is the angle of deflector orientation – meaning that the location of S_{u-n} is located laterally from F_s, the use of a horizontal line between P2 and P4 described the upstream extent of the scour hole to a distance L rather well.

Figure 6-8: Placement of geometrical inflection points based on simulated flow field properties.

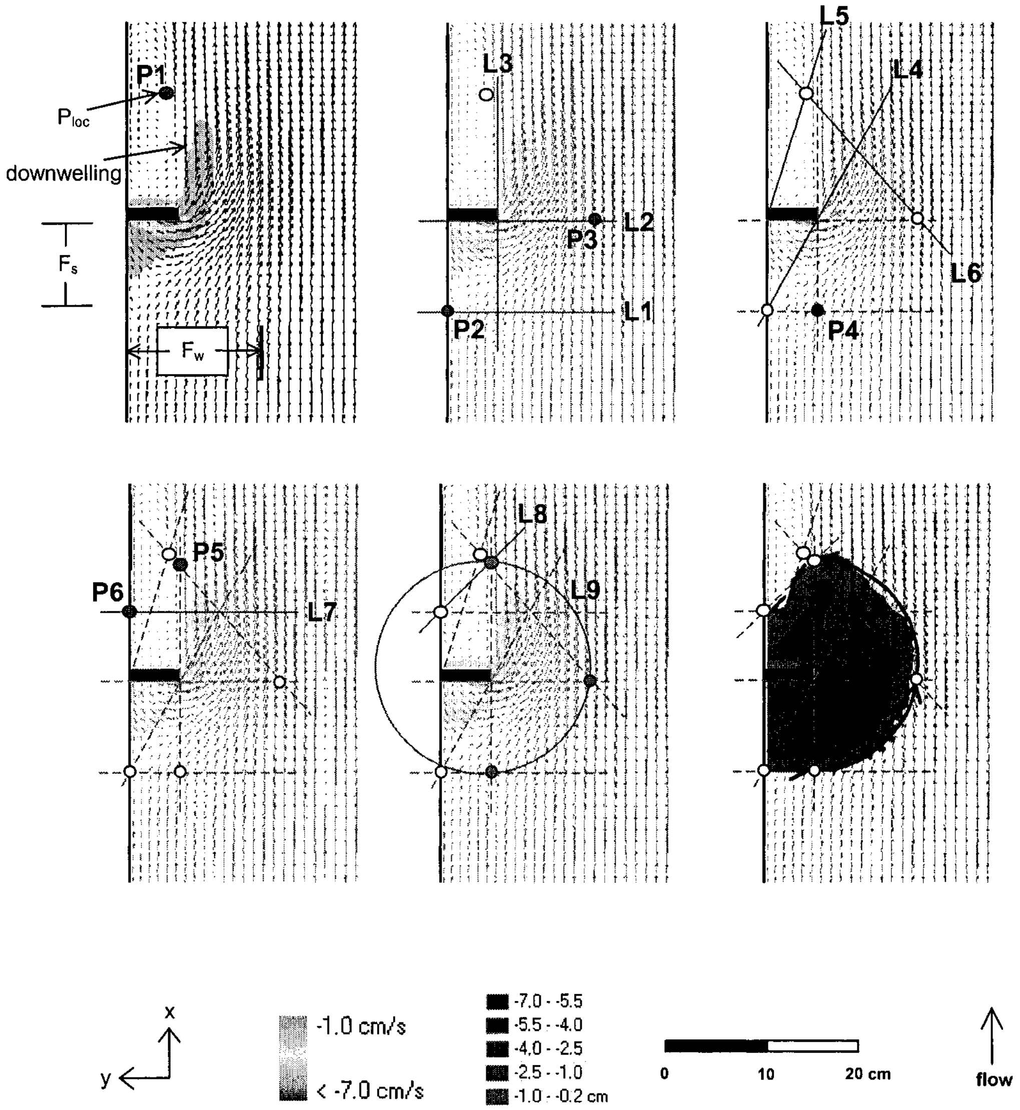

Number	Points	Lines
1	location of P_{loc}	horizontal – start at F_s
2	upstream separation point (F_s)	horizontal – aligned with nose
3	along Line 1 at distance F_w	vertical – aligned with nose
4	intersection of lines 1 & 3	angle – joining Point 2 and nose
5	intersection of Lines 3 & 6	angle – deflector-bank interface to Point 1
6	downstream deflector-bank junction	angle – joining Points 1and 3
7	-	horizontal – intersect Point 2 and Line 6
8	-	angle – joining Points 5 and 6
9	-	circle – joining Points 3, 4, and 5

Figure 6-9: Geometrical relationship between simulated flat-bed flow variables and equilibrium bed topography for timeline runs. Points and lines are inserted following Figure 6-8.

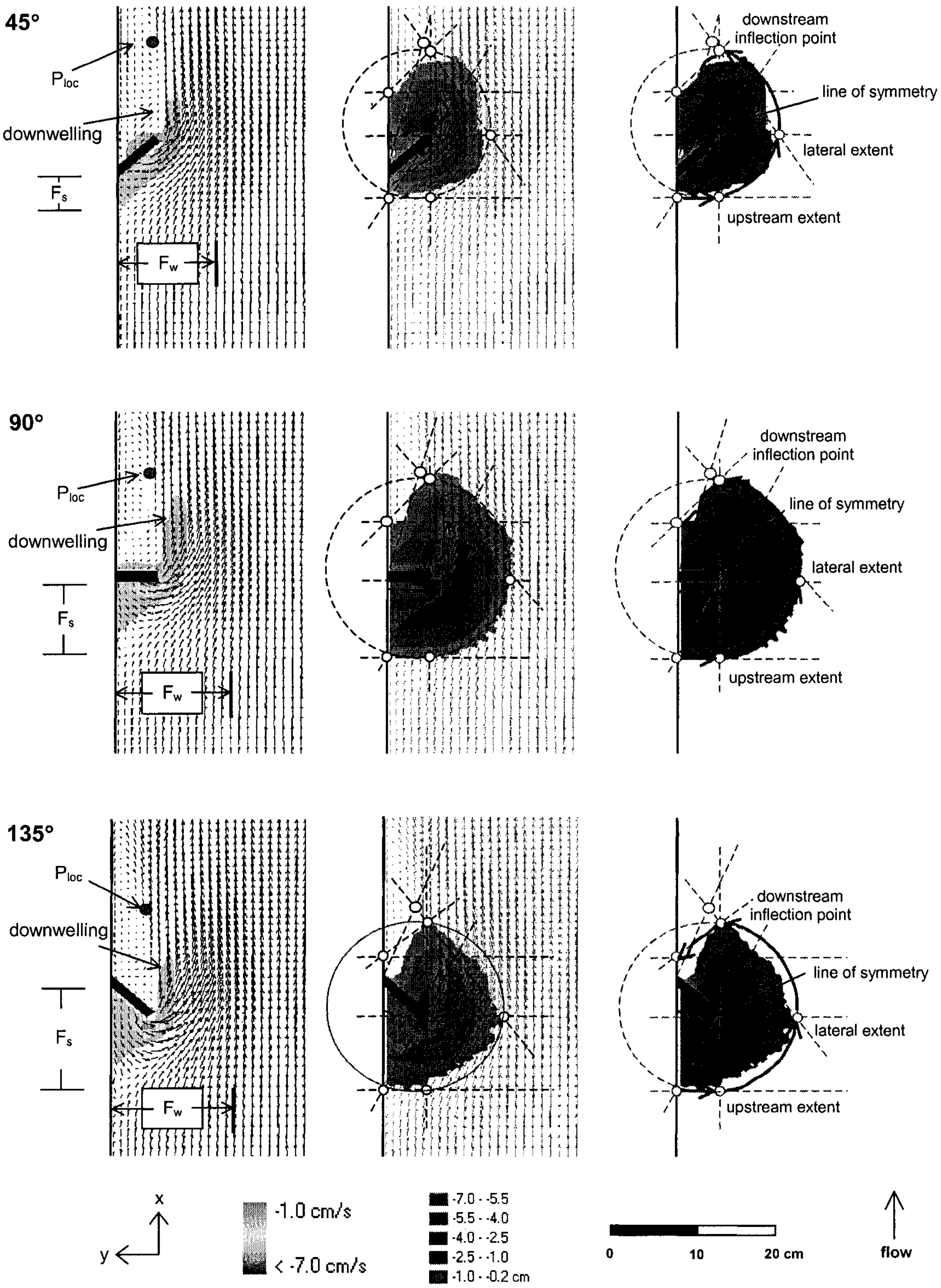

Figure 6-10: Geometrical relationship between simulated flat-bed flow variables and equilibrium bed topography for Biron *et al.* (2004a) flume experiments.

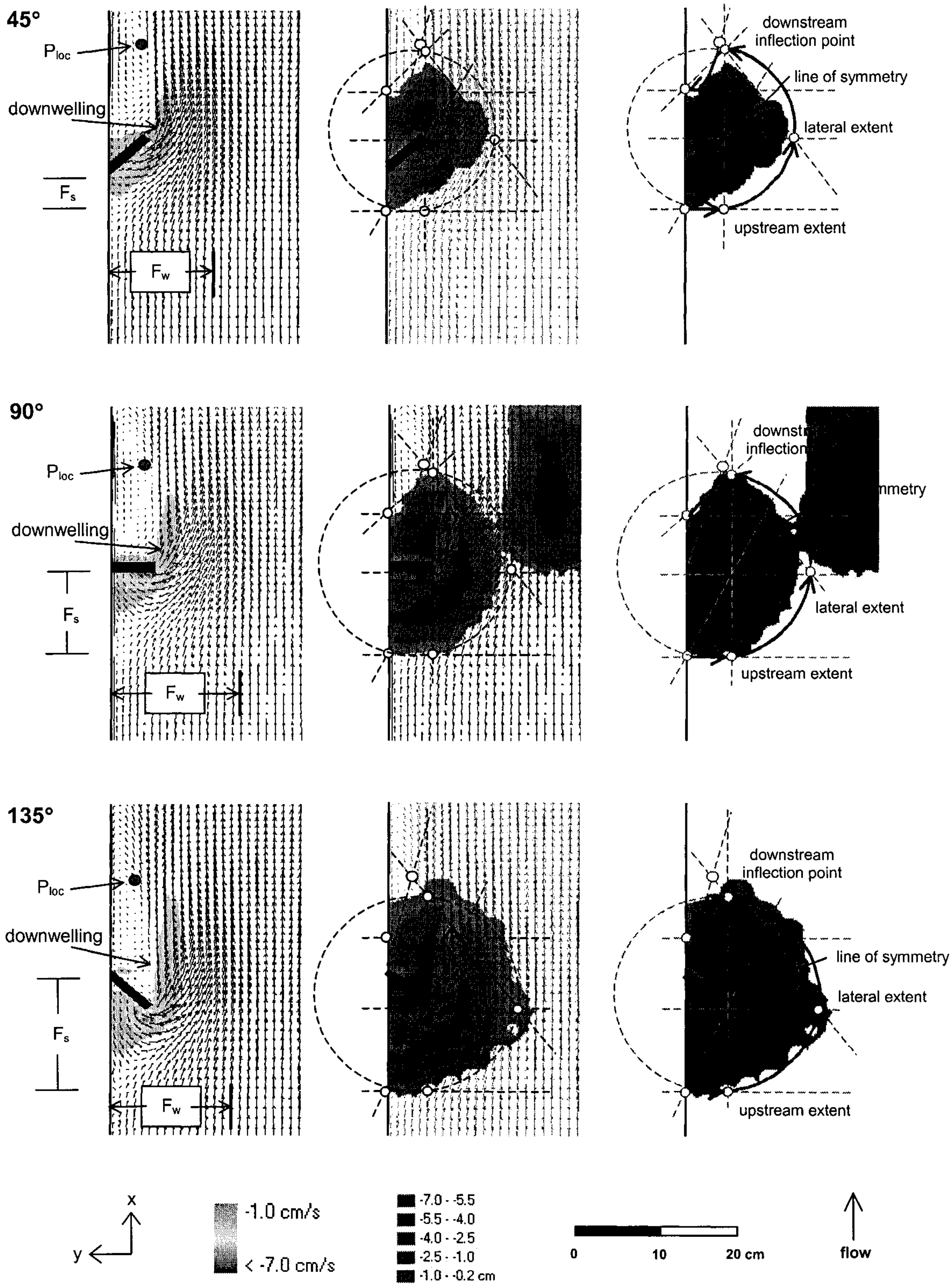

The arc between P3 and P4 reasonably represented the lateral extent of the scour holes for the T45, T90, B90 and B135 runs. For the remaining cases, a slight overestimation of scour extent was exhibited in this region. From P3 to P5, a moderate overestimation of scouring was also seen for the T135 and B45 runs, while the arc underestimated scour extent in run B135.

The path between P5 and P6 tended to work the best for the 45° and 90° deflectors in both sets of runs. For the 135° tests, however, considerable over- and underestimation of scour extents were seen for the timeline and Biron *et al.* (2004a) runs, respectively. Similarly, using P6 as the location of maximum downstream scour extent along the bank worked well for the 45° and 90° deflectors, but was seemingly inadequate for the 135° deflectors.

6.2.3 Scour Hole Initiation and Maintenance: A Conceptual Model

Although sediment transport functions were not explicitly tested in this study, it is possible to qualitatively assess the processes involved over the course of scour hole development in relation to sediment movement. Following the principles of the Exner equation, a net loss of sediment is predicted if the amount of sediment entering an area over a given time interval is less than the amount leaving the area over the same time:

$$\rho_s(\angle z_b/\angle t) = \vec{V}\,.\,\vec{q}_s \qquad \textbf{[6-3]}$$

where ρ_s is the density of sediment, z_b is the bed elevation, t is time, and $\vec{q}_s$ is the sediment transport rate in vector form. In essence, if $q_{s\text{-}in}$ is less than $q_{s\text{-}out}$ from an elementary bed area, z_b must decrease (i.e. scouring takes place). Specifically, under clear-water scouring conditions – when the approach velocity and stress are less than critical values – no sediment enters the hole and thus all of the sediment evacuation is a result of changes in flow structure due to the presence of the obstruction. Therefore, we must examine how the local flow field could contribute to sediment excavation away from the deflectors.

In general, sediment can move in two ways: if the bed shear stress is greater than the critical shear stress of the particle, or under the force of gravity in the form of local avalanches. When local stresses are great enough the bed will begin to degrade downward such that the lip of the trench is nearly vertical (Kothyari and Ranga Raju, 2001). However, if the slopes of the scour hole exceed the sediment's angle of repose, local avalanches will deposit sediment to the bottom of the scour hole (*ibid.*).

These processes can be related to changes in the slope of the scour hole over time. Theoretically, if the slope of the hole is increasing, then the hole is getting deeper more quickly than it is increasing in planform extent. Therefore, it is likely that the sediment flux is being driven by locally increased shear stress, as the bed is degrading vertically faster than the scour hole can expand outward. Moreover, if the increase in slope during a given time interval is rapid, it is possible that more than one process is contributing to maintaining the local shear stress well above critical levels. Conversely, if the slope is decreasing, the hole is getting wider more rapidly than it is deepening, and hence local avalanches are likely the dominant process.

For example, after five minutes of run time the upstream slope of the scour hole is greatest for the 135° deflectors and least for the 45° deflectors. This indicates that the ratio of vertical to horizontal scour extent increases with greater deflector angles. It is thus evident that more processes are contributing to the vertical degradation of the scour hole near as deflector angles increase. After re-examining Section 5.2, such a conclusion seems plausible. For example, the location of maximum downwelling for the 135° deflectors is at the nose whereas for the 45° deflectors it is slightly closer to the bank. Therefore, the additional momentum transfer to the bed resulting from negative vertical velocity (Lane *et al.*, 1999) combined with the augmented shear stress derived from nose velocity amplification may cause the 135° hole to deepen faster than it can grow upstream.

For the 5-30 minute interval, the increase in upstream slope is the greatest for the 45° deflectors and least so for the 135° deflectors, indicating that the scour hole for lower deflector angles is deepening faster than it is expanding upstream. Examining Figure 6-3a, it can be seen that the increase in depth for the 135° deflectors has slowed when compared to the other two deflectors, having already reached over 60% of its equilibrium value. At the same interval, the 45° and 90° holes had only reached approximately 45% of equilibrium depths. It is therefore possible that the second phase of scouring is directed primarily downward for the 45° and 90° holes and primarily downstream for the 135° deflectors.

From 30-120 minutes, the 135° scour hole exhibits a substantial decrease in upstream slope, indicating that local avalanching had become the dominant process. The upstream slopes for the 45° and 90° holes were virtually constant, and thus it appears that any sediment produced by upstream avalanching was balanced by the amount evacuated from the base of the scour hole. That the lateral slopes of the 45° and 90° holes were still increasing, though, indicates that the rate of lateral expansion was slowed. Looking at Figure 6-7, it does appear that the growth of the scour holein the cross-stream direction was greatest for the 135° deflectors, which would explain the reduction in lateral slope.

From 120 minutes to equilibrium, Figure 6-2 shows that the rate of scour hole depth increase had slowed for all three deflectors, especially for the 45° and 135° cases. Because the upstream and lateral slopes of the 135° hole are decreasing, it is likely that avalanching from all sides has continued to dominate. For the 90° and 45° deflectors, however, the upstream and lateral slopes have continued to increase, though only moderately for the 45° case. Therefore, it is likely that vertical bed degradation continued to dominate in these cases until equilibrium depths were reached.

In summary, it appears that downwelling is the dominant process involved throughout the scouring process, as evidenced by increases in upstream and lateral slopes for almost all time periods examined. However, avalanching appears to have also contributed to scour hole development, primarily for the later phases of the 90° and 135° scour holes. These findings are summarized below (Table 6-6).

Table 6-6: Dominant processes involved in scouring during different phases of scour hole development.

Time (min)	Upstream Slope			Lateral Slope		
	45°	90°	135°	45°	90°	135°
0 - 5	downwelling	downwelling	downwelling	downwelling	downwelling	downwelling
5 - 30	downwelling	downwelling	downwelling	downwelling	downwelling	downwelling
30 - 120	downwelling	avalanching	avalanching	downwelling	avalanching	downwelling
120 - *eq'm*	downwelling	downwelling	avalanching	downwelling	downwelling	avalanching

6.3 DISCUSSION

6.3.1 Equilibrium Scour Hole Geometry

Given that the equilibrium scour depths for the timeline runs followed the trends outlined in Biron *et al.* (2004a), readers are directed to that article for a comparison of measured equilibrium scour hole depths against various predictive models. The discussion in the following section will instead concentrate on scour hole geometry, the temporal development of scour depth, and the relation of scour hole patterns to flow dynamics.

The tendency in the literature to focus on scour depths more than scour hole geometry leaves little room for comparison with our laboratory data. Of the few studies that have reported on scour hole shape, Kuhnle *et al.* (2002) examined equilibrium scour hole geometry around spur dikes angled at 45°, 90°, and 135°. Relative to the dike-bank junction, they found that both the width and downstream extent of the scour hole was greatest for the 45° and 135° obstructions. While our downstream extent was also greatest for the 45° deflectors, it was the least so for the 135° deflectors. Moreover, the width of the scour holes in the present study appears to be in contrast with their findings; our study showed that scour widths were, in fact, the narrowest for the 45° runs.

Such differences may be due to the shape of the obstructions used in the respective experiments. Molinas and Hafez (2000) stated that obstruction length along the flow direction has flow-straightening effects, which would lead to a narrower separation zone (F_w). Following the conceptual model outlined in the previous section, separation zone width is related to scour zone width. As the 45° and 135° dikes used in Kuhnle *et al.* (2002) had relatively sharp corners compared to the 90° dikes, it is possible that the reduction in lateral scour extent for the 90° obstruction was directly a function of the flow straightening effects due to the longer portion of a downstream-oriented wall. Because the deflectors used in our study were only 1.2cm in thickness, and each had a reasonably sharp leading corner, modifications to the separation zone would have been minimized.

Moreover, the spur dikes in Kuhnle *et al.* (2002) were side-sloped while our deflectors were vertical plates. Rahman and Haque (2004) showed that sloped obstructions cause less scour than vertically oriented obstructions. It is likely, then, that the pressure gradient along the upstream face of the 90° dikes in Kuhnle *et al.* (2002) would have been much less than for the vertically oriented deflectors in our study. Because vortex strength is ultimately a function of the vertical stagnation pressure gradient along the upstream face of an obstruction (Ali and Karim, 2002), and scour depth is a function of vortex strength (Mia and Nago, 2003), reduced vorticity around the vertically angled spur dikes would have resulted in less scour occurring for their 90° case. If the conceptual model in Section 6.2.3 is correct – and scour around 90° obstructions has a stronger relation to vortex strength than scour around angled obstructions – it is possible that the notion of reduced scour extents around the 90° dikes was a result of reduced vorticity.

Another point of contention between published reports and our findings pertains to the upstream slope of the scour hole, with no consensus yet having been reached on what an appropriate value should be for the equilibrium scour hole. Blaisdell (1996) and Lim (1997) claim that the slope should vary between 22° and 26°, Mia and Nago (2003) cite a value of 30°, and Graf and Istiarto (2002) reported a value of 35°. Our findings indicate that not only can the upstream angle of the equilibrium hole reach the upper limits (i.e. 35°) set by Graf and Istiarto (2002) (Figure 6-6), but that it appears to be dependent on the angle of the obstruction orientation.

Although it was not discussed explicitly, scour hole slopes for Kuhnle *et al.* (2002) can be estimated from their figure illustrating bed elevation contours (Figure 6-11). Following the dashed-line transects, the slopes were approximated as being 34°, 28°, and 30° for the 135°, 90°, and 45° dikes, respectively. These values are comparable to our findings for the 135° and 45° deflectors, which exhibited upstream slopes of 33° and 31°, respectively. However, we found that the scour slopes were steepest for the 90° deflectors (~37°), while Kuhnle *et al.* (2002) show that it is the least so for the 90° dikes. It must be noted that Kuhnle *et al.* (2002) also reported the lowest scour depths for the 90° dikes, so it is logical that reduced slopes would follow.

Figure 6-11: Scour hole geometry around angled spur dikes (from Kuhnle *et al.*, 2002). Red dashed lines (A-A') indicate transects used to estimate slopes. Contour interval is approximately 2cm.

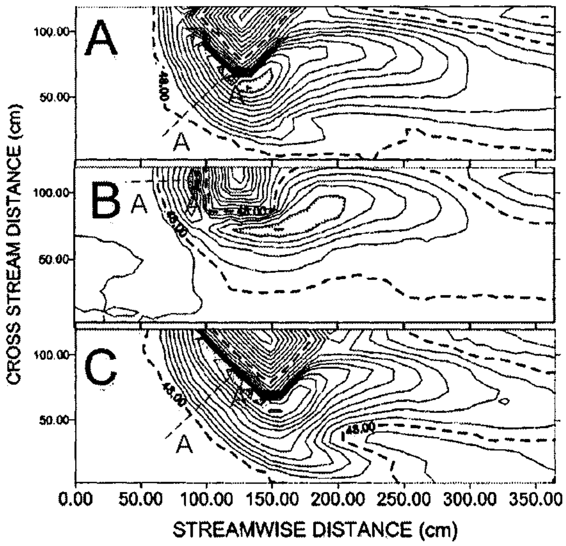

6.3.2 *Temporal Development of Scour Holes*

Depth vs. Time

Most of the attention in the literature on scour hole development is focused on bridge piers, while obstructions such as dikes, abutments, and deflectors have not been studied as much (Kothyari and Ranga Raju, 2001). Such a statement is evidenced by reviewing the equations tested in Section 6.1.3. Of the six equations examined, only two – Cardoso and Bettess (1999), and Oliveto and Hager (2002) – were developed using data from scour around abutments, and none was done so exclusively. Ironically, one of these two – Oliveto and Hager (2002) – was among the worst at accurately predicting scour depths over time for the deflectors.

Cardoso and Bettess (1999) suggest that – although agreement was shown between their data and the equations of Ettema (1980; "*ET*"), Franzetti *et al.* (1982; "*FR*"), and Whitehouse (1997; "*WH*") – the *ET*, *FR*, and *WH* equations should not be applied to abutments until "the functions relating [the constants] K_1, K_2, a_1, a_2, and p with some set of non-dimensional parameters are known" (p. 396). Our data support the notion that both the Ettema (1980) and Franzetti *et al.* (1982) equations are dependent on obstruction angle. Figure 6-4 suggests that only minor modifications need to be made to the Ettema (1980) equation, as the trendlines for the three deflector angles nearly collapse into a single line when using average values of K_1 and K_2. The Franzetti *et al.* (1982) equation, however, illustrates even stronger angle dependence, with the three trends remaining distinct. Additionally, Table 6-4 reveals that the relationship between the Franzetti *et al.* (1982) predictions and our scour depth measurements was not even linear, suggesting that further attention is required to refine the constants a_1 and a_2.

Moreover, it is interesting to note that the Whitehouse (1997) equation provided better predictions of our data than did the Cardoso and Bettess (1999) model. Given that the latter is simply the former with the addition of a constant (1.025), our data suggest that the constant, in fact, should have a value less than one. Table 6-4 shows that the regression slope (a) between model *WH* predictions and our data is closer to unity than that for model *CB* predictions, and thus it appears that the modifier in the Cardoso and Bettess (1999) equation is too large in magnitude. Therefore, it is likely that the sensitivity of p in the Whitehouse (1997) equation be further reviewed with relation to obstruction parameters.

That the various equations best predicted measured scour depths at various times of scour hole development reflects the Cardoso and Bettess (1999) statement that scouring takes place in three phases: initial, principal, and equilibrium. As stated in Section 6.1.3, different models performed better at predicting scour depths for different stages.

For example, each of the four equations that produced r^2 values greater than 0.95 when regressed against our measurements strongly overpredicted scour depths for the initial phase of the 45° run, while no apparent overpredictions were evident for the 90° and 135° runs. Thus, there are two possible conclusions that can be drawn: (i) the equations are satisfactory at predicting scour depths during the initial phase for 90° and 135° obstructions, but not for 45° obstructions, or; (ii) the initial phase of scour development for 90° and 135° deflectors takes place within the first five minutes. The latter is possible because no topography measurements were taken within the first five minutes of run time

For the principal phase, the Cardodso and Bettess (1999), Whitehouse (1997), and Ettema (1980) models were better at predicting scour depths than was the Melville and Chiew (1999) equation. Of the many parameters that the Melville and Chiew (1999) model is dependent upon, the sensitivity of U/U_c should be reviewed. Figure 6-12 illustrates a plot of scour data from the present study atop the envelope curves presented by Melville and Chiew (1999). As can be seen, measured depths are plotting in the range of $0.5 < U/U_c < 0.6$, which is slightly above the U/U_c value used in the timeline runs (0.47). It is possible that such a discrepancy could be responsible for the underpredictions during the intermediate stage of the scouring process in Figure 6-4. Therefore, we suggest that the envelope curves – which were developed for piers – be modified slightly for the equation to be applied to abutments and deflectors.

Figure 6-12: Scour depth (d_s) over time (t), normalized by respective equilibrium values (d_{se}, t_e) for present study plotted on Melville and Chiew (1999) envelope curves of approach velocity (V) normalized by critical velocity (V_c).

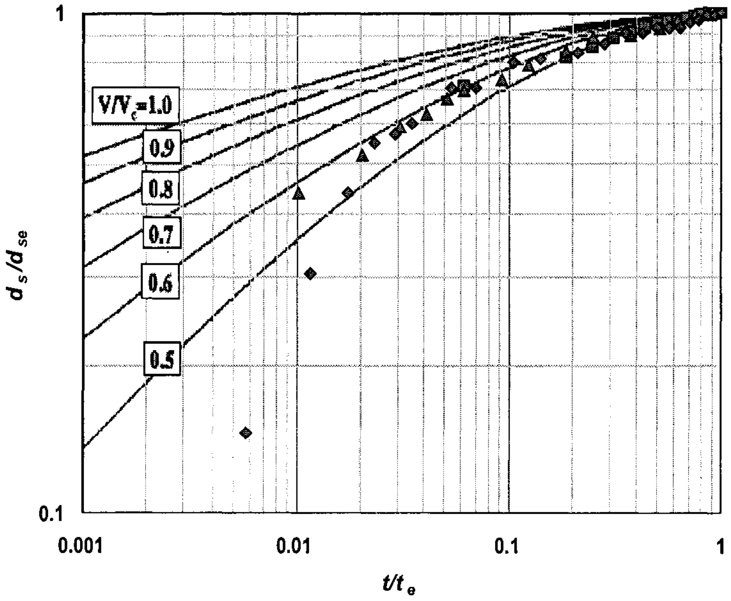

Geometry vs. Time

As stated previously, most of the literature concerning scour focuses exclusively on scour hole *depth* over time. Therefore, only general comparisons of our scour hole geometry over time can be made with other accounts. Kwan (1988), as reported in Kothyari and Ranga Raju (1998), stated that the width of local scouring near bridge piers affected a region 0.1 to 0.5 times the length of the abutment projected laterally from the nose. Such values correspond reasonably well with the 45° and 135° deflectors – where scour widths at the nose of the deflectors were approximately 0.2 and 0.6 times the deflector length – but were much lower than our scour extent for the 90° deflector, where scour widths were 0.8 times the deflector length.

However, Kwan (1988) also reported that the width of the scour hole remained constant throughout its entire development. Clearly, our data have shown that this is not the case for deflectors, with the 45°, 90°, and 135° scour holes growing in width by an average of 240% between t = 5min and equilibrium.

Figure 6-7 shows that the scour hole progressively envelopes the regions exhibiting the highest flow curvature. Given that Molinas (1998) showed that there is extra shear amplification in regions of great curvature, it is likely that even though the velocity magnitudes in this region were not as great as in the acceleration zone in the center of the channel, the additional curvature may have amplified the ambient shear stress and contributed to sediment evacuation.

Finally, no published reports on scour hole slope variation over time could be found. Brief mention to the subject is made by Dey *et al.* (1995), who state that the dynamic angle of repose throughout scour hole growth can be up to 20° greater than the static angle of repose of the sediment. Such a notion could potentially explain how our 135° scour hole exhibited slopes as high as 40° in the earlier stages of development before reaching equilibrium values of approximately 33°.

6.3.3 Relationship between Flow Field Properties and Scour Hole Geometry

The laboratory tests showed that scour around deflectors begins at the nose of the obstruction – similar to bridge piers and abutments (Mostafa, 1994; Ettema *et al.*, 1998) – as this was the location of maximum velocity amplification. That the approach velocity was doubled at this location (Figure 5-4b) likely means that shear stress could have increased by up to four times – as shear stress is proportional to the square of velocity – which would be in line with previous estimates (e.g. Molinas, 1998; Ahmed and Rajaratnam, 2000). However, given that no formal shear stress calculations were made during this study, this is a first estimate at best. For a more detailed examination of shear stress amplification near deflectors, refer to Biron *et al.* (2004b).

Figure 6-7 provided further support to the notion that the main mechanism behind scour is vortex formation and the associated downflow (Kothyari and Ranga Raju, 2001). The use of downwelling as an indicator of scour depths is reasonable following two separate lines of thought. First, Lane *et al.* (1999) stated that downwelling acts as an additional transfer of momentum to the bed. Therefore, even if velocity magnitudes downstream of the deflector nose may not have exceeded "critical" levels, it is possible that the shear stress amplification due to the momentum transfer could have been enough to induce sediment movement.

Moreover, the notion of sediment divergence could also play a role. Because sediment was not in suspension near the deflectors, any flow vertically directed towards the bed could not have been carrying a sediment load. Because vertical convergence of flow requires a horizontal divergence at the bed, in turn there must be a resulting divergence of the shear stress field parallel to the bed. Divergence of shear stress, then, results in a divergence of the sediment transport flux in order to preserve fluid mass continuity at the bed.

No evidence could be found in the literature on upstream separation length (F_s) acting as an indicator of the upstream extent of the scour hole. Biron *et al.* (2004a), however, showed that the upstream extent of the scour holes (S_{u-b}) for 45°, 90°, and 135° deflectors of contraction ration 0.5 were approximately 7, 15, and 26cm. Given that Figure 5-7a shows non-dimensional flow separation distance (F_s) becomes constant at values of 0.7, 1.65, and 2.7 for the three deflector angles, respectively, the deflector lengths of 10cm used by Biron *et al.* (2004a) would translate into F_s distances of 7, 16.5, and 27cm, showing a very close relation between F_s and S_{u-b}.

Figure 6-13: Lateral extent of scour hole matching flow lines with no appreciable curvature from (a) Kwan (1984), reproduced in Lim (1997), and (b) Cardoso and Bettess (1999).

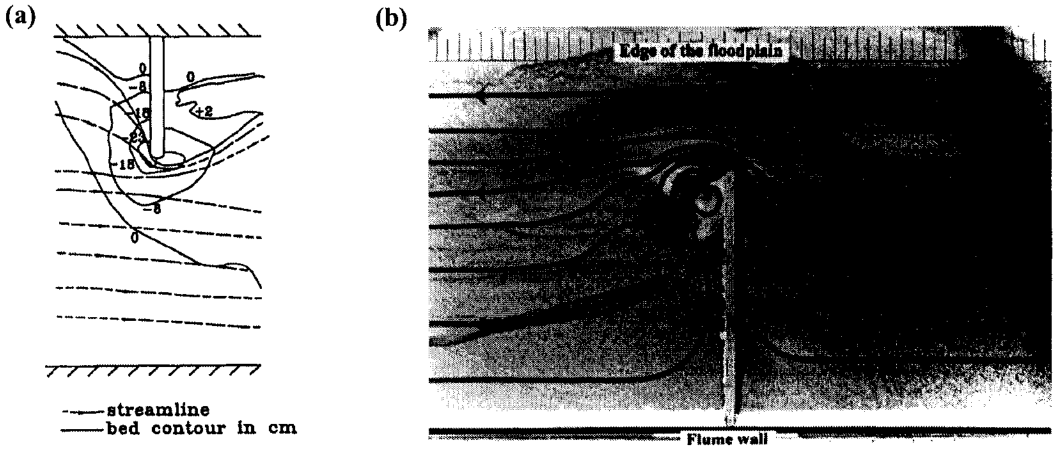

Only anecdotal evidence is available to relate scour hole widths to flow separation width. Kwan (1984) illustrated that scour hole widths roughly matched the lateral extent of the flow curvature region (Figure 6-13a), though he did not expresslystate so. Additionally, Cardoso and Bettess (1999; Figure 6-13b) appear to show that streamlines at the lateral boundary of the scour hole are not appreciably curved, but this is based on inference from the figure provided in the article. No specific mention was made stating that the scour hole extent was determined by a lack of flow curvature. Therefore, it is recommended that future studies also test the hypothesis that the lateral extent of the scour hole is determined by flow separation width.

Using a semi-circle to estimate the shape of the scour hole around deflectors (Figure 6-8; "L9") can be justified by examining the shape of scour holes around piers taking into consideration the differences between flow patterns around piers and abutments. Specifically, scour holes around cylindrical bridge piers are generally circular in shape, concentric with the pier (Dey *et al.*, 1995). Meanwhile, bridge abutments "with the mirror image in the channel wall were considered by earlier investigators to be similar to the pier of equivalent shape" (Kothyari and Ranga Raju, 2001). This means that the side of an abutment away from the wall is roughly equivalent to one half of a bridge pier. Therefore, if scour holes around piers are circular, and abutments – or, in this case, deflectors – are considered half-piers, it is sensible that the portion of the scour hole around deflectors not subject to wall effects would be semi-circular in shape.

Finally, that no scouring took place downstream of P_{loc} can be explained through general fluvial geomorphology principles. Because the dynamic pressure distribution was related to water surface topography (Figure 5-8b), the location of P_{loc} represents a local minimum in flow depth. In addition, P_{loc} served as a point of inflection for the slope of the water surface, meaning that the water surface was negatively sloped between the deflector and P_{loc} and positively sloped downstream of it. As changes in water surface slope from negative to positive have been related to sediment deposition (Knighton, 1998), it can be concluded that P_{loc} was not necessarily a limit to scouring, but rather that it represented the beginning of the deposition zone.

6.3.4 Implications on Stream Deflector Design

Although many strides have been made in the present study relating flow patterns to scouring around deflectors, the immediate applicability to field situations remains limited for a number of reasons. First, because this study was performed in a laboratory, the consequent scaling issues (Ettema *et al.*, 1998a; Ettema and Muste, 2004) may remain problematic. Moreover, only steady flow conditions were tested. Because discharge in natural channels are typically unsteady during floods (Knighton, 1996), the effect of varying discharge rates must be considered. In addition, natural sediment mixtures tend to be non-uniform, and thus scour holes will be reduced in depth due to bed-armoring processes (Froehlich, 1995). Finally, if live-bed scouring conditions (i.e. approach velocity is greater than critical) exist during the large discharge events, the equilibrium scour depths would be reduced (Lim and Cheng, 1998)

Furthermore, deflectors in the field are often designed to be frequently overtopped (Dolinsek and Biron, 2001; Thompson, 2002; Biron *et al.*, 2004a). Theoretically, a reduction in obstruction height would have several implications for the flow field and resulting scour patterns. For example, lower deflectors would mean that some of the discharge upstream of the obstruction would not be intercepted. Because the stagnation pressure gradient on the front of the obstruction is a function of flow deceleration (Ali and Karim, 2002), and the flow at the surface must decelerate the most when the height of the obstruction is greater than the flow depth (Ahmed and Rajaratnam, 1998), reduced obstruction heights would likely result in a weaker pressure gradient being formed. As scouring is a function of vortex strength, which in turn is a function of the pressure gradient, reduced scour depths and extents would likely occur.

Allowing part of the flow to go over the obstruction would likely also result in weaker velocity amplification at the nose, as part of the discharge would not be subject to constriction. Because shear stress at the obstruction nose is a function of the velocity amplification (Molinas, 1998), reduced velocities would result in lower shear stresses, and ultimately lesser scour depths.

Additionally, the extents of the upstream and lateral separation zones would likely be reduced as well. If portions of the discharge are not obstructed, the water surface superelevation upstream of the deflectors would likely be reduced. Because Section 5.2 has linked upstream dynamic pressures (i.e. water surface elevations) with the upstream and lateral extents of the separation zones, and Section 6.2 has linked separation zone extents with scour extents, it is likely that the scouring around overtopped deflectors would be reduced.

Finally, it is likely that the methods and principles derived in the preceding chapter are applicable to other instream obstructions similar in shape, such as weirs, spur dikes, or abutments. However, the applicability to circular bridge piers is questionable. Given the fundamental differences in the flow fields around abutments and piers (Kothyari and Ranga Raju, 2001), it is unknown at this time if scour hole patterns will follow similar trends based on flow field parameters. Therefore, it is recommended that a future study reproduce the present experiment substituting circular piers for stream deflectors.

7. CONCLUSION

This thesis has achieved its three stated objectives, and in the process made a number of contributions to the body of work involving the numerical modeling of flow dynamics around instream obstructions and the examination of local scour processes. The results of the mesh sensitivity analysis (Section 4.1) illustrated that the conventional means of using maximum and minimum flow parameters as proxies for a fully-developed flow field may be inadequate, especially when individual mesh cells are partially obstructed. It is thus recommended that more thorough grid-independence tests be carried out following Hardy *et al.* (2003).

Additionally, a new method of incorporating complex bed topography into a structured Cartesian modeling mesh was developed (Section 4.2). Although the initial tests were not as successful as those using conventional means of representing boundary geometry in a modeling domain, the 'object bed' did show signs of potential. It is recommended that future studies using the object bed obtain and incorporate the highest resolution topography data possible.

Chapter 5 provided a systematic examination of how deflector angle and length impact the three-dimensional flow field. Dynamic pressures (i.e. water surface topography), nose velocity amplification, length and width of the separation zone, magnitudes and extent of negative vertical velocity, and primary vortex formation were shown to be dependent on obstruction geometry. Future studies could combine these findings with varying discharge to provide an even greater understanding of the flow-obstruction interaction.

The laboratory component of the thesis provided new insight into scour hole temporal development. To our knowledge, Section 6.1 is the first thorough examination of the dependence of planform scour hole geometry development on obstruction angle. The topography data from Figure 6-2 could be used either as verification data of a numerical model predicting bed development, or to build individual modeling meshes to simulate the flow field at various times throughout scour hole development. Such simulations would provide invaluable insight into how the flow field evolves as the bed is adjusting to the presence of the obstruction, thereby contributing to a better understanding of the flow-bed feedback cycle.

Moreover, Equation 6-1 closely predicted maximum scour hole depths during development, and was shown to be independent of obstruction angle and comparable with various equations from throughout the literature. However, future studies involving varying discharge and obstruction length are needed to establish the equation's transferability.

Examination of three-dimensional scour hole geometry evolution provided evidence that scouring may be dominated by different processes throughout development, and that such processes depend on the angle of the obstruction. However, only a theoretical model was presented. Future work should isolate primary vortex formation and development and establish its dependence on obstruction angle.

Finally, a method was developed to predict scour hole extents based only on flow field properties over a flat, initial bed. However, future studies must be performed to establish if the method is applicable when flow conditions (i.e. depths, velocities, discharge, etc..) other than those tested in this study are present.

On a broader scale, we hope to have shown that it is possible to combine data from numerical and laboratory sources to provide meaningful results, calling upon the strengths of each to suppress the shortcomings of the other. Specifically, velocity point measurements, alone, may not have represented the full flow structure in the laboratory (Ferguson *et al.*, 2003), but the application of poorly-understood flow-sediment interaction relationships into a numerical model could have resulted in a misinterpretation of bed response (Cao and Carling, 2002).

In closing, there seems to be a stark dichotomy between those who use numerical models and 'classical' researchers. For some, models represent a powerful and promising tool with which to examine a given system; for others, they are nothing more than hand-waving and flashy jargon. As Aber (1997) eloquently stated: "When the question is asked, as it usually is, 'Are you a modeler or a field scientist?', there are few who would respond, 'Both.'" We purport that there should be no distinguishing the two, provided that physical principles are at the forefront of the interpretation of *any* results, be they physical or digital.

8. REFERENCES

Aber, J.D. 1997. Why don't we believe the models? Bulletin of the Ecological Society of America, 78(3): 232-233.

Ahmed, F. and Rajaratnam, N., 1998. Flow around bridge piers. Journal of Hydraulic Engineering, ASCE, 124(3): 288-300.

Ali, K.H.M. and Karim, O., 2002. Simulation of flow around piers. Journal of Hydraulic Research, 40(2): 161-174.

Anderson, P.G. 1998. Sediment generation from forestry operation and associated effects on aquatic ecosystems. *In* M.K. Brewin and D.M.A Monita (tech.coords). Forest-fish conference: land management practices affecting aquatic ecosystems. Proc. Forest-Fish Conference, May 1-4, 1996, Calgary, Alberta. Nat. Resour. Can., Can. For. Serv., North. For. Cent., Edmonton, Alberta. Inf. Rep. NOR-X-356

Angermeier, P.L., 1995. Ecological attributes of extinction-prone species: loss of freshwater fishes of Virginia. Conservation Biology, 9(1): 143-158.

Babaeyan-Koopaei, K., Ervine, D.A., Carling, P.A. and Cao, Z., 2002. Velocity and turbulence measurements for two overbank flow events in River Severn. Journal of Hydraulic Engineering, ASCE, 128(10): 891-900.

Bates, P.D., Lane, S.N. and Ferguson, R.I., in press. CFD Applications in Hydrology and Hydraulics: Theory and Practice. Wiley.

Berg, N., Carlson, A. and Azuma, D., 1998. Function and dynamics of woody debris in stream reaches in the central Sierra Nevada, California. Canadian Journal of Fisheries & Aquatic Sciences, 55: 1807-1820.

Biglari, B. and Sturm, T.W., 1998. Numerical modeling of flow around bridge abutments in compound channel. Journal of Hydraulic Engineering, ASCE, 124(2): 156-164.

Binns, N.A., 1994. Long-term responses of trout and microhabitats to habitat management in a Wyoming headwater stream. North American Journal of Fisheries Management, 14: 87-98.

Biron, P.M., Lane, S.N., Roy, A.G., Bradbrook, K.F. and Richards, K.S., 1998. Sensitivity of bed shear stress estimated from vertical velocity profiles: the problem of sampling resolution. Earth Surface Processes and Landforms, 23: 133-139.

Biron, P.M., Richer, A., Kirkbride, A.D., Roy, A.G. and Han, S., 2002. Spatial patterns of water surface topography at a river confluence. Earth Surface Processes and Landforms, 27: 913-928.

Biron, P.M., Robson, C., Lapointe, M.F. and Gaskin, S.J., *in press*. Three-dimensional flow dynamics around deflectors. River Research and Applications.

Biron, P.M., Robson, C., Lapointe, M.F. and Gaskin, S.J., 2004a. Deflector designs for fish habitat restoration. Environmental Management, 33(1): 25-35.

Biron, P.M., Robson, C., Lapointe, M.F. and Gaskin, S.J., 2004b. Comparing different methods of bed shear stress estimates in simple and complex flow fields. Earth Surface Processes and Landforms, 29(11): 1403-1415.

Biron, P.M., Ramamurthy, A.S., and Han, S. 2004c. Three-dimensional numerical modeling of mixing at river confluences. Journal of Hydraulic Engineering, ASCE, 130(3): 243-253.

Blaisdell, F.W., 1996. Discussion: Local scour downstream of hydraulic structures. 1997, 123(7): 419-420.

Booker, D.J., Sear, D.A. and Payne, A.J., 2001. Modelling three-dimensional flow structures and patterns of boundary shear stress in a natural pool-riffle sequence. Earth Surface Processes and Landforms, 26: 553-576.

Bradbrook, K.F., Biron, P.M., Lane, S.N., Richards, K.S. and Roy, A.G., 1998. Investigation of controls on secondary circulation in a simple confluence geometry using a three-dimensional numerical model. Hydrological Processes, 12: 1371-1396.

Bradbrook, K.F., Lane, S.N. and Richards, K.S., 2000a. Numerical simulation of time-averaged flow structure at river channel confluences. Water Resources Research, 36: 2731-2746.

Bradbrook, K.F., Lane, S.N., Richards, K.S., Biron, P.M., and Roy, A.G. 2000b. Large eddy simulation of periodic flow characteristics at river channel confluences. Journal of Hydraulic Research, 38: 207-215.

Bradbrook, K.F., Lane, S.N., Biron, P.M. and Roy, A.G., 2001. Role of bed discordance at asymmetrical river confluences. Journal of Hydraulic Engineering, ASCE, 127(5): 351-368.

Bradbrook, K.F., 2000. Three-dimensional numerical modeling of flow dynamics at river confluences. PhD Thesis, Cambridge University.

Brookes, A. and Shields-Jr., F.D., 1996. Perspectives on river channel restoration. In: A. Brookes and F.D. Shields-Jr. (Editors), River channel restoration: Guiding principles for sustainable projects. John Wiley and Sons, New York, pp. 1-19.

Cao, Z. and Carling, P.A., 2002. Mathematical modelling of alluvial rivers: reality and myth. Part I: General review. Water & Maritime Engineering, 154(3): 207-219.

Cardoso, A.H. and Bettess, R., 1999. Effects of time and channel geometry on scour at bridge abutments. Journal of Hydraulic Engineering, ASCE, 125(4): 388-399.

Chiew, Y.-M. and Lim, S.-Y., 1996. Local scour by a deeply submerged horizontal circular jet. Journal of Hydraulic Engineering, ASCE, 122(9): 529-532.

Chrisohoides, A., Sotiropoulos, F. and Sturm, T.W., 2003. Coherent structures in flat-bed abutment flow: Computational fluid dynamics simulations and experiments. Journal of Hydraulic Engineering, ASCE, 129(3): 177-186.

D'Agostino, V. and Ferro, V., 2004. Scour on alluvial bed downstream of grade-control structures. Journal of Hydraulic Engineering, ASCE, 1(30): 24-37.

D'Aoust, S.G. and Millar, R.G. 2000. Stability of ballasted woody debris habitat structures. Journal of Hydraulic Engineering, ASCE, 126(11): 810-817.

Dey, S., Bose, S.K. and Sastry, G.L.N., 1995. Clear water scour at circular piers: A model. Journal of Hydraulic Engineering, ASCE, 121(12): 869-876.

Dolinsek, I. and Biron, P.M., 2001. The role of flow deflectors on maintaining pool depth and habitat in a large river, NESTVAL Annual Conference, New Bedford, MA, USA.

Ebersole, J.L., Liss, W.J. and Frissel, C.A., 1997. Restoration of stream habitats in the Western United States: restoration as reexpression of habitat capacity. Environmental Management, 21(1): 1-14.

Ettema, R., 1980. Scour at bridge piers, University of Auckland, Auckland, New Zealand.

Ettema, R., Melville, B.W. and Barkdoll, B., 1998a. Scale effect in pier-scour experiments. Journal of Hydraulic Engineering, ASCE, 124(6): 639-642.

Ettema, R., Mostafa, E.A., Melville, B.W. and Yassin, A.A., 1998b. Local scour at skewed piers. Journal of Hydraulic Engineering, ASCE, 124(7): 756-759.

Ettema, R. and Muste, M., 2004. Scale effects in flume experiments on flow around a spur dike in flatbed channel. Journal of Hydraulic Engineering (ASCE), 130(7): 635-646.

Fang, F.-M., Hsieh, W.D., Jong, S.W. and She, J.J., 1997. Unsteady turbulent flow past solid fence. Journal of Hydraulic Engineering, ASCE, 123(6): 560-565.

Ferguson, R.I., Parsons, D.R., Lane, S.N. and Hardy, R.J., 2003. Flow in meander bends with recirculation at the inner bank. Water Resources Research, 39(11): 1322-1334.

Franzetti, S., Larcan, E. and Mignosa, P., 1982. Influence of tests duration on the evaluation of ultimate scour around circular piers. In: B.F. Engineering (Editor), International Conference on the Hydraulic Modelling of Civil Engineering Structures, Cranfield, Bedford, MK43 OAJ, England, pp. 381-396.

Frissell, C.A. and Nawa, R.K., 1992. Incidence and causes of physical failure of artificial habitat structures in streams of Western Oregon and Washington. North American Journal of Fisheries Management, 12: 182-197.

Froehlich, D.C., 1995. Armor-limited clear-water contraction scour at bridge piers. Journal of Hydraulic Engineering, ASCE, 121(6): 490-493.

FISRWG, 1998. Stream corridor restoration: Principles, processes, and practices. GPO Item No. 0120-A; SuDocs No. A 57.6/2:EN 3/PT.653, Federal Interagency Stream Restoration Working Group (FISRWG).

Garbrecht, J., Kuhnle, R. and Alonso, C., 1995. A sediment transport capacity formulation for application to large channel networks. Journal of Soil and Water Conservation, 50(5): 527-529.

Gilvear, D.J., 1999. Fluvial geomorphology and river engineering: future roles utilizing a fluvial hydrosystems framework. Geomorphology, 31(1-4): 229-245.

Gore, J.A. and Hamilton, S.W., 1996. Comparison of flow-related habitat evaluations downstream of low-head weirs on small and large fluvial ecosystems. Regulated Rivers: Research and Management, 12(4-5): 459-469.

Gowan, C. and Fausch, K.D., 1996. Long-term demographic responses of trout populations to habitat manipulation in six Colorado streams. Ecological Applications, 6(3): 931-946.

Graf, W.H. and Istiarto, I., 2002. Flow pattern in the scour hole around a cylinder. Journal of Hydraulic Research, 40(1): 13-20.

Hager, W.H. and Oliveto, G., 2002. Shields' entrainment criterion in bridge hydraulics. Journal of Hydraulic Engineering, ASCE, 128(5): 538-542.

Haltigin, T.W., Biron, P.M., and Lapointe, M.F. 2004. The effect of obstruction angle and length on a three-dimensional numerically modeled flow field. Unpublished manuscript.

Han, S. 2002. Three dimensional numerical modeling of mixing at river confluences. Unpublished MASc thesis, Concordia University, 151p.

Hardy, R.J., Bates, P.D. and Anderson, M.G., 1999. The importance of spatial resolution in hydraulic models for floodplain environments. Journal of Hydrology, 216: 124-136.

Hardy, R.J., Lane, S.N., Ferguson, R.I. and Parsons, D.R., 2003. Assessing the credibility of a Computational Fluid Dynamic code for open channel flows. Hydrological Processes, 17: 1539-60.

Haschenburger, J.K., 1999. A probability model of scour and fill depths in gravel-bed channels. Water Resources Research, 35(9): 2857-2869.

Heggenes, J., 1996. Habitat selection by brown trout (Salmo trutta) and young Atlantic salmon in streams: Static and dynamic hydraulic modeling. Regulated Rivers, 12(2-3): 155-169.

Hey, R.D., 1994. Restoration of gravel-bed rivers: principles and practice. In: D. Shrubsole (Editor), 1st International Conference on Guidelines for "Natural" Channel Systems, Niagara Falls.

Hey, R.D., 1996. Environmentally sensitive river engineering. In: G. Petts and P. Calow (Editors), River Restoration. Blackwell Science, Oxford, pp. 80-105.

Hicks, B.J. and Hall, J.D., 2003. Rock type and channel gradient structure salmonid populations in the Oregon Coast Range. Transactions of the American Fisheries Society, 132: 468-482.

Hilderbrand, R.H., Lemly, A.D., Dolloff, C.A. and Harpster, K.L., 1997a. Effects of large woody debris placement on stream channels and benthic macroinvertebrates. Canadian Journal of Fisheries and Aquatic Sciences, 54: 931-939.

Hodskinson, A. and Ferguson, R.I., 1998. Numerical modelling of separated flows in river bends: Model testing and experimental investigation of geometric controls on the extent of separation at the concave bank. Hydrological Processes, 12: 1323-1338.

Hoey, T.B. and Ferguson, R., 1994. Numerical simulation of downstream fining by selective transport in gravel-bed rivers: Model development and illustration. Water Resources Research, 30(7): 2251-2260.

Hoffmans, G.J.C.M. and Pilarczyk, K.W., 1996. Closure: Local scour downstream of hydraulic structures. 1997, 123(7): 420.

Holmlund, C.M. and Hammer, M., 1999. Ecosystem services generated by fish populations. Ecological Economics, 29(2): 253-268.

Hunt, R.L., 1988. A compendium of 45 trout stream habitat development evaluations in Wisconsin during 1953-1985. 162, Wisconsin Department of Natural Resources.

Huusko, A. and Yrjana, T., 1997. Effects of instream enhancement structures on brown trout, *Salmo trutta* L., habitat availability in a channelized boreal river: a PHABISM approach. Fisheries Management and Ecology, 4: 453-466.

Hvidsten, N.A. and Johnsen, B.O., 1992. River bed construction: impact and habitat restoration for juvenile Atlantic salmon, *Salmo salar* L., and brown trout, *Salmo trutta* L. Aquaculture and Fisheries Management, 23: 489-498.

Johnson, P.A., 1995. Comparison of pier-scour equations using field data. Journal of Hydraulic Engineering, ASCE, 121(8): 626-629.

Johnson, P.A., 1996. Modeling uncertainty in prediction of pier scour. Journal of Hydraulic Engineering, ASCE, 122(2): 66-72.

Johnson, P.A. and Dock, D.A., 1998. Probablistic bridge scour estimates. Journal of Hydraulic Engineering, ASCE, 124(7): 750-754.

Johnson, P.A. and Simon, A., 1997. Effect of channel adjustment processes on reliability of bridge foundations. Journal of Hydraulic Engineering, ASCE, 123(7): 648-651.

Johnson, P.A. and McCuen, R.H., 1991. A temporal spatial pier scour model. Transportation Research Record, 1319: 143-149.

Karim, O.A. and Ali, K.H.M., 2000. Prediction of flow patterns in local scour holes cause by turbulent water jets. Journal of Hydraulic Research, 38(4): 279-288.

Kim, S.C., Fredrichs, C.T., Maa, J.P.Y. and Wright, L.D., 2000. Estimating bottom stress in a tidal boundary layer from Acoustic Doppler Velocimeter data. Journal of Hydraulic Engineering, ASCE, 126(6): 399-406.

Knighton, A.D. 1998. Fluvial Forms and Processes: A New Perspective. Arnold, London, 383pp.

Kondolf, G.M., 1998. Lessons learned from river restoration projects in California. Aquatic Conservation: Marine and Freshwater Ecosystems, 8: 39-52.

Kondolf, G.M. and Micheli, E.R., 1995. Evaluating stream restoration projects. Environmental Management, 19(1): 1-15.

Kondolf, G.M., Kattelmann, R., Embury, M. and Erman, D.C., 1996. Status of riparian, Sierra Nevada Ecosystem Project: Final report to Congress, vol. II, Assessments and scientific basis for management options. Wildland Resources Center Report no. 37. Univeristy of California, Centers for Water and Wildland Resources, Davis, CA, pp. 1009-1030.

Kothyari, U.C. and Raju, K.G.R., 2002. Scour around spur dikes and bridge abutments. Journal of Hydraulic Research, 39(4): 367-374.

Kuhnle, R.A., Alonso, C.V. and ShieldsJr., F.D., 1999. Geometry of scour holes associated with 90° spur dikes. Journal of Hydraulic Engineering, ASCE, 125(9): 972-978.

Kuhnle, R.A., Alonso, C.V. and ShieldsJr., F.D., 2002. Local scour associated with angled spur dikes. Journal of Hydraulic Engineering, ASCE, 128(12): 1087-1093.

Kumar, V., Raju, K.G.R. and Vittal, N., 1999. Reduction of local scour around bridge piers using slots and collars. Journal of Hydraulic Engineering, ASCE, 125(12): 1302-1305.

Kwan, T.F. 1984. Study of abutment scour. Report No. 328, School of Engineering, University of Auckland, New Zealand.

Kwan, T.F. 1984. A study of abutment scour. Report No. 451, School of Engineering, University of Auckland, New Zealand.

Lammert, M. and Allan, J.D., 1999. Assessing biotic integrity of streams: effects of scale in measuring the influence of land use/cover and habitat structure on fish and macroinvertebrates. Environmental Management, 23(2): 257-270.

Lane, S.N., 1998. Hydraulic modelling in hydrology and geomorphology: A review of high resolution approaches. Hydrological Processes, 12: 1131-1150.

Lane, S.N. et al., 1998. Three-dimensional measurement of river channel flow processes using acoustic doppler velocimetry. Earth Surface Processes and Landforms, 23: 1247-1267.

Lane, S.N., Bradbrook, K.F., Richards, K.S., Biron, P.A. and Roy, A.G., 1999. The application of computational fluid dynamics to natural river channels: three-dimensional versus two-dimensional approaches. Geomorphology, 29: 1-20.

Lane, S.N., Hardy, R.J., Elliott, L. and Ingham, D.B., 2002. High-resolution numerical modelling of three-dimensional flows over complex river bed topography. Hydrological Processes, 16: 2261-2272.

Lane, S.N., Hardy, R.J., Elliott, L. and Ingham, D.B., 2004. Numerical modeling of flow processes over gravelly surfaces using structured grids and a numerical porosity treatment. Water Resources Research, 40(1): W01302-W01319.

Lapointe, M.F., Eaton, B., Driscoll, S. and Latulippe, C., 2000. Modeling the probability of salmonid egg pocket scour due to floods. Canadian Journal of Fisheries & Aquatic Sciences, 57: 1120-1130.

Lawless, M. and Robert, A., 2001. Three-dimensional flow structure around small-scale bedforms in a simulated gravel-bed environment. Earth Surface Processes and Landforms, 26: 507-522.

Lim, S.-Y., 1997. Equilibrium clear-water scour around an abutment. Journal of Hydraulic Engineering, ASCE, 123(3): 237-243.

Lim, S.Y. and Cheng, N.S., 1998a. Prediction of live-bed scour at bridge abutments. Journal of Hydraulic Engineering, ASCE, 124(6): 635-638.

Marelius, F. and Sinha, S.K., 1998. Experimental investigation of flow past submerged vanes. Journal of Hydraulic Engineering, ASCE, 124(5): 542-545.

Martinuzzi, R. and Topea, C., 1993. The flow around surface mounted, prismatic obstacles placed in a fully developed channel flow. Journal of Fluids Engineering, 115: 85-92.

Martin-Vide, J.P., Hidalgo, C. and Bateman, A., 1998. Local scour at piled bridge foundations. Journal of Hydraulic Engineering, ASCE, 124(4): 439-444.

McLelland, S.J. and Nicholas, A.P., 2000. A new method for evaluating errors in high-frequency ADV measurements. Hydrological Processes, 14: 351-366.

Melville, B.W., 1992. Local scour at bridge abutments. Journal of Hydraulic Engineering, ASCE, 118(4): 615-630.

Melville, B.W., 1995. Bridge abutment scour in compound channels. Journal of Hydraulic Engineering, ASCE, 121(12): 863-868.

Melville, B.W., 1997. Pier and abutment scour: Integrated approach. Journal of Hydraulic Engineering, ASCE, 123(2): 125-136.

Melville, B.W. and Chiew, Y.-M., 1999. Time scale for local scour at bridge piers. Journal of Hydraulic Engineering, ASCE, 125(1): 59-65.

Melville, B.W. and Hadfield, A.C., 1999. Use of sacrificial piles as pier scour countermeasures. Journal of Hydraulic Engineering, ASCE, 125(11): 1221-1224.

Melville, B.W. and Raudkivi, A.J., 1996. Effects of foundation geometry on bridge pier scour. Journal of Hydraulic Engineering, ASCE, 122(4): 203-209.

Mercille, B., 2001. La reconstruction de rivière à la suite du déluge de 1996 au Québec: Tenir compte de l'importance économique des resources fauniques: The reconstruction of rivers following the 1996 deluge in Quebec: Taking into account the economic importance of the fauna. Techniques - Sciences - Methodes, 3: 44-50.

Meselhe, E.A. and Sotiropoulos, F., 2000. Three-dimensional numerical model for open-channels with free-surface variations. Journal of Hydraulic Research, 38(2): 115-121.

Mia, M.F. and Nago, H., 2003. Design method of time-dependent local scour at circular bridge pier. Journal of Hydraulic Engineering, ASCE, 129(6): 420-427.

Minns, C.K., 1997. Quantifying 'no net loss' of productivity of fish habitats. Canadian Journal of Fisheries & Aquatic Sciences, 54(10): 2463-2473.

Minns, C.K., Kelso, J.R.M. and Randall, R.G., 1996. Detecting the response of fish to habitat alterations in freshwater ecosystems. Canadian Journal of Fisheries & Aquatic Sciences, 53(Suppl. 1): 403-414.

Molinas, A. and Hafez, Y.I., 2000. Finite element surface model for flow around vertical wall abutments. Journal of Fluids and Structures, 14: 711-733.

Molinas, A., Kheireldin, K. and Wu, B., 1998. Shear stress around vertical wall abutments. Journal of Hydraulic Engineering, ASCE, 124(8): 822-830.

Molls, T. and Chaudhry, M.H., 1995. Depth-averaged open-channel flow model. Journal of Hydraulic Engineering, ASCE, 121(6): 453-465.

Muotka, T., Novikmec, M., Laasonen, P., Paavola, R. and Haapala, A., 2002. Long-term recovery of stream habitat structure and benthic invertebrate communities from in-stream restoration. Biological Conservation, 105(2): 243-253.

Nagata, N., Hosada, T. and Muramoto, Y., 2000. Numerical analysis of river-channel processes with bank erosion. Journal of Hydraulic Engineering, ASCE, 126(4): 243-252.

Newbury, R.W. and Gaboury, M.N., 1993. Stream analysis and fish habitat design: a field manual. Newbury Hydraulics Ltd., British Columbia.

Nicholas, A.P., 2001. Computational fluid dynamics modelling of boundary roughness in gravel-bed rivers: An investigation of the effects of random variability in bed elevation. Earth Surface Processes and Landforms, 26: 345-362.

Nicholas, A.P. and Mitchell, C.A., 2003. Numerical simulation of overbank processes in topographically complex floodplain environments. Hydrological Processes, 17(727-746).

Oliveto, G. and Hager, W.H., 2002. Temporal evolution of clear-water pier and abutment scour. Journal of Hydraulic Engineering, ASCE, 128(9): 811-820.

Olsen, N. R.B. and Stokseth, S. 1995. Three-dimensional numerical modelling of water flow in a river with large bed roughness. Journal of Hydraulic Research, 33(4), 571-581.

Olson, R.M. and Wright, S.J. 1990. Essentials of engineering fluid mechanics. Harper & Row, New York.

Ouillon, S. and Dartus, D., 1997. Three-dimensional computation of flow around groyne. Journal of Hydraulic Engineering, ASCE, 123(11): 962-970.

Paquier, A. and Khodashenas, S.R., 2002. River bed deformation calculated from boundary shear stress. Journal of Hydraulic Research, 40(5): 603-609.

Parrish, D.L., Reeves, G.H., Behnke, R.J., Gephard, S.R. and McCormick, S.D., 1998. Why aren't there more Atlantic salmon (Salmo salar)? Canadian Journal of Fisheries and Aquatic Sciences, 55 (Suppl. 1): 281-287.

Pretty, J.L. et al., 2003. River rehabilitation and fish populations: assessing the benefit of instream structures. Journal of Applied Ecology, 40(2): 251-265.

Rahman, M.M. and Haque, M.A., 2004. Local scour at sloped-wall spur-dike-like structures in alluvial rivers. Journal of Hydraulic Engineering, ASCE, 130(1): 70-74.

Rameshwaran, P. and Naden, P.S., 2003. Three-dimensional numerical simulation of compound channel flows. Journal of Hydraulic Engineering, ASCE, 129(8): 645-652.

Richardson, J.E. and Panchang, V.G., 1998. Three-dimensional simulation of scour-inducing flow at bridge piers. Journal of Hydraulic Engineering, ASCE, 124(5): 530-540.

Robson, C., 2003. Three-dimensional flow dynamics and bed morphology around deflectors in a laboratory flume. MSc Thesis, McGill, Montreal, 140 pp.

Roper, B.B., Dose, J.J. and Williams, J.E., 1997. Stream restoration: Is fisheries biology enough? Watershed Restoration, 22(5): 6-11.

Salaheldin, T.M., Imran, J. and Chaudhry, M.H., 2004. Numerical Modeling of three-dimensional flow field around circular piers. Journal of Hydraulic Engineering, ASCE, 130(2): 91-100.

Scruton, D., 1996. Evaluation of the construction of artificial fluvial salmonid habitat in a habitat compensation project, Newfoundland, Canada. Regulated Rivers: Research and Management, 12(2-3): 171-183.

Seckin, G., Yurtal, R. and Haktanir, T., 1998. Contraction and expansion losses through bridge constrictions. Journal of Hydraulic Engineering, ASCE, 124(5): 546-549.

Shamloo, H., Rajaratnam, N. and Katopodis, C., 2001. Hydraulics of simple habitat structures. Journal of Hydraulic Research, 39(4): 351-366.

Shields-Jr, F.D., Copeland, R.R., Klingeman, P.C., Doyle, M.W. and Simon, A., 2003. Design for stream restoration. Journal of Hydraulic Engineering, ASCE, 129(8): 575-584.

Shields-Jr, F.D., Knight, S.S. and Cooper, C.M., 1995a. Incised stream physical habitat restoration with stone weirs. Regulated Rivers: Research and Management, 10(2-4): 181-198.

Shields-Jr., F.D., Cooper, C.M. and Knight, S.S., 1995b. Experiment in stream restoration. Journal of Hydraulic Engineering, ASCE, 121(6): 494-502.

Shields-Jr., F.D., Knight, S.S. and Cooper, C.M., 1998. Rehabilitation of aquatic habitats in warmwater streams damaged by channel incision in Mississippi. Hydrobiologia, 382: 63-86.

Shields-Jr., F.D., Knight, S.S., Morin, N. and Blank, J., 2003. Response of fishes and aquatic habitats to sand-bed stream restoration using large woody debris. Hydrobiologia, 494: 251-257.

Sinha, S.K. and Marelius, F., 2000. Analysis of flow past submerged vanes. Journal of Hydraulic Research, 38(1): 65-71.

Spalding, D.B., 2002. PHOENICS overview: CHAM technical report TR 001. In: Ludwig (Editor), TR 000 PHONEICS Hard-Copy Documentation (Version 3.5). Concentration, Heat, and Momentum Ltd., London.

Sukhodolov, A., Uijttewaal, W.S.J. and Engelhardt, C., 2002. On the correspondence between morphological and hydrodynamical patterns of groyne fields. Earth Surface Processes and Landforms, 27: 289-305.

Sukhodolov, A., Engelhardy, C., Kruger, A. and Bungartz, H., 2004. Case study: turbulent flow and sedmient distributions in a groyne field. Journal of Hydraulic Engineering, ASCE, 130(1): 1-9.

Thompson, D.M., 2002. Channel-bed scour with high versus low deflectors. Journal of Hydraulic Engineering, ASCE, 128(6): 640-643.

Thompson, D.M. and Stull, G.N. 2002. The development and historical use of habitat structures in channel restoration in the United States: The grand experiment in fisheries management. Geographie Physique et Quaternaire, 56: 45-60.

Thorne, C.R., 1997. Channel types and morphological classification. In: C.R. Thorne, R.D. Hey and M.D. Newson (Editors), Applied fluvial geomorphology for river engineering and management. John Wiley and Sons, New York, pp. 175-222.

Trimble, S.W. and Crosson, P., 2000. Soil erosion rates - myth and reality. Science, 289(5477): 248-250.

Umbrell, E.R., Young, G.K., Stein, S.M. and Jones, J.S., 1998. Clear-water contraction scour under bridges in pressure flow. Journal of Hydraulic Engineering, ASCE, 124(2): 236-240.

VigilarJr., G.G. and Diplas, P., 1998. Stable channels with mobile bed: Model verification and graphical solution. Journal of Hydraulic Engineering, ASCE, 124(11): 1097-1108.

Wallerstein, N.P., 2003. Dynamic model for constriction scour caused by large woody debris. Earth Surface Processes and Landforms, 28: 49-68.

Wesche, T.A., 1985. Stream channel modification and reclamation structures for the improvement of salmonid rearing habitat in a coastal stream in British Columbia. In: C.J. Hassler (Editor), Propogation, enhancement, and rehabilitation of anadromous salmonid populations and habitat symposium. American Fisheries Society, Humboldt State University, Arcata CA, pp. 99-108.

White, R.J., 1996. Growth and development of North American stream habitat management for fish. Canadian Journal of Fisheries & Aquatic Sciences, 53 (Suppl. 1)(342-363).

Whitehouse, R.J.S., 1997. Scour at marine structures: A manual for engineers and scientists. SR417, HR Wallingford Ltd., Wallingford, U.K..

Wilcock, P.W., 1996. Estimating local bed shear stress from velocity observations. Water Resources Research, 32(11): 3361-3366.

Williams, E. and Simpson, J.H., 2004. Uncertainties in estimates of Reynolds stress and TKE production rate using the ADCP variance method. Journal of Atmospheric and Oceanic Technology, 21(2): 347-357.

Wu, S. and Rajaratnam, N., 1996. Submerged flow regimes of rectangular sharp-crested weirs. Journal of Hydraulic Engineering, ASCE, 122(7): 412-414.

Wu, S. and Rajaratnam, N., 2000. A simple method for measuring shear stress on rough boundaries. Journal of Hydraulic Research, 38(5): 399-400.

Yakhot, V. and Orszag, S.A. 1986. Renormalization group analysis of turbulence. Journal of Scientific Computing, 1, 536-551.

Yen, C.-L., Lai, J.-S. and Chang, W.-Y., 2001. Modeling of 3D flow and scouring around circular piers. Proc. Natl. Sci. Counc. ROC(A), 25(1): 17-26.

Zalewski, M. and Welcomme, R., 2002. Restoration of sustainability of physically degraded fish habitats - the model of intermediate restoration. Ecohydrology and Hydrobiology, 1(3): 279-282.

Zheng, Y. and Jin, Y.-C., 1998. Boundary shear in rectangular ducts and channels. Journal of Hydraulic Engineering, ASCE, 124(1): 86-89.

Ziegenhorn, R., 2000. A river full of fish: Industrial catfish production and the decline of commercial fishing on the upper Mississippi River. Human Organization, 59(2): 162-168.